Modeling the Infrared Continuum Emission of a Sample of Hard X-Ray Selected Active Galactic Nuclei

by

Seamus Riley

A dissertation submitted to The Johns Hopkins University in conformity with the requirements for the degree of Doctor of Philosophy.

Baltimore, Maryland

September, 2013

Abstract

We model *Spitzer* Infrared Spectrograph (IRS) data spanning $5-40\mu m$ of 66 hard X-ray selected active galactic nuclei (AGN) in an attempt to isolate and define the individual emission components. Our sample is drawn from the *Swift* Burst Alert Telescope (BAT) AGN survey, a wide-field, uniform, flux limited survey sensitive to all but the most Compton-thick AGN. This work uses a new spectral de-convolution and modeling technique in the IR using XSPEC, a well test X-ray spectral modeling software. Our model has four components: a clumpy torus obscuration region, dusty narrow line region (NLR) clouds, a host galaxy dust model, and blackbody dust. We also incorporate a silicate absorption multiplicative model to account for host galaxy dust absorption. All of our AGN can be modeled with combinations of components yielding a distribution of geometric parameters that describe the AGN models. We derive bolometric luminosities for our AGN using IR and hard X-ray flux that refine our models. We derive torus covering factors, size, thickness, inclination, and opacity from our models and are capable of calculating the likelihood of the directly observing accretion disk emission for every AGN. Our models indicate a significant

ABSTRACT

correlation between the radial extent of the torus and the bolometric luminosity. We can reproduce the observed fraction of optically obscured AGN using our geometric covering factor. Comparisons with hard X-ray flux and variability allow us to predict the impact of changes in bolometric luminosity on the torus shape. Our NLR model demonstrates the isotropic nature of the NLR continuum which correlates strongly with bolometric indicators such as [O IV] 25.89 μm luminosity. We find the average covering factors of the NLR and torus are 54 and 8%. Our sample also exhibits host galaxy absorption that we believe can impact the AGN type observed.

Primary Reader: Kim Weaver

Secondary Reader: Holland Ford

Acknowledgments

This work is based on observations made with the Spitzer Space Telescope, which is operated by the Jet Propulsion Laboratory, California Institute of Technology under a contract with NASA. Support for this work was provided by NASA Goddard Space Flight Center.

Dedication

This thesis is dedicated to my wife, Jessica Brick, who stood with me through it all.

Contents

CONTENTS

List of Tables

List of Figures

Chapter 1

Introduction

1.1 Summary

One of the most fundamental questions of present-day cosmology is the role played by supermassive black holes (SMBHs) in galaxy evolution. Presumed to be residing in the nucleus of most galaxies, these black holes can be on the order of millions of times the mass of the sun. Yet because of their relatively small spatial scale and their location in the often opaque galactic nucleus it is frequently difficult to directly quantify black hole properties. We know that a clear relationship exists between SMBHs and host galaxies despite the limited sphere of gravitational influence of the SMBH. Called the M-σ relation (or MBH-σ), Ferrarese & Merritt (2000) and Gebhardt et al. (2000) independently observed that the stellar velocity dispersion (σ) of the host galaxy bulge correlates with the mass of the central black hole. The tightness

of the relation implies that there is feedback between the processes of supermassive black hole evolution and galaxy bulge growth. This feedback is likely both radiative (Sazonov et al., 2004, 2005, e.g) and mechanical (Begelman & Nath, 2005; Di Matteo et al., 2005, e.g) in nature and originates during periods of active black hole accretion.

Detailed knowledge of SMBHs has historically come from observations of active galactic nuclei (AGN) at discrete wavelengths such as the optical, soft X-ray, and radio (see Sections 2.1.2, 2.1.5, and 2.1.1). But because of the variety of spectral features and degrees of obscuration present in AGN (Section 1.2.2), is it difficult to construct scientifically unbiased samples from which to base concrete statistical tests of observational properties. Depending on the wavelengths at which data are gathered, it can be hard to untangle the spectral signatures associated with the SMBH from those of stellar processes. It is particularly troublesome that the spectral signatures from the accretion disk happen to fall within regions of the spectrum where there can be significant stellar contamination (IR, optical, and UV) and/or significant obscuration (optical, UV, and X-ray).

This work uses a new spectral de-convolution and modeling technique in the IR to examine a well-defined sample of X-ray selected AGN. Questions of dust properties, photoionization, obscuration, variability, stellar contributions, and geometry are addressed. The analysis presented allows us to improve our understanding of AGN characteristics in a statistically meaningful way along with analysis of the galaxies which host them.

The current knowledge of AGN is replete with questions yet to be answered. These questions can be divided into several categories: accretion processes, galaxy-AGN interactions/feedback, modifications to unification theory, and assessing the geometry of the obscuration region. Although not exhaustive, this thesis will work to contribute answers to these areas of AGN study. Questions to be specifically examined in this work are listed in Section 1.2.3.

1.2 AGN

1.2.1 What are Active Galactic Nuclei?

Active galactic nuclei (AGN) are enormously luminous objects located at the centers of many galaxies, and they consist of material falling into supermassive black holes. Universal to AGN is a prodigious luminosity assigned to an unusually small volume. The efficiency for such intense energy production on a small scale requires the most efficient known radiation mechanism ($\epsilon = 0.1$), accretion into a relativistically deep gravitational potential. The falling matter collapses into a rotationally supported disk and spirals into the potential well. The observational constraints that one can place on the emissive volume allow us to infer that the gravitational well must be a supermassive black hole (Krolik, 1999). The most compelling example of this is the Keplerian rotation seen via water masers in the accretion disks (e.g., Claussen & Lo, 1986). The masers of NGC 4258, offset $0.13 - 0.29\,\mathrm{pc}$ from the center, trace line

of sight velocities of $\pm 1000\,\mathrm{km\,s^{-1}}$ from the galaxy systemic velocity revealing a mass of $3.6 \times 10^7\,\mathrm{M_\odot}$ concentrated within 0.13 pc (Miyoshi et al., 1995). Furthermore, the adherence of the masers to Keplerian motion implies a mass distribution with radius $\leq 0.012\,\mathrm{pc}$, implying $\rho > 5 \times 10^{12}\,\mathrm{M_\odot\,pc^{-3}}$. This density, if not initially a SMBH, would quickly collapse into one.

Despite the simple premise of infalling matter, AGN emit across an incredibly broad range of energies. Although not universal, some AGN have been observed with comparable luminosity per logarithmic energy interval across thirteen decades of energy (Krolik, 1999). Determining the mechanisms for this broad radiation requires understanding of the morphology of AGN across a huge variety of physical scales.

1.2.2 AGN Morphology and Observation

The compact nature of AGN has made them nearly impossible to image in any electromagnetic frequency but radio. Radio observations show that the supermassive black hole at the center of some galaxies is surround by an accretion disk. That this disk is occasionally warped remains unexplained (Miyoshi et al., 1995; Herrnstein et al., 2005). Orbiting material must transfer angular momentum outwards in order to move inwards along the disk. Theoretical mechanisms for this transfer have been suggested but none are totally understood. The most common proposed mechanisims include turbulence driven viscosity (Shakura & Sunyaev, 1973), turbulent Maxwell stresses (Balbus & Hawley, 1991), and magnetically bound outflows (Begelman et al.,

1983). The latter is particularly interesting because material ejection could be used to explain the presence of dust responsible for disk anisotropy.

The most commonly known kind of AGN is classified as a Seyfert galaxy (Seyfert, 1943) and is defined as a galaxy with an incredibly bright point-like nucleus. Seyferts are less luminous than quasars, their more distant and unresolved counterparts. There are two types of Seyfert galaxies, Type 1 exhibit both broad (FWHM $\sim 10^3$ to 10^4 km s^{-1}) and narrow (FWHM $\sim$ 250 to 900 km s^{-1}) optical emission lines, Type 2 show only narrow lines. The emission of these lines is thought to originate in two distinct regions, the broad line region (BLR) and narrow line region (NLR). The bifurcation of AGN type is explained by the commonly named "unification theory" which asserts that both classes are drawn from the same parent sample but observed by us at different inclination angles (Antonucci, 1993). An equatorial obscuration region of dust is proposed to surround the central accretion disk and thus blocks both the velocity-broadened emission lines from the BLR and any relativistically-broadened emission lines from the accretion disk. For simplicity of this straw man model, the obscuring region was initially assumed to be toroidal in shape. The Type 1 and Type 2 nomenclature (unobscured and obscured respectively) is used for both Seyferts and quasars. AGN are sometimes assigned a fractional numerical classification depending on the relative narrow and broad line strengths (i.e. 1.2, 1.5, 1.8, and 1.9). Unification theory explains many other observational characteristics across many wavelength regimes. The ramifications of these characteristics will be discussed later in Section

2.1.

The accretion disk emits most strongly in the UV (Elvis et al., 1994). Dissipative momentum transferring processes heat the disk (Shakura & Sunyaev, 1973) so that the primary emission is blackbody in nature (Malkan, 1983). Above and below the plane of the disk, a corona of relativistic electrons inverse Compton scatters much of this radiation yielding a power-law component in the X-ray band. The exact shape of the spectral continuum between the optical and soft X-ray energy bands is unclear even for Type 1 AGN, as it is often obscured by intervening gas either in the host galaxy, intergalactic medium (IGM), or the interstellar medium (ISM). When unobscured, the BLR emits emission lines which are broadened to Doppler widths in the range $\sim 1,000$ to $25,000$ km s^{-1}. The origin and shape of this high-density, high-velocity gas is uncertain, but it is believed that the BLR clouds may exist in either a disk wind or in extended sections of the disk itself (e.g., Elvis, 2000). The time delay between disk continuum emission fluctuations and BLR emission line variability can be measured in a process called reverberation mapping to determine the BLR radius (e.g., Peterson et al., 2005). When combined with line-of-sight velocities from BLR widths, the virial theorem can be invoked to estimate black hole masses. This method provides the most robust AGN black hole mass estimator but requires extensive spectroscopic variability measurements. Work by Kaspi et al. (2005) has demonstrated a luminosity-BLR radius scaling relation, yet this has resulted in many less robust mass estimates being based on only luminosity and BLR line width.

The theoretical underpinnings of disk accretion are understood, but the specific mechanisms remain speculative. The exact method for angular momentum transport is uncertain and details regarding disk winds, magnetic confinement of ejecta, and energy transfer to the hot plasma of the corona remain tentative. A new category of thick, radiatively inefficient, accretion disks has been proposed as more low luminosity AGN are discovered (Abramowicz et al., 1995). These new disks are likely advection dominated and have entirely unique emission properties (Narayan et al., 1995). Our level of understanding of the theoretical physics of these objects is shown when one considers that the presence of an equatorial obscuration region in these objects is unclear (Elitzur & Ho, 2009). This means we are capable of producing accretion models that reproduce some AGN SEDs (e.g., Nenkova et al., 2008b; Hubeny et al., 2000), but none are free of assumptions.

The coronal X-ray emission remains unobscured at the highest energies (at least for typical Compton-thin AGN), but soft X-rays can be depleted or entirely obscured from our view by intervening dust (e.g., LaMassa et al., 2011). Narrow emission lines are visible originating from clouds of dust and gas both above and below the accretion disk. The clouds that make up these narrow line regions (NLR) are far enough from the disk and obscuring equatorial region that they are expected to emit isotropically. Isotropic emission is confirmed by the strength of the most common narrow lines such as [O IV] 25.89 μm, [Ne II] 12.81 μm, [Ne III] 15.56 μm, and [Ne V] 14.32/24.32 μm (e.g., Meléndez et al., 2008; Diamond-Stanic et al., 2009; Rigby

et al., 2009). No line strength disparities in the IR for a hard X-ray selected sample of nearby AGN are observed between Seyfert 1 and 2 populations (Weaver et al., 2010).

Even farther out from the NLR, narrow collimated jets are often seen in the radio band on both sides of the host galaxy. Their morphology is varied and their size ranges from barely resolvable to hundreds of kiloparcecs in length. Radio lobe jet galaxies are subdivided into those with core-dominated emission, and those with an immensely bright leading edge; known as Fanaroff-Riley 1 and 2 radio galaxies respectively (Fanaroff & Riley, 1974). Curiously, the core dominated emission lobes (FR1s) often feature bending down the length of the lobe (e.g., 3C 31) indicative of either a host galaxy interaction or a variable jet orientation (Kembhavi & Narlikar, 1999). These objects, while easily resolved and often times very radio bright, give only a small fraction of the total luminosity at radio wavelengths. A frequently used cutoff to distinguish between radio loud and radio quiet AGN is $L_{radio}/L_{optical} \sim 2 \times 10^{-4}$ (Krolik, 1999) highlighting the weakness of the radio emission. Although the exact mechanism for launching these often enormous jets is unknown, symmetry dictates the jets are normal to the accretion disk. Interestingly, there has been no detected correlation between the jet position angle and the galaxy disk axis in Seyfert galaxies (e.g., Schmitt et al., 1997; Clarke et al., 1998; Nagar & Wilson, 1999). There is also a unique phenomenon of incredibly bright non-thermal emission seen from radio to hard X-ray when the jet is oriented in the line of sight of the observer. These objects, termed blazars, demonstrate incredibly anisotropic synchrotron and inverse Compton

emission that is relativistically beamed toward the observer. This results in highly variable and luminous objects.

1.2.3 Open Questions

1. **Obscuration related angle dependence is not completely understood.** Because most of the obscuration is due to dust, which has a sublimation temperature $\sim$ 1500K, most re-radiation in the infrared is expected. The heated dust should act as a blackbody with a sharp edge where the dust is being destroyed by ionizing radiation. The simple solid torus shaped cloud model has been replaced in practice with an ensemble of dusty clumps (Nenkova et al., 2002). The variety of infrared spectral shapes observed is better fit with a group of clumps with a multitude of ionization parameters depending on cloud location instead of a large smooth torus (Krolik & Begelman, 1988).

The size of the putative toroidal region has been roughly estimated to have a radius comparable to the height ($R/H \sim 1$) based on analysis of the observed type 1 and 2 objects (Antonucci, 1993); but accurately quantifying this requires an unbiased AGN catalog as well as an accurate understanding of the toroidal shape and features. Most AGN continuum studies focus on unobscured AGN (Section 3.4) so little work has gone into reproducing the entire distribution of AGN types with toroidal models. Given the limited testing of advanced torus models on multiple AGN types, little is known about model applicability and ability to predict the degree of obscuration.

2. **The origin of the dusty torus as well as the impact of AGN variability on the torus are unknown.** The torus clouds are generally treated as static objects in AGN continuum modeling. Some speculate that magnetically confined, radiation pressure driven outflows might be responsible for clumpy torus clouds (e.g, Krolik, 1999; Elvis, 2000). If this is the case, it has been noted that incredibly low luminosity AGN may lack the radiation pressure to sustain winds of this nature eliminating the possibility of true type 2 low-luminosity AGN (Elitzur & Ho, 2009). IR variation in AGN is well studied (e.g., Ulrich et al., 1997; Minezaki et al., 2006; Landt et al., 2011) but has never been linked directly to specific torus continuum simulations.

3. **Isotropic nature of the NLR region remains unknown.** The NLR regions of many nearby AGN have been directly observed (e.g., NGC 1068, Evans et al., 1991). The [OIV] 25.89 μm line has been claimed to be a good tracer of bolometric luminosity with identical distributions between type 1 and 2 AGN (Diamond-Stanic et al., 2009). But at the same time, the BAT AGN sample contains 6 previously undiscovered AGN that are under-luminous in [O IV] (Weaver et al., 2010). The [O III] line has also long been used as an isotropic indicator, but for a reddening corrected sample, Weaver et al. (2010) confirm that it does not reliably gauge AGN activity. This discrepancy demonstrates that even seemingly ideal isotropic features can be obscured by host galaxy dust.

4. **What is the nature of AGN feedback?** A mechanism for SMBH-galaxy feedback was suggested by Rees (1998). He modeled supermassive black holes formed

before the majority of the galaxy bulge became stars that regulate star formation with ionizing radiation and AGN outflows. The exact details of this regulation are speculative. Furthermore, we know that jets visibly impact the interstellar medium (ISM), and AGN are often observed with high levels of host galaxy nuclear star formation. Many studies have compared AGN frequency and galaxy morphology. Adams (1977) noted the tendency of radio quiet AGN to be in disk galaxies whereas radio loud objects were primarily in elliptical galaxies. Despite significant complications due to likelihood of radio loud galaxies to be significantly brighter then the morphologically observable radio quiet counterparts, this trends seems to stand (Krolik, 1999). An additional unknown is the correlation or lack thereof between galaxy and AGN orientations. As previously mentioned this is uncorrelated in the case of jets, but perhaps a sample not relying on radio emission might have a different outcome. Only a completely unbiased and resolved set of AGN is capable of definitively revealing whether or not a correlation exists

1.3 The Scope of this Thesis

This thesis examines the geometry of the obscuration regions in nearby AGN using infrared spectroscopic observations. We remain open to questions regarding accretion physics, host galaxy properties, and AGN evolution; however we will focus our efforts using these fields as tools to isolate the geometric properties of a sample of AGN.

Our goal is based on the applicability of our data to the problems of the field as well as on the strengths of our unique technique and approach to model fitting. Previous work in this subfield lacks a comprehensive and unbiased sample and methodology such as ours.

Observations in the IR were substantially limited before the launch of the *Spitzer Space Telescope*. Limited by atmospheric molecules, atmospheric windows in the IR have made ground-based, complete spectroscopic continuum observations of AGN impossible. The advent of space based IR telescopes has steadily and incrementally increased capabilities from the *Infrared Astronomical Satellite* to *Spitzer*. The use of IR indicators to search for AGN will be discussed in the Chapter 2; here we will focus on how IR data has impacted our knowledge of AGN.

1.3.1 Current Literature

Infrared AGN observations are inherently geared towards the study of two emission mechanisms: thermal torus warm dust and gas, and narrow emission line region clouds. The former is difficult to resolve and easily confused with galaxy dust so has been limited in its study. It is most easily studied using photometric continuum measurements (e.g., Stern et al., 2005; Alonso-Herrero et al., 2006; Ward et al., 1987). The latter of these are easily visible with ground and space based observations so has a wealth of prior observations and resulting literature.

NGC 1068 exemplifies the attempts that have been made to observe both torus

and NLR clouds photometrically for a very near (14.4 Mpc) and bright Type 2 Seyfert galaxy. High-resolution IR photometric observations reveal both an ionization cone with a similar orientation to radio jet observations (Rouan et al., 1998; Alloin et al., 2000; Bock et al., 2000) as well as a perpendicular structure 80 pc in width purported to be a torus by Marco & Alloin (2000). Jaffe et al. (2004) use interferometric mid-IR observations to resolve a structure 2.1 pc thick and 3.4 pc wide that they claim to be the first resolved AGN torus. Galliano et al. (2003) use high-resolution photometric data to create a nuclear SED in order to test torus geometries but find that with 12 photometric data points, they are incapable of assigning strong constraints on geometric parameters. Furthermore, their fluxes are derived from observations with varying apertures and stellar subtraction methods. Although a great deal can be learned about a single AGN with comprehensive photometric analysis, the majority of modern AGN IR research has focused on IR spectra of AGN.

IR emission lines can be used as a probe of NLR activity and can reveal information regarding cloud velocities (Crenshaw & Kraemer, 2000), metalicity (Groves et al., 2006b), shape (Kaiser et al., 2000), densities (Meléndez et al., 2008), and ionizing radiation (Meléndez et al., 2011) of the NLR. Although these lines exist in the UV, optical, and IR and all of these can be used to probe NLR conditions; the only emission lines capable of penetrating dusty obscuration are those in the IR. The use of these IR emission lines and ratios to detect AGN will be discussed in Chapter 2.

1.3.2 The State of Theoretical Models in the IR

The next step in AGN spectroscopy is the modeling of continuum emission with comprehensive models that include torus, NLR, and host galaxy dust. The wide variety of spectral shapes possible is demonstrated by Weedman et al. (2005) and is indicative of the flexibility in modeling required when modeling AGN continua. Whereas photometrical SED have been enlightening regarding basic torus properties (e. g., Pier & Krolik, 1993; Granato & Danese, 1994), modern space-based spectroscopy has dramatically increased the ability to constrain models. Torus models have relied on two independent geometries to account for the variety of SEDs observed, that of a smooth flared disk (e.g., Efstathiou & Rowan-Robinson, 1995; Manske et al., 1998; van Bemmel & Dullemond, 2003), and that of a clumpy disk (e.g., Nenkova et al., 2008a,b, hereafter N08). Whereas both sets of models have been applied successfully to data (e.g., Fritz et al., 2006; Mor et al., 2009, respectively), the clumpy medium models have a few advantages. The torus was initially thought to be clumpy (Krolik & Begelman, 1988) to protect the grains from photodissociation, but smooth models were an easier modeling starting point (Pier & Krolik, 1992, 1993). Smooth distributions however lack the ability to match the range of far-IR emission observed as well as require a finely tuned set of parameters to account for face-on silicate emission feature suppression (Nenkova et al., 2002). These problems can be solved with the use of clumpy media (Rowan-Robinson, 1995). N08 created a comprehensive set of clumpy models that will be explained in Section 3.3.3.

As seen from the photometric data, the NLR can also be responsible for substantial IR emission. These regions have been modeled by Groves et al. (2006a, hereafter G06) with consideration given to both the emission line and continuum emission. Details of the model will be given in Section 3.3.4. Schweitzer et al. (2008, hereafter S08) used their model with a combination of blackbodies representing torus emission to fit a sample of Palomar Green QSOs. They found observed silicate emission can be reproduced by their NLRs and also fit several geometric NLR parameters such distance and covering factor for their sample. Mor et al. (2009) and Mor & Netzer (2012) (hereafter M09 and M12) also fit a sample of AGN with both N08 and G06 models. Their work exemplifies both the efficacy of these two models as well as the geometric characteristics of a sample of Type 1 Seyferts. Our analysis will include an evaluation of the fitting technique, models, and parameter distributions of these previously studied samples (Section 3.4).

Chapter 2

Identifying a Less Biased Sample

2.1 Previous Samples

The creation of a standardized, unbiased, and complete sample of AGN is a difficult task for several reasons. AGN can appear different to an observer depending on the wavelength in which they are seen. Elements of the broad AGN spectrum can be absent or faint because of intrinsic differences in the AGN geometry (e.g., radio jets) or obscured by orientation dependent AGN dust or other intervening material. The varied nomenclature of AGN is a result of the fact that depending of the wavelength of observations, AGN can look like fundamentally different phenomena. Samples derived solely from observations within a single electromagnetic bandpass can select very different objects.

We will make a quick overview of historic surveys in an effort to justify the ro-

bustness of our hard X-ray selected sample of AGN. We will begin with observations in the radio band and work our way toward X-ray energies.

2.1.1 Radio Surveys

Radio searches are biased toward radio-loud AGN and suffer contamination issues at low luminosities. Radio emission is usually associated with AGN jets, and thus is emitted anisotropically. The unique geometry and brightness of radio jet emission makes radio observations extremely effective at finding AGN, yet less than 10% of AGN have luminous radio emission (White et al., 2000). At lower radio luminosities, the AGN radio emission generally lacks a clear morphology, and is difficult to discern from the radio emission associated with star formation (Barger, 2004). Rapid-evolving star formation is often present in both active and inactive galaxies, meaning that follow up observations in wavebands other than the radio are necessary to detect AGN without resolvable jets in low luminosity radio surveys of AGN.

2.1.2 Optical Surveys

Samples of AGN constructed in the optical regime are highly biased in their selection. The most notable optical survey bias is intrinsic to the AGN itself; optical emission is obscured by the presence of AGN dust in Type 2 AGN. No photometric optical selection technique can overcome this bias. Independent of this caveat,

photometric colors can be used to determine which galaxies contain optically luminous AGN. Selection criteria can be made to separate the broad and smooth AGN optical continua from the thermal, strongly curved galactic spectra (Sandage, 1971). However, completion of such a sample is difficult because robust elimination criteria are required to isolate the small fraction of AGN compared to inactive galaxies (Hartwick & Schade, 1990). This optical selection technique is clearly biased against finding faint AGN in relatively bright host galaxies. One complication is that optical galactic continuum emission can appear flattened and therefore less thermal, due to redshifted Lyα emission (Krolik, 1999). For larger redshifts, the AGN SED can appear less flattened (and more thermal) in the optical due to Lyman continuum absorption (Krolik, 1999). An additional complication arises in surveys of nearby AGN where objects without resolved host galaxies are cut to eliminate stars (Barger, 2004). This can bias against extremely AGN dominated galaxies that appear point-like.

Even after the application of stringent color criteria, objects classified by color often require optical spectroscopic follow up observations to eliminate contamination of a sample by galaxies that do not contain AGN. AGN systems provide discrete signatures of kinematically broadened emission lines, but these broad lines are only observable when unobscured by the putative torus. The broad lines serve as a definitive but heavily biased method of discovering AGN. Narrow emission lines can also indicate activity especially with the use of specific diagnostic line ratios (e.g., Kewley et al., 2006). Because spectroscopic classifications are more robust than photometric

ones, an ideal survey would simply take spectroscopic measurements of every galaxy.

The Sloan Digital Sky Survey (SDSS) has become a valuable optical data set. Through mapping the entire sky, the SDSS delivers a flux limited galaxy survey with spectroscopic follow-up of many kinds of objects. Most notable is the color selection (based on the *ugriz* colors) of probable AGN. Outliers of a stellar locus in four dimensional color space are targeted for spectroscopic observations (Richards et al., 2002). Derived from these spectroscopically observed objects, and another $\sim 100,000$ galaxy spectra, Hao et al. (2005) find 6,391 confirmed nearby AGN fainter than the magnitude cut off $r = 17.77$. These local AGN are supplemented by 105,783 spectroscopically confirmed quasars (Schneider et al., 2010).

2.1.3 Ultra-Violet Surveys

The AGN SED shows a strong intrinsic peak in the UV because of hot gas associated with the accretion disk (Shields, 1978). UV light plays an important role in AGN mechanics, photoionizing the leading edge of the obscuration region (e.g., Barvainis, 1987), possibly aiding in ejection of magnetically bound regions from the disk (e.g., Pelletier & Pudritz, 1992), and serving as a source of photons to be inverse Compton scattered into the X-ray (e.g., Bregman, 1990). Yet for edge-on AGN this UV emission is almost completely obscured creating a paucity of type 2 AGN that are observable in the UV. Furthermore, star forming regions excel at the production of UV light (Kennicutt, 1998), often near the nucleus of other galaxies, and the stel-

lar contribution to the integrated spectrum can be significant. Observations are also inhibited by UV attenuation from our atmosphere, the Milky Way, the intergalactic medium, and the AGN host galaxy.

Despite the difficulties with observing in the UV, galaxies with UV excesses between $3400 - 6900\,\text{Å}$ noted by Markarian et al. (1989) led to the ground based First Byurakan Survey yielding 1515 UV objects. These objects were later named Markarian galaxies. From this sample, there are roughly 200 Seyferts, several dozen quasars, and hundreds of starburst galaxies. Although a vital contribution in its time, the output of this survey remains incredibly small compared to other survey techniques.

2.1.4 Infrared Surveys

The second largest peak in AGN SED occurs in the infrared (Elvis et al., 1994). This primarily thermal emission is inherent to the warm dusty, molecular obscuration screen surrounding AGN. It is supplemented with narrow forbidden emission lines originating several parsecs away from the AGN core. Both regions likely emit isotropically and are ubiquitous amongst AGN. The shape of the AGN IR continuum spectrum has not been well enough established to find AGN exclusively with photometric color criteria and requires spectroscopic confirmation (e.g., Weedman et al., 2005). Spectral line-ratio diagnostics based on narrow emission lines fluxes are used to detect AGN activity, yet a perfect selection criterion has not been established. One example of this is the use of the [O IV] 25.89μm/[Ne III] 15.56μm and [Ne III] 15.56

μm/[Ne II] 12.81μm line ratios to isolate AGN activity (Weaver et al., 2010). The [O IV] line correlates with hard X-ray flux – an indicator of AGN bolometric luminosity – to a strong degree (Weaver et al., 2010; Rigby et al., 2009). Similarly, [Ne V] is found to be a strong indicator of AGN bolometric luminosity (e.g., Abel & Satyapal, 2008). Despite the IR band having several indicators of AGN activity, assembling an unbiased IR spectral catalog requires a more effective searching methodology then is currently available. The observations require exposures of significant length and can be difficult to justify for faint targets. The *James Webb Space Telescope* will significantly enhance the ability to find AGN using IR spectra (Gardner et al., 2006).

Many attempts have been made to create an unbiased flux-limited IR catalog. An early attempt by the *Infrared Astronomical Satellite* (IRAS), used photometric color criteria to establish an AGN candidate pool based on warm IR colors (de Grijp et al., 1987). This yielded 1071 candidates with an 18% contamination rate and excluded ∼30% of optically and UV identified AGN (de Grijp et al., 1992). This early photometric data could not provide statistically complete samples. One thing that was discovered is that at low redshifts ($z < 0.2$), Type 2 AGN outnumber Type 1 (Padovani, 1998), a notable finding given the inherent bias for Type 1 AGN of most previous surveys. Subsequent catalogs were built around the Two Micron All-Sky Survey (2MASS), a ground based photometric survey with a limiting magnitude of $K \leq 14$. The Red AGN survey (Cutri et al., 2002) used color based selection on this data set and follow up spectroscopy to discover 485 new AGN. The ratio of Type 1

to Type 2 is nearly four to one (Cutri et al., 2002), implying that a photometric color based survey limited to this atmospheric window does not find most obscured AGN. Photometric IR AGN searches have yet to overcome completeness problems given the robust cuts needed to eliminate the huge number of inactive galaxies.

2.1.5 X-ray Surveys at Soft and Medium X-ray Energies

AGN often display a significant amount of X-ray emission from the accretion disk and the disk corona. The intrinsic X-ray SED is generally described as a cut-off power-law that can be easily modeled as thermal Comptonization (Haardt & Maraschi, 1991). Additionally, a bump component ($\sim$40 keV), a soft excess ($\sim$2 keV), and Fe Kα emission lines with large equivalent widths (a few hundred keV) are often observed (Gandhi, 2005). The bump is attributed to Compton reflection from the disk (Matt et al., 1991). The soft excess could represent the process of Comptonization of photons through a warm coronal layer, a merging of a large number of relativistically blurred soft X-ray lines, or an as of yet unidentified model (Krolik, 1999). The Fe Kα lines are thought to have a number of origins including those that are broadened ($> 10,000\,\mathrm{km\,s^{-1}}$) and redshifted by orbital motions deep within a potential field near the black hole (e.g., Mushotzky et al., 1995) and those far from the central black hole (Weaver et al., 1996).

Observations within the X-ray regime provide an efficient method of finding AGN; any compact source with a luminosity $> 10^{42}\,\mathrm{erg\,s^{-1}}$ (2-10 keV) is considered to be an AGN. This soft-to-medium X-ray emission can be blocked by Compton thick obscuration making it difficult to create an unbiased sample of AGN. Furthermore, observations made in this regime frequently rely on grazing incidence telescopes in order to isolate and image the AGN, but such telescopes are ill suited for large sky surveys (i.e. they require trading resolution for large fields of view). Soft X-ray surveys have been especially effective for tracking type 1 AGN evolution (e.g., Hasinger et al., 2005) and so once absorption effects have been eliminated, X-ray surveys can excel at tracing activity over a large redshift range.

2.1.6 Hard X-ray Surveys

I have explained how the orientation and obscuration effects can strongly bias AGN surveys in radio, UV, optical, and soft X-ray regimes. The two wavelength categories left in which bias is less of a problem are the IR and hard X-ray band. The latter of these two fields represents the newest and most discriminating AGN survey tool. Newest in the sense that the technology has only recently reached needed levels of efficiency. Most discriminating in that, despite the potential for source confusion from poor imaging resolution, there are relatively few non-galactic hard X-ray sources in the sky that are *not* AGN. Furthermore, the increased sensitivity of X-ray detectors allows for the detection of all but the most Compton thick AGN.

Two hard X-ray surveys have been carried out in the last decade. The *International Gamma-Ray Laboratory* (INTEGRAL) is an ESA launched satellite sensitive from 15 keV to 10 MeV with a 0.24 steradian partially coded aperture. It is particularly adept for detecting faint sources with directed pointings. Although this satellite is capable of creating a substantial minimally biased AGN catalog, we choose to utilize the data from the *Swift* observatory.

2.2 Our Sample: *Swift* BAT AGN

The *Swift* Burst Alert Telescope (BAT, Barthelmy et al., 2005) was designed to hunt for gamma ray bursts (GRBs) and follow up with observations of GRB afterglows. Optimized for searching the entire night sky, the *Swift* BAT instrument uses a coded aperture mask to observe 2 steradians of sky at a time. The mask is D-shaped with a 50% of its area blocked by ∼54,000 randomly positioned lead tiles ($5 \times 5 \times 1$ mm) one meter from the detection plane. The 1.2 by 0.6 m CdZnTe detector is sensitive from $15 - 150$ keV with a coded response, and up to 500 keV uncoded. The coded aperture typically yields 4 arcmin position information. While not observing in burst mode to detect and locate GRBs, the telescope is creating the most thorough hard X-ray survey to date. Despite markedly reduced sensitivity compared to other satellites such as INTEGRAL, the wide field of view and extended observation time make it uniquely capable of detecting a large sample of AGN candidates.

Given the relatively poor astrometric accuracy inherent with non-imaging hard X-ray astronomy missions, follow up observations are necessary to verify newly-found objects. Observations with other onboard instruments such as the *Swift* X-Ray Telescope (XRT) allow for AGN verification where archival soft X-ray data do not exist. Because the survey is ongoing, several iterations of BAT results have been published (Tueller et al., 2008, 2010; Baumgartner et al., 2012).

Our targeted objects are derived from both the nine- and 22-month iterations of the *Swift* BAT AGN catalog (Tueller et al., 2008, 2010). Object identification is hindered along the galactic plane ($|b| < 15$) as a result of source confusion, so the *Swift* BAT sample avoids this region. Every object is selected with 4.8σ detection. Of these objects, 266 are identified using follow up XRT or archival observations to be AGN (Tueller et al., 2010). Those that are determined through archival photometric IR observations to be bright enough are selected for *Spitzer* IRS observation. The objects can be split into those bright enough for both high and low-resolution data, and those fainter objects with just low-resolution data. Differences between these data sets and capabilities will be described in the next chapter.

Chapter 3

Observations and Data Reduction

3.1 *Spitzer* Infrared Spectrometer

The *Spitzer Space Telescope* was launched in August 2003 as the last of NASA's four great observatories. The mission was meant to last a minimum of 2.5 years, limited by the 260 liters of onboard liquid helium required to maintain cryogenic conditions for the instruments. The cryogen actually lasted just under 6 years, and now the satellite operates with only the shortest wavelength observations in what is called the *Spitzer* "warm" mission. The satellite contains two photometric imaging instruments and one spectroscopic instrument. The former are called the Multiband Imaging Photometer for *Spitzer* (MIPS) and the Infrared Array Camera (IRAC). MIPS collected data in three energy bands at 24, 70, and 160 μm. IRAC made simultaneous four-band observations at 3.6, 4.5, 5.8, and 8 μm. The warm mission

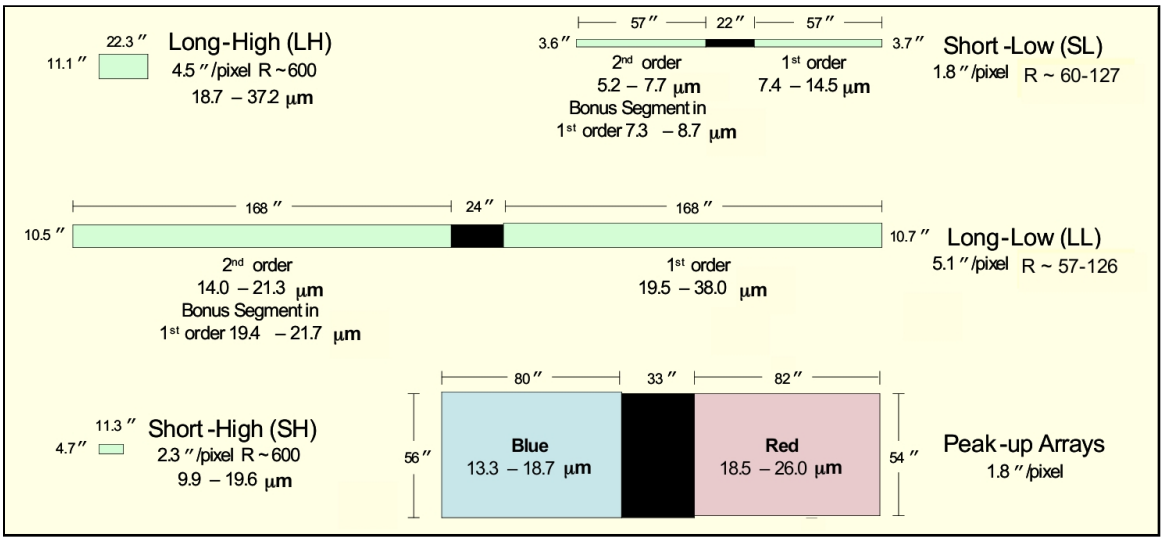

Figure 3.1: From *Spitzer* IRS manual, summary of IRS module properties. Actual slit positions are not parallel as depicted. Actual position angles relative to *Spitzer* roll angle of 0° are SL = +84.7°, LL = +181.2°, SH = +221.5°, LH = +136.7°, and Peak-up = +181.2°.

continues to observe celestial objects with the 3.6 and 4.5 μm filters where the current 30 K instrument temperature still produces useful data. Although data from these instruments have not been taken specifically for this project, a great deal of archival observations exists which aids our research.

Our work focuses on the use of spectroscopic data taken from the *Spitzer* Infrared Spectrometer (IRS, Houck et al., 2004). This instrument consists of four modules divided between high and low resolution as well as long and short wavelengths (Figure 3.1 shows the spectral coverage and resolution by module). The module aperture is slit shaped so that one dimensional spatial information can be collected after the light is diffracted by the the grating. The high-resolution modules pass the filtered light through two gratings which disperse the light in perpendicular directions. This results

in an echelle (ladder-shaped) 2d pattern on the detector (each rung is a different order) maximizing resolution and spectral coverage on a square detector. Each high-resolution module has a different slit size and the SH slit is placed nearly perpendicular to the LH slit on the *Spitzer* focal plane. Observers cannot request specific slit orientations except in extreme cases. The low-resolution modules (Short Low [SL], Long Low [LL]) are only diffracted once but are further divided into two slits each (representing two orders, i.e., SL1 and SL2) requiring twice the exposures for each module. This provides the added benefit of simultaneous background observations wherever both slits are observed; the SL1 slit image can be subtracted from SL2.

The data for this project were mostly obtained by us in two observing runs with *Spitzer* (PI: K. Weaver). The goal of our program was to obtain the first high quality IR spectral survey of an unbiased local AGN sample. These targets provide a means for insight into the true distribution of IR properties of AGN. It is only by having an independent measure of AGN strength and from a well-observed hard X-ray sample that one can untangle the complexity of the IR data. A hard x-ray survey will find all Compton thin AGN in a uniform fashion and determine their intrinsic luminosity. With these data we search for the thermal AGN continuum in the IR, constrain star formation in the galaxies, and construct non ad-hoc continuum models based on hard X-ray fluxes.

Each of our IRS observations is grouped by astronomical observation request (AOR) and follows a generalized observing strategy. This is initialized with slew-

ing the telescope so that either the target or a known offset object is visible to the peak-up detector. This peak-up observation uses either red (13-18.5 μm) or blue (18.5-26 μm) fields of view and the SL detector array to make a photometric image. A centroid position is determined automatically in order to refine the pointing and to insure proper astrometry (a required step given the narrow slit size and 1" inherent astrometry errors). Subsequently, the shift to and between modules contributes negligible pointing error. The target is acquired with a small slew of the telescope with whatever combination of modules is requested. The IRS can be used in either a staring mode centered on a single point, or in a spectral mapping mode that scans over extended objects. All of our observations occur using the former. To create subtraction regions, we supplement our high-resolution observations with off-target observations using an identical observation strategy. For science exposures, a sample up the ramp (SUR) scheme is used to read pixels. This scheme identifies and mitigates cosmic ray data loss by sampling each pixel multiple times between resetting the pixels for each exposure. Every IRS observation is duplicated after "nodding" down the length of the slit so that the object is positioned at 1/3 and 2/3 the length of the slit, ameliorating errors caused by bad pixels. The SUR readings and nodding are repeated for a user-defined number of cycles for each observation (e.g., a 6 second ramp duration for 2 cycles would result in 4 spectra with an on-source integration time of 24 seconds).

Two proposals to study BAT AGN with *Spitzer* IRS were approved (PI: K.

Weaver). The first randomly selected 20 previously unobserved BAT AGN determined to be bright enough for observations with archival IRAS observations. The second proposal sought to supplement the pilot survey with 49 additional IRS spectra capable of detection prominent emission lines, host galaxy PAH features, and the AGN IR continuum. In total, high-resolution data were collected for the 34 brightest local AGN. Low-resolution data were taken for the remaining fainter and more distant objects.

Table 3.1 describes which objects are observed, the net on-target observing time for each object, whether or not the observing strategy included high- or low-resolution modules, host galaxy classifications, and AGN activity classifications. A description of the classification of sources is given in Section 6.1.

Table 3.1: BAT AGN selected for IRS observations

Host Galaxy	BAT Name	RA	Dec	z	Galaxy Type	Activity	Mod.	Exp.	L_{bol}
MRK 352	SWIFT J0059.4+3150	14.972	31.827	0.014864	S0	Sy1	All	20.1	43.4504
NGC 454	SWIFT J0114.4-5522	18.594	-55.399	0.012158	E/Irr pair	Sy2	All	18.1	43.4333
NGC 526A	SWIFT J0123.8?3504	20.977	-35.066	0.019097	S0/E/Pec	Sy1.9	All	9.4	44.0696
NGC 513	SWIFT J0124.5+3350	21.112	33.799	0.019544	Sb/c	Sy2	HR	10.2	43.515
NGC 612	SWIFT J0134.1-3625	23.491	-36.493	0.029771	SA0/E/Pec	Sy2	LR	6.2	44.1008
ESO 297-G018	SWIFT J0138.6?4001	24.655	-40.011	0.025227	Sa	Sy2	All	22.7	44.1314
NGC 788	SWIFT J0201.0-0648	30.277	-6.816	0.013603	SA0	Sy2	All	20.4	43.6406
IC 1816	SWIFT J0231.6-3645	37.963	-36.672	0.016945	SBa/b	Sy2	All	28.0	43.5994
NGC 973	SWIFT J0234.1+3233	38.584	32.506	0.016195	Sb	Sy2	All	25.5	43.6393
ESO 198-024	SWIFT J0238.2-5213	39.582	-52.192	0.0455	E	Sy1	All	21.5	44.3564
ESO 417-G006	SWIFT J0256.4-3212	44.090	-32.186	0.016291	SA0/a	Sy2	All	25.3	43.3953
ESO 548-G081	SWIFT J0342.0-2115	55.515	-21.244	0.01448	SBa	Sy1	LR	6.2	43.6878
PGC 13946	SWIFT J0350.1-5019	57.599	-50.310	0.036492	pair?	Sy2	LR	5.0	43.9484
ESO 549-G049	SWIFT J0402.4-1807	60.607	-18.048	0.026291	Sb	Sy1	LR	3.9	43.9362
ESO 157-G023	SWIFT J0422.7-5611	65.601	-56.226	0.04353	SBbc	Sy2	LR	5.0	44.2311
MCG -02-12-050	SWIFT J0438.2-1048	69.559	-10.796	0.036352	SBab	Sy1.2	LR	5.0	44.1267
MCG -01-13-025	SWIFT J0451.4-0346	72.923	-3.809	0.015894	$SAB0^{+}$	Sy1.2	All	25.3	43.4249
CGCG 420-015	SWIFT J0453.4+0404	73.357	4.062	0.02939	Sa	Sy2	LR	3.9	44.5097
LEDA 178130	SWIFT J0505.8-2351	76.441	-23.854	0.035041		Sy2	LR	3.9	44.4096
ARK 120	SWIFT J0516.2-0009	79.048	-0.150	0.032713	Sb	Sy1	All	12.3	44.6419
IRAS 05218-1212	SWIFT J0524.1-1210	81.027	-12.167	0.049	S?	Sy1.5	LR	5.0	44.6919
2MASX J05580206-3820043	SWIFT J0557.9-3822	89.508	-38.335	0.03387	S0?	Sy1.2	All	12.2	44.8057
ESO 005-G004	SWIFT J0601.9-8636	91.424	-86.632	0.006228	Sb	Sy2	All	12.2	42.8695
ESO 121-IG028	SWIFT J0623.9-6058	95.940	-60.979	0.040521	SB0/a	Sy2	LR	5.0	44.1318
ESO 426-G002	SWIFT J0623.8-3215	95.943	-32.217	0.022429	SB0/a	Sy2	LR	5.0	43.8687
UGC 03601	SWIFT J0655.8+3957	103.956	40.000	0.017122	?	Sy1.5	All	29.2	43.378
UGC 04013	SWIFT J0747.5+6057	116.871	60.934	0.029255	Sb	Sy1	LR	5.0	43.8883

Table 3.1: (continued)

Host Galaxy	BAT Name	RA	Dec	z	Galaxy Type	Activity	Mod.	Exp.	L_{bol}
CGCG 118-036	SWIFT J0800.5+2327	119.973	23.390	0.029183	Sa	Sy2	LR	3.9	44.0992
MRK 18	SWIFT J0902.0+6007	135.493	60.152	0.011088	E/S0	Unknown	All	12.0	43.0156
2MASX J09043699+5536025	SWIFT J0904.3+5538	136.154	55.601	0.037142	Asym.	Sy1	LR	5.0	43.8206
2MASX J09112999+4528060	SWIFT J0911.2+4533	137.875	45.468	0.026782	S?	Sy2	LR	5.0	43.616
MCG -01-24-12	SWIFT J0920.8-0805	140.193	-8.056	0.019644	SABc	Sy2	All	12.2	43.9343
MCG +04-22-042	SWIFT J0923.7+2255	140.929	22.909	0.032349	SBa	Sy1.2	All	21.5	44.3521
MCG -05-23-016	SWIFT J0947.6-3057	146.917	-30.949	0.008486	S0	Sy2	All	6.6	43.9478
ESO 374-G044	SWIFT J1013.5-3601	153.333	-35.983	0.028453	SBab	Sy2	LR	5.0	44.0679
MRK 417	SWIFT J1049.4+2258	162.379	22.965	0.032756	E	Sy2	LR	3.9	44.2035
UGC 06728	SWIFT J1143.7+7942	176.317	79.682	0.006518	SB0/a	Sy1.2	All	8.5	42.6818
LEDA 088639	SWIFT J1145.6-1819	176.419	-18.454	0.032949	Irr	Sy1	LR	5.0	44.3341
CGCG 041-020	SWIFT J1200.8+0650	180.241	6.806	0.036045	Sa?	Sy2	LR	5.0	44.0843
ARK 347	SWIFT J1204.5+2019	181.124	20.316	0.022445	Sb	Sy2	LR	3.9	43.9339
NGC 4102	SWIFT J1206.2+5243	181.596	52.711	0.002823	Sb	Liner	All	12.2	43.0138
MRK 50	SWIFT J1223.7+0238	185.851	2.679	0.023433	S0	Sy1	LR	10.1	43.618
NGC 4388	SWIFT J1225.8+1240	186.445	12.662	0.008419	SAb	Sy2	All	10.1	43.9542
NGC 4395	SWIFT J1202.5+3332	186.454	33.547	0.001064	SA	Sy1	All	38.8	40.8909
ESO 506-G027	SWIFT J1238.9-2720	189.727	-27.308	0.025024	$S0^{+}$	Sy2	LR	3.9	44.376
NGC 4686	SWIFT J1246.6+5435	191.666	54.534	0.016735	Sa	Xbong	All	29.1	43.3825
SBS 1301+540	SWIFT J1303.8+5345	195.998	53.791	0.0299	S0+	Sy1	LR	5.0	43.9101
ESO 323-077	SWIFT J1306.4-4025	196.609	-40.415	0.015014	$SB0^{0}$	Sy1.2	All	12.2	44.1621
NGC 4992	SWIFT J1309.2+1139	197.273	11.634	0.025137	Sa	Liner	LR	5.0	44.1043
MCG -03-34-064	SWIFT J1322.2-1641	200.602	-16.729	0.016541	S0/a	Sy2	All	16.2	44.4553
NGC 5252	SWIFT J1338.2+0433	204.566	4.543	0.022975	S0	Sy2	LR	12.3	44.2495
UM 614	SWIFT J1349.7+0209	207.470	2.079	0.0327	Sb	Sy1.8	LR	5.0	43.9079
ESO 511-G030	SWIFT J1419.0-2639	214.843	-26.645	0.022389	SAc	Sy1	LR	5.0	43.8871

Table 3.1: (continued)

Host Galaxy	BAT Name	RA	Dec	z	Galaxy Type	Activity	Mod.	Exp.	L_{bol}
NGC 5728	SWIFT J1442.5-1715	220.600	-17.253	0.009353	SABa	Sy1.9	All	14.3	43.4996
MRK 501	SWIFT J1654.0+3946	253.468	39.760	0.033663	E	BLLac	LR	5.0	44.2059
ESO 140-G043	SWIFT J1844.5-6221	281.225	-62.365	0.014178	SBb	Sy1	All	18.1	44.0215
ESO 141-G055	SWIFT J1921.1-5842	290.309	-58.670	0.037109	Sc?	Sy1.2	All	12.2	44.6239
2MASX J19595975+6508547	SWIFT J1959.6+6507	299.999	65.1485	0.047	E	BLLac	LR	5.0	44.3525
UGC 11871	SWIFT J2200.9+1032	330.175	10.550	0.026612	Sb	Sy1.9	LR	3.9	44.1528
NGC 7172	SWIFT J2201.9-3152	330.508	-31.870	0.008683	Sa	Sy2	All	8.0	43.6536
MRK 915	SWIFT J2236.7-1233	339.194	-12.545	0.024109	Sa	Sy1.5	LR	3.9	44.005
UGC 12282	SWIFT J2258.9+4054	344.731	40.932	0.016992	Sa	Sy1.9	All	29.2	43.4035
NGC 7582	SWIFT J2318.4-4223	349.598	-42.371	0.005254	SBab	Sy2	All	4.6	43.3317
LEDA 089420	SWIFT J2325.5-3827	351.351	-38.447	0.0359	S0	Sy1	LR	5.0	43.8717
NGC 7682	SWIFT J2328.9+0328	352.266	3.533	0.01714	SBab	Sy2	All	29.2	43.3196
UGC 12741	SWIFT J2341.8+3033	355.481	30.582	0.017445	Sa	Sy2	All	29.2	43.2473

3.2 Data Reduction

The data for each of our objects are reduced using an identical process. The data were downloaded using Leopard, the Spitzer Science Center's original data archive tool. Since 2010, the Center has switched to the Spitzer Heritage Archive, a web based tool with similar capabilities. Each observation is split into an Astronomical Observation Request (AOR) with a subsequent number used for sorting. High-resolution background observations are frequently given their own AOR number. Initially, every observation is checked by eye using the overlay tool, which allows the slit positions to be projected onto other FITS photometric images. This confirmation of targeting allows for verification that each slit contains the object of interest as well as allowing for classification of the adjacent features such as heavy extended host galaxy contamination. Where available, MIPS, IRAC, and SDSS data are used in this process. Similarly, the background observations are checked for contamination. Through this process we have insured that all of our AGN are contained within their slits; observed some galaxies with non-negligable galactic features in their low-resolution subtraction regions (i.e. Section 4.3); and verified that none of our high-resolution background observations contain bright objects that would render them useless.

Basic calibrated data (BCD) files are downloaded with all relevant calibration files. The BCDs have already undergone the batch mode, non-interactive pipeline. This includes tasks such as correction for cosmic rays and an estimation of the slope of the linearized data signal ramps as described in the IRS Pipeline Handbook. The BCD

files that we use are the fully processed 2d spectroscopic data, pixel status masks, traceable uncertainty images, and droop images tracing flux in unilluminated pixels. I carry out further reduction by using the contributed IDL software DARK_SETTLE. This package removes scalloping and order mismatch in the Long High module data by removing time-dependent non-uniform dark currents. Next, we make 2d sky subtracted images for each data file. This is done prior to data extraction as advised by the Spitzer Science Center help desk in order to minimize errors. All of our high-resolution data sets are accompanied by off-target observations generally obtained within minutes of the original observation with an identical observation strategy to our target strategy. Because the low-resolution data are taken from two slits, half of a given observation is always off-target. These off-target data are used as the background image with important caveats. First, the off-target slit is not necessarily empty. The slit centers are only separated by 79-192 arcsec so that light from the host galaxy flux could be included in the integrated spectrum for nearby, extended host galaxies. Secondly, this observing strategy means off-target observations are taken on different sides of the object for the two orders of a given module. This, combined with the roughly perpendicular SL and LL slits, means that background images are taken from four distinct regions surrounding the central object (see Figure 3.2). The on-target and off-target unextracted data images are subtracted directly, with errors added in quadrature for each pixel. The pixel status masks are combined with a bit-wise OR command that notes flags for each pixel from both masks. After subtracting

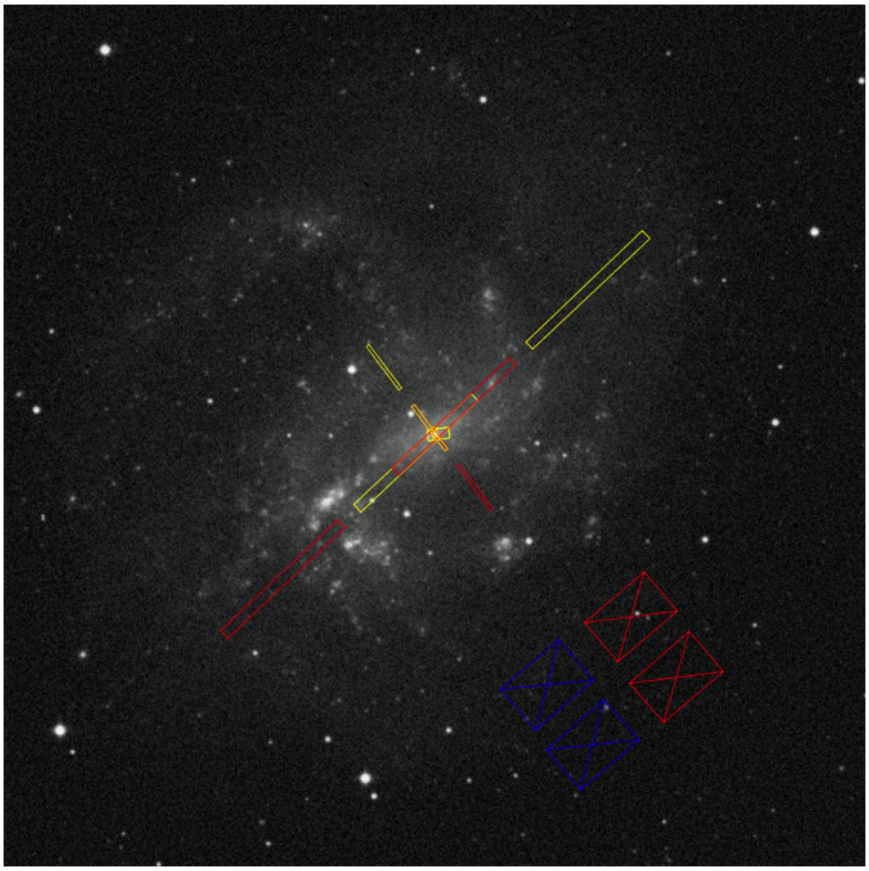

Figure 3.2: NGC 4395 SDSS image with selected slit overlays. For low-resolution apertures, yellow represents the first slit, red denotes second slit. High-resolution background images are outside of field of view. Crossed rectangles represent peak-up array apertures while not in use.

the background, the resulting 2d spectrum is cleaned of rogue pixels using IRS_CLEAN. This interactive IDL tool creates bad pixel masks using a built-in algorithm that detects extremely bright lone pixels or clusters of pixels. After a rogue pixel is found, the program determines a flux profile according to the neighboring row, normalizes it to the remaining pixels in the affected row, and substitutes for the rogue.

The spectrum is next extracted using the Spitzer IRS Custom Extraction (SPICE) software. The high-resolution data are extracted over the entire slit without slit-

loss corrections (the default for point source high-resolution extraction). The low-resolution data were extracted over a computer defined region tracing a peak ridge in the spatial dimension. This extraction width in the spatial direction shrinks with decreasing wavelength. The output of the data extraction is a calibrated 1d flux spectrum covering all the orders for a given module. The edges of each order are contaminated with large flux errors due to the effects of the chip edges. In order to mitigate these errors, the order overlap regions (where data are present from two orders) are trimmed. This is most easily carried out using the Spectroscopic Modeling Analysis and Reduction Tool (SMART) because of its superior GUI interface. Trimming is done manually to insure that all usable data are incorporated. Spurious data are only removed when an adjacent, well-behaved region of another order can be used in its place. Following trimming, the data are binned to match the spectral resolution of the module at each wavelength. Each bin averages over overlapping orders as well as over multiple cycles and positions (nods) of the same object with 2σ clipping. The systematic uncertainty for each point is combined with the random uncertainty in quadrature.

3.3 Modeling

3.3.1 XSPEC

I model the data using the spectral fitting package originally designed for analyzing X-ray data, XSPEC (Arnaud, 1996). The primary advantage of this modeling technique is the ease of adding user-defined models. With the help of Keith Arnaud (NASA/GSFC/UMD), a script was implemented in order to prepare our binned one-dimensional output for XSPEC. The instrumental response of each module at every wavelength was incorporated so that a theoretical model can be fitted to all the data sets simultaneously. Models are fitted using a χ^2 minimization technique with a modified Levenberg-Marquardt algorithm. Model parameters are either frozen (e.g., redshift) or limited to narrow ranges based on results from prior observations and model feasibility (e.g., estimated bolometric luminosity). One-dimensional errors are determined by varying a single parameter within its allowed range while refitting the non-frozen parameters until $\chi^2/\nu > 2.706$. This threshold defines the 90% confidence interval for the single parameter. This process also replaces the tested parameter with a better value if a lower χ^2 is found. The iterative fitting technique insures that the model is not trapped in a local minimum by testing a large portion of possible parameter space. The drawback of this approach is that the estimated errors cannot exceed the parameter range limits. Multiple models can effortlessly be fit simultaneously. Additionally, observations can be split into groups so that some parameters

can be allowed to vary while others remain the same while fitting all the data simultaneously. This allows us to investigate spectral components that vary with time and with aperture (see Section 4.7).

We have amassed a small collection of infrared models from the literature to capture the underlying physics of the AGN. Several of the models used are sparsely populated multidimensional grids that XSPEC is capable of interpolating between for each free parameter. Our models include the effects of both the AGN and the host galaxy and are designed to be as self-consistent as possible. The use of published models allows us to include all the relevant physics while exploring the efficacy of the most recent and detailed models in the field. While most of our models are previously computed, we are required to reproduce the simulations of our NLR models as they are not available publicly. Additionally, although already simulated and available, our torus models require a selection of parameters that are evenly distributed and complete across our desired parameter ranges. Figure 3.3 shows a cartoon depicting a typical AGN including regions of IR emission that we model.

3.3.2 Host Galaxy Dust Model

In order to model the contribution of host galaxy star formation regions, we use infrared spectral models assembled by Draine & Li (2007, hereafter, DL07) to describe the dust that is heated by starlight. These models assume a mixture of carbonaceous grains, amorphous silicate grains, and polycyclic aromatic hydrocarbons (PAHs) with

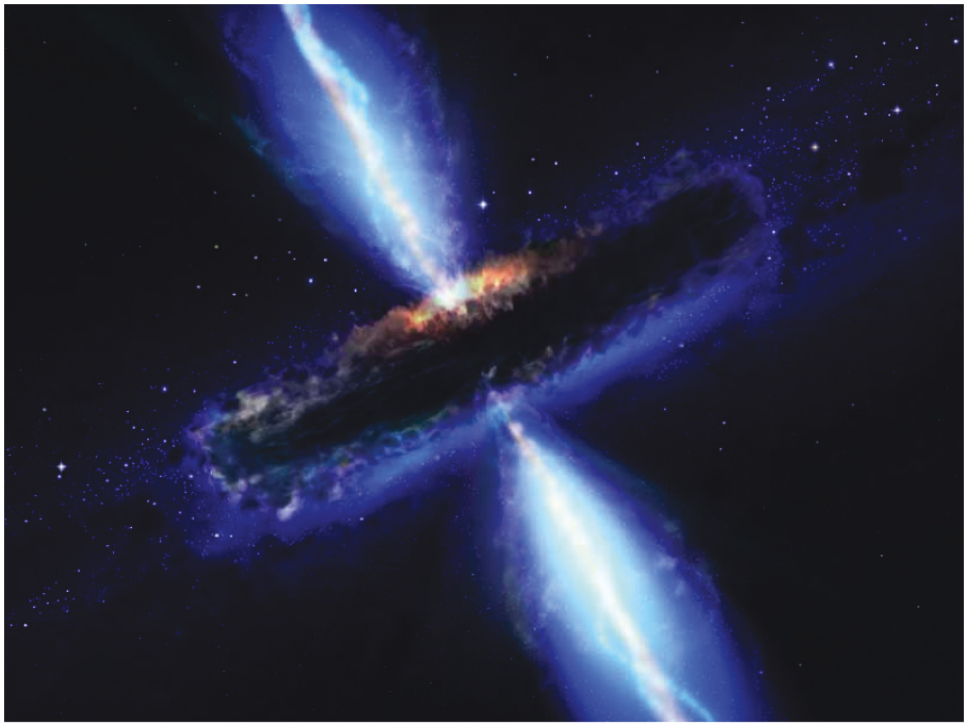

Figure 3.3: Cartoon of an AGN at the center of a nearby galaxy. Shown are the molecular torus that surrounds the BLR and accretion disk in this edge-on view. The jets emerge along the axis of the SMBH rotation and highlight the location of the NLR clouds that are lit up by the AGN.

size distributions capable of reproducing the extinction curve of the Milky Way. The only dust composition parameterization required is q_{PAH}, the PAH mass fraction, which is given a range of 0.47 to 4.58% by DL07. This variable is used by DL07 to distinguish between varying grain size distributions used by Weingartner & Draine (2001) to reproduce extinction curves on Milky Way sightlines characterized by $R_V \equiv A_V/(A_B - A_V) = 3.1$, a value typical for the diffuse ISM. Although the set of models defined by this range of q_{PAH} certainly does not encapsulate all possible dust grain size distributions, extending the modeling to outside this range is beyond the scope of this work. Instead, we allow for a larger range of silicon extinction using dust

absorption models that are applied to AGN and host galaxy models when needed (see Section 3.3.5).

The absorption properties of the PAHs are derived from spectral observations of local galaxies as well as laboratory data (DL07, references therein). The models include the effects of single-photon heating. Starlight intensity is parameterized by the dimensionless scaling factor U, the starlight intensity relative to the local interstellar radiation field. Because the starlight intensity will vary substantially within a galaxy, DL07 use a distribution of U values defined as a delta function at U_{min}, and a power-law (U^{α}) between $U_{min} < U < U_{max}$ with exponent α. These components represent diffuse ISM dust and circumstellar dust respectively. DL07 find that a large sample of SEDs can be suitably fit with $U_{max} = 10^6$ and $\alpha = 2$ so we freeze these parameters in our model. The fraction of dust which is circumstellar is γ ($U > U_{min}$). The parameters defining a given model curve are q_{PAH}, U_{min}, and γ. The parameter ranges tested ($\gamma = 0 - 1, U_{min} = 0.1 - 25, q_PAH = 0.47 - 4.58\%$) should be capable of fitting a variety of galaxy spectra (DL07). The dust mass (M_{dust}) can be derived from the normalization parameter. A small subset of the SED's are plotted in Figure 3.4

3.3.3 Clumpy Torus Model

Following the example of M09, we use the clumpy torus models of N08 in order to account for the equatorial dust surrounding the AGN. The model postulates a distri-

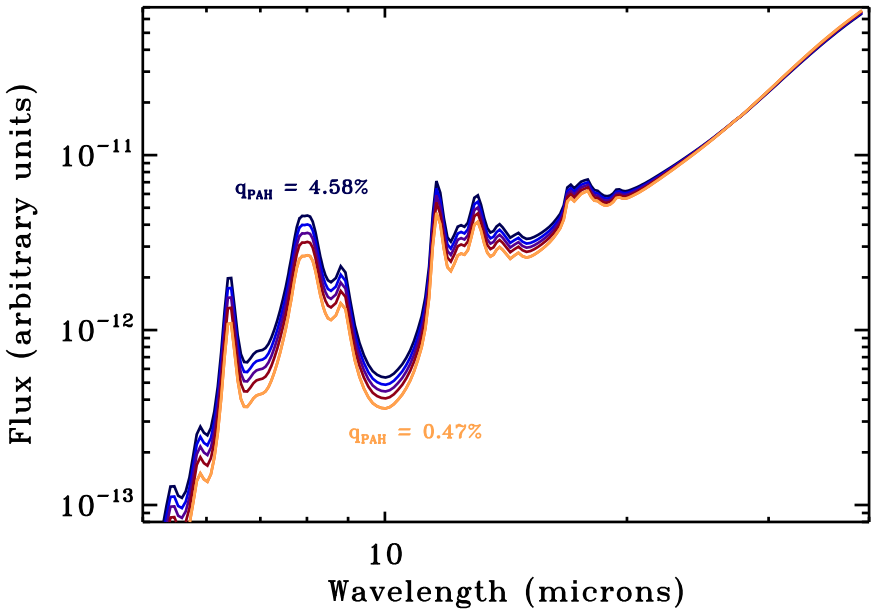

Figure 3.4: Selection of host galaxy SEDs with varying q_{PAH}

bution of identical dust clouds each with optical depth τ_v surrounding the accretion disk emission, defined as a piecewise power-law spectrum (N08, references therein). Occupying a toroidal volume, these clumps are distributed radially with a power-law defined density r^{-q} and a sharp cutoff that is some multiple of the inner radius ($Y = R_o/R_i$). The poloidal angular distribution of clouds is Gaussian with width σ. The overall density of clouds is defined by the mean number of clouds along a radial equatorial line N_0. The resulting AGN classification is therefore only probabilistically dependent on viewing angle i (see Figure 3.5).

The probability of photon escape ($P_{esc} = e^{-N_0 * e^{-\beta^2/\sigma^2}}$ where $\beta = 90° - i$ from N08) corresponds to the probability that the accretion disk surrounding the SMBH is

unobscured, which is dependent on N_0, i, σ, and τ_v. For those AGN displaying broad emission lines, P_{esc} could be used as a model constraint to approximate a reasonable probability of photon escape. We refrain from using this constraint in order to test the efficacy of our models. Given the three parameter dependence and limited features of some of our models in the IR, we do not expect every model to accurately predict AGN inclination and type (via P_{esc}). Our analysis (Section 6.2) will show that for this ensemble of objects our models faired well in matching known AGN type.

The cloud distributions inner radius R_i is set by the AGN bolometric luminosity (L_{bol}) and the sublimation temperature of the composite dust, a grain mixture with standard interstellar properties (N08). L_{bol} is used to scale the flux of the model but has no effect on the spectra curvature. This is because an increase in bolometric luminosity will spread the torus brightness over a larger area while maintaining an identical dust temperature distribution when scaled by the inner radius (R_i) (N08 section 2.3, and appendix A). We discuss the methodology for determining L_{bol} in Section 3.3.6. The radiative transfer code DUSTY (Ivezic & Elitzur, 1997) is used to determine the radiative properties of individual dust clouds whose ionizing spectra vary depending on location. The CLUMPY (N08) software determines global emission properties that depend on the cloud distribution and viewing angle. The free parameters (and tested parameter ranges) of the model are τ_v $(10-100), q$ $(0-1), Y$ $(5-60), \sigma$ $(15-75^\circ)$, and i $(0-90^\circ)$. A model grid is assembled using a sparse but complete grid of 7,680 of the $\sim$1.4 million previously computed models available online spanning the plausible

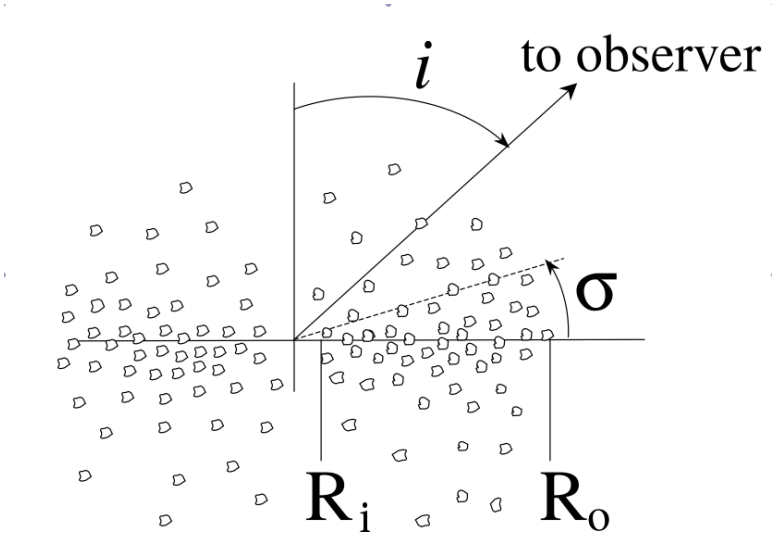

Figure 3.5: Diagram of the equatorial obscuration region taken from N08. Labeled are i, the inclination from disk normal to the observer; σ, the angle of Gaussian distribution from the plane of the torus; R_i, the sublimation temperature and bolometric luminosity determined torus inner radius; and R_o, the torus outer radius

parameter space. A subset of the resulting SEDs is shown in Figure 3.6.

3.3.4 Narrow Line Region Model

The Narrow Line Region (NLR) emission has been previously modeled by G06 in a manner that we reproduce with an extended parameter space. Using the MAPPINGS IIIR code, we compute the IR emission spectra of a cloud of dust with a given size, composition, and a given local radiation field using appropriate dust physics including stochastic heating. The model input parameters are well described and justified by G06 and S08 and will be briefly summarized here. The dust is presumed a combination of graphitic and silicaceous grains with a modified grain shattering profile size distribution (with index $\alpha = -3.3$). PAHs are thought to be destroyed in the

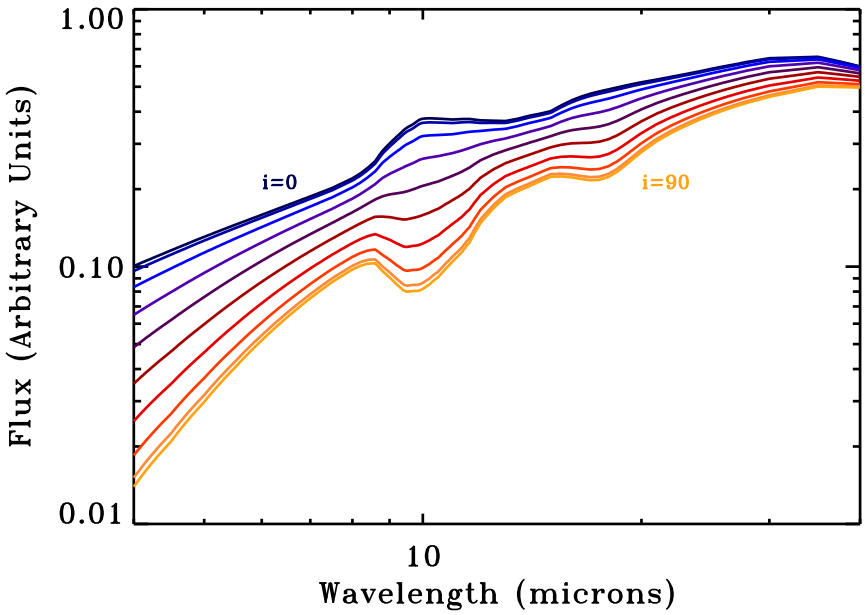

Figure 3.6: Selection of clumpy torus SEDs with varying inclination

NLR through photo-dissociation by the hard AGN radiation and thus we omit them from the model. Solar abundances and local ISM depletion factors are used (Dopita et al., 2005, references therein). The input ionizing spectrum is a combination of two power-laws with exponential cut-offs similar to that used by N08 (G06, see their Figure 1). A constant density structure is assumed for simplicity with $n(H) = 10^4 \mathrm{cm}^{-3}$ (S08). The column density is limited to $N_H = 10^{21.5} \mathrm{cm}^{-2}$ (G06, S08). The flux of the model is determined by the covering factor of the NLR. The only other free parameter in this model is the ionization parameter (U), a dimensionless ratio relating the ionizing flux to the particle density $U = F_{ion}/n_H c$. We test ten ionization parameters between $\log U = 1$ and -4.3 which XSPEC can interpolate between. The

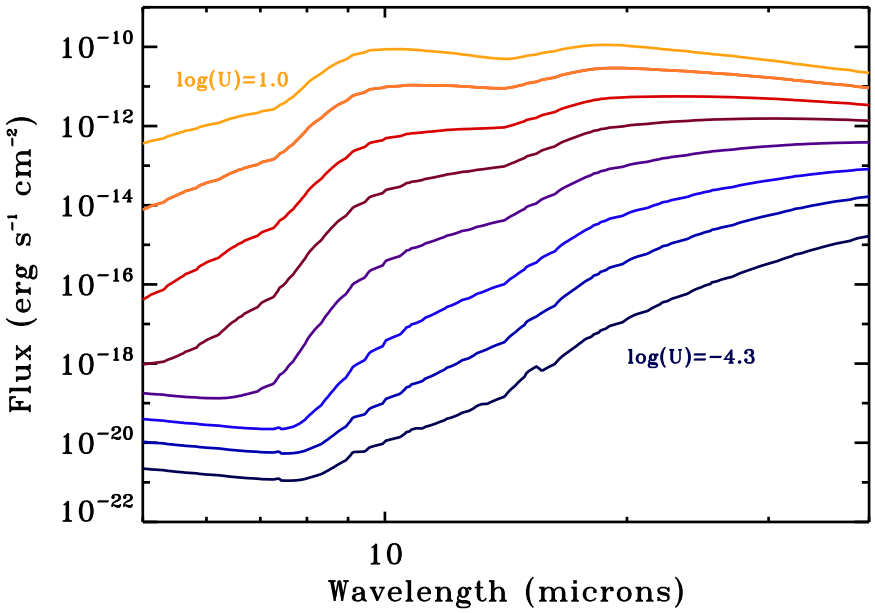

Figure 3.7: NLR SEDs with varying ionization parameter

range of ionization parameters are typical of NLRs (S08) with the high value (log $U = 1$) being an extreme case and the low value (log $U = -4.3$) being too cool to contribute significant emission for our observations. For each of 80 logarithmically binned dust sizes, absorption, scattering, and photoelectric heating is calculated to derive a probabilistic temperature distribution. This in turn is used to determine the IR re-emission spectrum (Figure 3.7) with quantum fluctuations (G06).

3.3.5 Silicate Absorption Model

We incorporate a multiplicative extinction curve in our modeling to account for silicate absorption at 9.7 and 18 μm that is not associated with the AGN. Silicate dust in the Milky Way and host galaxy ISM is responsible for the strongest IR galactic absorption features (Li, 2007). Although this creates a silicate absorption degeneracy with the AGN, the exact absorption profiles differ in the two markedly different environments (Li, 2007). Our models are based on the extinction curves used by PAHFIT (Smith et al., 2007), a *Spitzer* IRS spectral decomposition algorithm that emphasizes the recovery of silicate absorption features. Our first attempt at modeling extinction (parameterized as $S_{type} = 3$) uses a model that linearly combines tabulated silicate absorption lines and a power-law with an exponent of 1.7 (Smith et al., 2007). The 9.7 μm profile is taken from a Galactic center study between 8.0 and 12.5 μm (Kemper et al., 2004). The 18 μm feature is given a Drude profile, a slightly asymmetric profile for a classically damped harmonic oscillator similar in shape to a Lorentzian profile (Smith et al., 2007). The relative strength of the power-law is allowed to remain a free parameter ($\beta = 0$ to 1). We also attempt to fit our data with two other extinction curves derived from Chiar & Tielens (2006). They utilize Milky Way observations to define a local ISM extinction curve and a galactic center extinction curve (labeled as $S_{type} = 0$ and 1 respectively). Longward of the tabulated data at 30 μm, a power-law with an exponent of 1.7 is used with no additional free parameter. We normalize all three curves with their optical depth at 9.7 μm.

3.3.6 Bolometric Luminosity

We use the IR data combined with hard X-ray fluxes in order to define a bolometric luminosity used to both scale our clumpy torus model and to determine geometric ramifications of our best-fit NLR model. The NLR model is unaffected by the bolometric luminosity as the only variable that effects spectral shape is the ionizing flux parameter. An accurate bolometric luminosity is required however to determine the NLR radius and covering factor (Section 6.3).

To create an unbiased bolometric luminosity catalog for our objects we combine the hard X-ray *Swift* BAT fluxes with the integrated *Spitzer* IR spectra flux. This avoids the double counting problem caused by absorption in the optical, UV, and 0.1-10 keV regimes that are reprocessed into the IR. This approach is similar to that of Vasudevan et al. (2010), who combine *Infrared Astronomical Satellite* (IRAS) and *Swift* BAT fluxes to determine bolometric luminosity for an IR and hard X-ray flux limited sample of AGN. Our IR data features substantially smaller aperture size compared to the instruments of IRAS simplifying host galaxy subtraction. Also, inherent to our IR modeling is the ability to subtract the host galaxy IR contribution and thus we are able to isolate the AGN IR emission with our detailed spectral models. The fitting of IR emission is an iterative process as the bolometric luminosity affects the normalization of the clumpy torus model. We refit our models until the bolometric luminosity used to normalize the torus model is within 2.5% of the measured (IR and hard X-ray) bolometric luminosity. The resulting AGN IR emission is added to the

hard X-ray (14-195 keV) emission from the 70-month *Swift* BAT catalog (Baumgartner et al., 2012) utilizing the longest exposure times available in order to average out variability. Our IR data lacks this long exposure time, meaning IR variability can affect our resulting luminosities. We predict that the *Spitzer* IRS misses cooler IR emission but this emission is generally dominated by host galaxy cool dust emission. The total bolometric luminosities are listed in Table 3.1.

3.4 Previous Attempts to Model the IR Continuum

Initial attempts at IR continuum fitting primarily tested individual model geometries on large samples of AGN using photometric observations (Pier & Krolik, 1993; Efstathiou & Rowan-Robinson, 1995, e.g.,). The use of *Spitzer* IRS data allows for substantially more detailed models and more robust spectral fitting. As previously mentioned, G06 create a set of NLR cloud models in an attempt to explain both observed emission line fluxes and dusty continuum emission. Follow-up work (S08) uses high-resolution IRS spectra to evaluate the effectiveness of their NLR models. Using IRS observations of a sample (Guyon et al., 2006) of 23 Palomar-Green AGN (Schmidt & Green, 1983), S08 fit IR spectra after subtracting a normalized M82 template to account for host galaxy flux. The remaining emission is modeled with up to four blackbody curves (representing the torus and cool host galaxy dust) and the

NLR dust component. All emission lines were removed with the gaps ignored in the fitting routine. Error is redefined so that it is proportional to the inverse, square-root of the local sampling density to insure that better sampled regions do not dominate the fit (S08, equation 4). The error is also proportional to the flux of a best fit power-law in the vicinity of the individual data points (S08, equation 4). This ignores the systematic error of individual datum and minimizes the contribution of data that deviate from a power-law.

M09 fit the same data sets using N08 clumpy torus models instead of multiple blackbodies models. They similarly handle host galaxy emission with subtraction of a static M82 template before fitting the remaining models. In order to eliminate the emission lines, M09 bin the data into 100 equally spaced energy bins effectively smoothing any lines. The error is not propagated through this binning; it is redefined as 10% of the flux in each bin. The resulting χ^2 statistic is said to be "different" then the one normally used in statistical analysis. They find that even with the use of the N08 torus model, an additional blackbody component is required to explain low wavelength emission. This is explained as purely carbonaceous dust within a radius defined by the silicate dust sublimation temperature (M09). The graphitic dust would have no impact on the prominent silicate absorption/emission features that the N08 model attempts to model. After publication, it was revealed that the N08 model code used before 2010 contained an error resulting in incorrect normalizations (see erratum, Nenkova et al., 2010). The exact impact on the models of M09 are unknown, but we

must assume the resulting fits are collectively less reliable.

M12 applied similar fitting techniques to an expanded group of 115 nearby ($z < 0.2$) Type 1 AGN derived from work by Sani et al. (2010) combined with the M09 sample. The model fitting of M12 utilizes more sophisticated host galaxy model subtraction by using the best fitting of five star formation templates. The templates are normalized so that the remaining 7.7 μm flux (a PAH feature emitted by galactic dust) is less than the noise at that wavelength. Although this technique is more flexible, M12 report that for some spectra the host galaxy flux exceeds the observed flux in narrow wavelength ranges (e.g., $6.5 - 7.5\mu$m) rendering the remaining AGN SED "meaningless." The clumpy model is updated with the correct normalizations, but M12 report that using the *exact* techniques of M09, they are incapable of fitting their sample of Type 1 AGN with low inclination models. Because the low inclination models are brighter than their spectra, they introduce an additional normalization to the torus model. M12 justify this by suggesting the graphitic dust of M09 might block a significant fraction of the AGN luminosity and reradiate in the IR. The graphitic dust is modeled with an additional cloudy model with five input parameters. The resulting model spectrum appears very similar to multiple summed blackbody spectra. The data are binned and error estimated identically to M09.

In previous attempts to model the IR AGN continuum (e.g., S08, M09, M12), silicate absorption by the host galaxy is ignored. Work modeling starburst galaxies (e.g., Brandl et al., 2006; Smith et al., 2007) utilize silicate absorption components

in order to recover the observed 9.7 μm absorption feature in these inactive galaxies. Although introducing these multiplicative models into our fitting algorithm adds complexity, there is little doubt that silicate dust absorption occurs in galactic dust as well as the AGN torus (Li, 2007).

Our work utilizes both theoretical models and fitting procedures previously used while improving the methodology, host galaxy modeling technique, and sample selection. Our host galaxy model is considerably more flexible than the templates previously used and is capable of reproducing PAH features that match our data. Because we fit our host galaxy at the same time as the rest of our AGN models the statistical uncertainty of the stellar subtraction is propagated instead of being ignored. We use the updated torus models of N08 eliminating the incorrect normalizations that affect the M09 results. We choose not to incorporate the more detailed graphitic dust models of M12 because we lack the spectral coverage to justify the additional parameters required with a such a complex model. Additionally, we are capable of producing torus models of all orientations that correlate well with model type (see Section 6.2). Our statistical approach is considerably more robust than our predecessors as we do not redefine the errors of our data. This results in fit statistics that lack artificial deflation and reflect the actual ability of our models to fit the data (Section 5.2). Several of our model components require the use of the AGN bolometric luminosity which we have estimated using hard X-ray and IR flux (Section 3.3.6). All the previously mentioned authors utilize bolometric correction factors to derive

the bolometric luminosities from the 5100 Åluminosity (i.e., $L_{bol} = 9 \times L_{5100\mathring{A}}$). Our L_{bol} values are inherently time averaged in the hard X-ray and require no correction factor. The most fundamental difference with our work however is the application torus modeling to a significantly less biased catalog that includes AGN of all types. Prior to our work, these models have never been applied to obscured AGN.

Chapter 4

A Detailed Example of Applying Data Techniques

4.1 NGC 4395

NGC 4395 was initially chosen as the first to be modeled because it is the nearest object in our sample ($z = 0.00106$). The essentially bulgeless Sd dwarf galaxy contains the faintest known Seyfert 1 nucleus (Filippenko & Sargent, 1989) with $L_{bol} \sim 1.2 \times 10^{41}$ erg s^{-1}. The galaxy is located at a distance of 4.0 ± 0.3 Mpc (Thim et al., 2004). It was found through reverberation mapping (see Section 1.2.2) to contain a central black hole with $M_{BH} = (3.6 \pm 1.1) \times 10^5 M_\odot$ (Peterson et al., 2005). From the most recent BAT survey, 9.4 months of integrated observation time over the course of 58 months reveal a time averaged hard X-ray luminosity $L_{14-195keV} = 5.77 \pm 0.99 \times 10^{42}$

erg s^{-1} (Baumgartner et al., 2012). Broad emission lines dominate the optical and UV spectra (Filippenko & Sargent, 1989; Filippenko et al., 1993; Moran et al., 1999). Wrobel & Ho (2006) present radio data resolving weak radio emission indicative of an outflow.

NGC 4395 is highly variable. Soft X-ray variability was well observed by Vaughan et al. (2005) using a 90 ks *XMM-Newton* observation ($0.2 - 10$ keV). The fractional excess rms variability amplitude is reportedly over 100% making it one of the most variable known AGN. Half of a 17 ks *Chandra* observation ($0.3 - 10$ keV) revealed transient quasi-periodic behavior lasting at least 11 cycles with a period of $\sim$400 s (Moran et al., 2005). Similar oscillation was tentatively reported in another 30 ks *Chandra* observation with a period of 341 s, but the authors failed to find the feature in a second identical *Chandra* observation or *XMM-Newton* data (O'Neill et al., 2006). Variations in spectral softness (counting rate ratio between the $0.4 - 3.4$ keV and $3.4 - 8.0$ keV bands) that have been attributed to enhanced soft X-ray variability are thought to be the result of variations in absorbing material in the line of sight (O'Neill et al., 2006).

The optical continuum varied by a factor of ~ 2.2 at 3800Å over the course of six months while B- and I-band observations demonstrate 20% variability in one day (Lira et al., 1999). Cross-correlation analysis shows that the optical emission lags behind UV and X-ray emission by 24^{+7}_{-9} and 44 ± 13 minutes respectively, consistent with a model in which X-ray photons are reprocessed into UV and optical photons

(Desroches et al., 2006). Analysis of optical and IR ground based photometric data suggests two variable spectral components; one with intraday flux variations, likely originating from the outer accretion disk, and the other on the monthly timescales, probably thermal emission from toroidal dust (Minezaki et al., 2006).

NGC 4395 represents a unique AGN given its observational history. It serves as a good test bed for our methodology because of its proximity, the availability of many observations at other wavelengths, and the ability to compare our results to previous work. Additionally, its variability and low luminosity allow us to both demonstrate the ease of model fitting with variable parameters in XSPEC as well as demonstrate the applicability of our models down to the lowest luminosities in our sample.

4.2 Observations

Observations of NGC 4395 with the *Spitzer* IRS were taken as part of three separate campaigns with low- and high-resolution observations separated by one year (June 2007 and June 2008 respectively). This time gap is used to compare flux and model shifts over the course of one year. Archival low-resolution observations lasting 1,463 seconds are incorporated into our analysis. Our requested observations totaled 122 seconds in the SH and LH modules, but was immediately followed by 743 seconds of total high-resolution observations requested by another observer. These data sets were combined to reduce errors. The total on-target integration time is 39 minutes.

In addition to the IR data, we examine the concurrent hard X-ray data supplied by the *Swift* BAT in order to identify periods of variability. NGC 4395 was observed over the course of 5.45 years for a total of 9.4 months (Baumgartner et al., 2012). This time was broken up into 28,890 individual observations averaging around 14 minutes with a net S/N of 14.16. We bin these observations using two-month time weighted averages with corresponding errors.

4.3 Photometric Analysis

We verify the astrometry of our observations by overlaying the slit projections onto archival images of our object (Figure 4.1). Extensive prior multiwavelength observations allow us to glean much valuable information regarding what is contained within our slit projections. The slit size varies substantially with module yet, because of our extraction methodology, the extraction area is comparable between high- and low-resolution modules. Within each low-resolution module the extraction area does however vary with wavelength, but our extraction software attempts to correct this.

What parts of the galaxy are contained within the IRS slits? We need to know the answer to this question to be able to model the IR data appropriately. In the *Hubble Space Telescope* (*HST*) ACS image (Figure 4.1), based on the spatial extent of the brightest part of the galaxy nucleus, it appears as if the AGN may not be fully contained within the SL slit projection. Yet analysis of the spatially collapsed

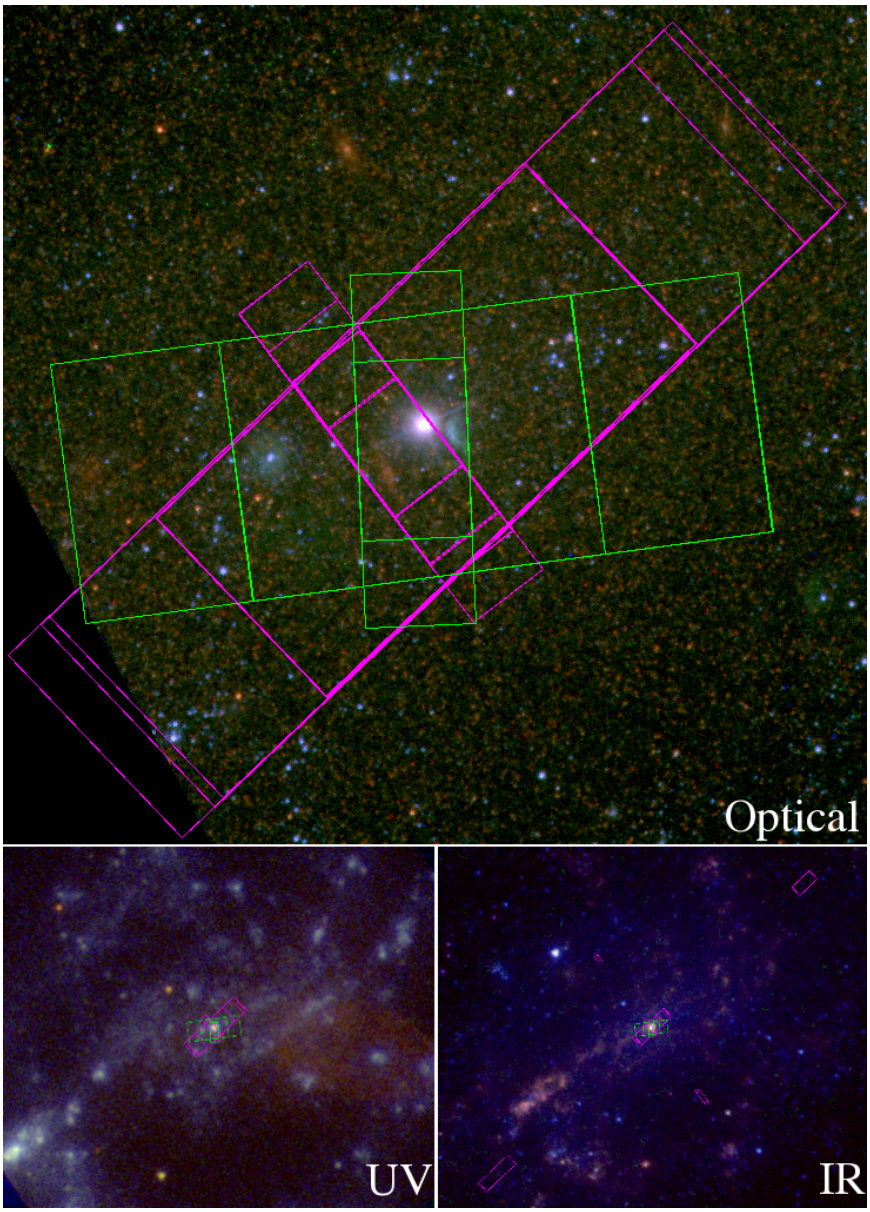

Figure 4.1: NGC 4395 image composite with high (green) and low (magenta) resolution extraction areas projected, clockwise from top; optical: *HST* ACS image using F435FW, F555W, and F814W filters; IR: *Spitzer* IRAC 3.6μm, 5.8μm, and 8.0μm filters; UV: *GALEX* NUV (2267Å), *XMM-Newton* OM UVW1 (2910Å), and U (3440Å) filters.

IRS spectrum from the perpendicularly aligned SL and LL modules confirms that the AGN is actually well centered within the two slits. The failure to completely align the ACS image with the slit projections is a result of the ∼1" absolute astrometry error that each is subject to. The correct *Spitzer* IRS target position is also verified by the peak-up array before observation, and skewing during an observation after initial targeting results in negligible relative pointing error according to the Spitzer IRS manual.

Our UV composite image consisting of the *Galaxy Evolution Explorer* (*GALEX*) near UV filter (2267Å) along with the *XMM-Newton* Opitical/UV Monitor (OM) UVW1 (2910Å) and U (3440Å) filters reveals that several bright knots of presumed star formation are included in both the high- and low-resolution data sets. Additionally, there is diffuse UV emission from the galaxys circumnuclear region likely mapping less dense star formation regions. The *Spitzer* IR Array Camera (IRAC) images complement this by demonstrating the presence of warm circumstellar dust concentrated near the galaxy center.

Diffuse UV radiation is also seen in the low-resolution background observations, which traces faint IR emission between 3 and 9μm. This emission is substantially lower than the nuclear emission. Our high-resolution data are observed to have a fainter subtraction area since the background observation is farther from the galaxy center. Analysis of these regions (via full IRS extraction of the subtraction regions) demonstrates that the background flux differences between modules are within flux

errors when scaled by the extraction area.

Additional structure is apparent in the optical image. Matthews et al. (1999) note two structures at 0.25" and 1" from the nucleus using the WFPC2 B- and I-bands, which they presume to be a nuclear ionization cone, an area of rarefied gas illuminated by the AGN and shaped by the torus shadow. Archival ACS imagery shows the 1 feature as a blue filament just west of the AGN. Presuming they are correct and our pointings are accurate, all NLR regions will be contained within the slits (widths from 3.6" to 11.1"). We can also take into account the orientation of the off-center NLR in order to infer that the disk is not face on. To make a conservative disk inclination minimum hard limit, we take the projected opening angle of the NLR region visible in the archival WFPC2 and ACS images and halve it (opening angle $\sim 40^\circ$ and $i_{min} \sim 20^\circ$). Presuming a conical NLR, this guarantees that the single ionization cone remains on only one side of the AGN as observed.

4.4 Fitting Process

After all of our NGC 4395 data has been reduced and formatted so that it is XSPEC readable, we begin plotting our data and fitting our models. A flux mismatch between high- and low-resolution data sets is apparent, but we first fit all the data with identical models. We begin modeling our spectra using only the clumpy torus and NLR emission models as we presume all AGN contain these features. Our resulting

best-fit model continuum is nearly featureless with a $\chi^2/\nu = 2.65$ (Figure 4.2a). None of the features of the AGN are fit and the model averages between the two disparate continuum fluxes, especially between 10 and 13μm. We note a subtle increase in the quality of the fit with the addition of another NLR model $\chi^2/\nu = 2.52$ (Figure 4.2b), but we feel the complexity of the model can be better matched with components of a different type. Several broad feature are apparent which correspond to PAH emission wavelengths (e.g., 7.7 and 11.3μm). We add our host galaxy component to the model and find that these features are easily accounted for while improving the quality of the fit ($\chi^2/\nu = 2.20$, Figure 4.2c). Inclusion of an additional NLR feature has an incredibly small impact on the fit quality ($\chi^2/\nu = 2.18$, Figure 4.2d) as the two models are nearly identical. The three physically motivated models fail to fit a low wavelength excess below 10 μm that is apparent in the low resolution data. Substantial improvement ($\chi^2/\nu = 1.98$, Figure 4.2d) is made with the inclusion of an 1800 K blackbody (similar to that used by S08 and M09, Section 3.4). We realize that in order to fit the data, our model needs to encapsulate the difference in flux and spectral shape between high- and low-resolution data. Initially, we allow the host galaxy flux to vary between the two data sets ($\chi^2/\nu = 1.42$, Figure 4.2e). This significantly improves the fit quality, but is unsatisfying in the direction of the flux shift.

We presume the cause of the high- and low-resolution flux mismatch is two-fold; our different sized module slits encapsulate different amounts of extended host galaxy

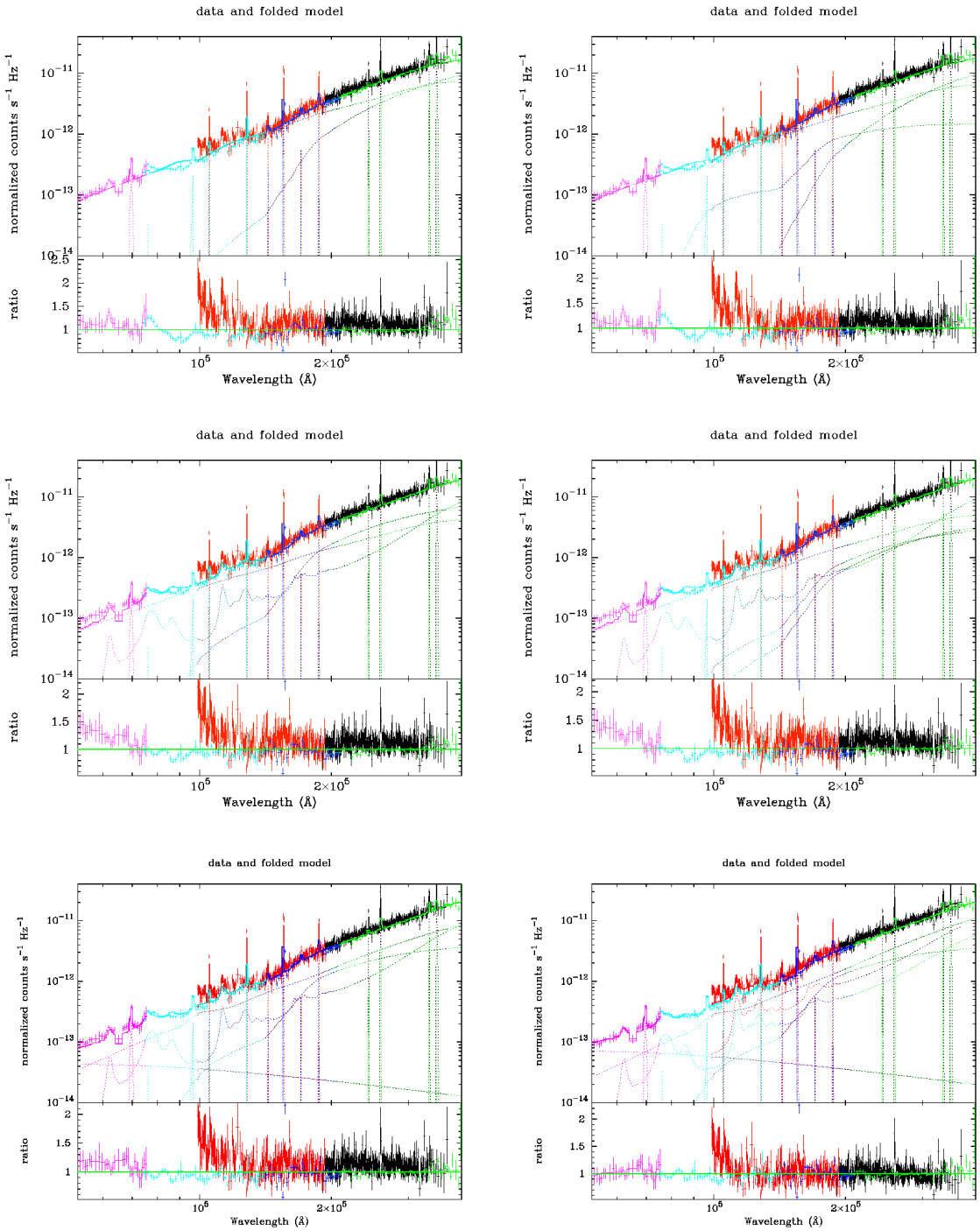

Figure 4.2: Attempts to model NGC 4395 as plotted by XSPEC. For clarity, data is binned so that total significance of each bin exceeds $5\,\sigma$ with a maximum of 10 datum per bin. The attempted models shown are a). Torus and NLR, b) Torus and two NLR, c) Torus, NLR, and host galaxy, d) Torus, two NLR, and host galaxy, e) Torus, NLR, host galaxy, blackbody, f) Torus, NLR, varying flux host galaxy, blackbody

light (Figure 4.1) and our extraction region may not handle extended emission accurately. The first of these issues leads to more host galaxy light in the larger slit low-resolution modules. The second issue occurs because our method of extracting the data in point-source mode inaccurately measures the extended host galaxy emission surrounding our point-like AGN emission. Point source emission is subject to slit light losses when measured, an affect that is implicitly accounted for in calibration. A spatially flat extended field of emission however will experience no slit light loss (losses and gains will be equal) so the implicit slit loss corrections must be removed. To correctly estimate the slit loss correction factor for our data, we would need to know, a priori, the galaxy light profile extending out from the AGN core emission. This factor would reduce the absolute flux of the extended emission by up to 10% according to the IRS Instrument Manual. Importantly, this factor would change both the host galaxy flux and the AGN flux (which should be unaffected by extended source corrections). Even if the slit loss correction could be estimated we would not want to use it. Using a pure point-source extraction will artificially increase the extended component of the flux for our low-resolution data (IRS Instrument Manual).

These extended emission problems should both artificially increase the low-resolution host galaxy flux. The data and corresponding models however both show that the measured high-resolution IR emission is more luminous than the low resolution data. In order to account for the flux difference between modules, we need to address AGN variability with our models.

We can determine what physical AGN elements specifically are varying by testing for best fit. The ability to free any fraction of parameters between models is built into XSPEC. We assume that the NLR region is resistant to AGN variability on the timescale between our observations (1 year) as the projected light travel time from the accretion disk is between 16 and 60 lightyears. Any temporal host galaxy dust variation will likely be negligible. We therefore assume the disk and surrounding obscuring region are the only possible time changeable components. Minezaki et al. (2006) confirm this by observing intraday IR variations indicative of toroidal origin.

We start by assuming the main contribution to variability in the clumpy N08 models is the accretion disk luminosity; evidenced by the dramatic variability observed from the UV to X-ray. We free this parameter between modules. Adjusting the bolometric luminosity scales the model with an implicit assumption that the inner and outer disk radii increase with luminosity (N08). We cannot however find a suitable fit with only this one free parameter. Initially, we test if we are capable of modeling the obscuring region by assuming only the inner disk radius changes with L_{bol}. This is accomplished by requiring the Y parameter to vary as the inverse square root of the luminosity change (which accounts for the dust sublimation defined inner torus radius variation, leaving the outer radius constant) and does not decrease the number of degrees of freedom of our model. This significantly worsens the fit statistic so is rejected as a possible model. We subsequently test the other model parameters $(\sigma, Y, q, \tau_v, N_0)$ independently freeing each parameter between the two models.

Although the fit statistic varies to a small degree ($\delta(\chi^2/\nu) = 0.06$), the best model is found with varying σ. As an additional criterion for quality of fit, we consider a model less robust if its derived inclination becomes pegged at the hard maximum or minimum (indicative that the model would be a better fit if given theoretically unlikely/impossible inclinations). We can also use the P_{esc} values derived from the models with worse fit statistics ($P_{esc} = 0.6 - 7\%$) to demonstrate that those models are unlikely. These two additional criteria corroborate our goodness-of-fit statistic to show that the parameter σ is physically most likely to be linked to the variability. Further testing with pairs of parameters changing reveals that although better fits can be achieved, the degree of improvement are minuscule and they come at the expense of feasibility according to our other criteria of a good fit. We find that changes in L_{bol} and σ fully explain the IR temporal variability.

We lastly try varying the hot blackbody model. M09 postulate that blackbody emission seen in other AGN represents hot graphitic dust within the silicate sublimation radius. We limit our model to a maximum temperature of $T = 1800K$, the carbon dust sublimation temperature. Our testing shows that because the blackbody emission peak lies outside our observed spectral range, our blackbody temperature cannot be finely constrained limiting our ability to test for variability.

NGC 4395 is unique in our sample as a result of variability and proximity. Our BAT AGN IRS observations are generally taken within minutes of each other meaning variability is not observed. NGC 4395 is the most spatially extended galaxy in our

sample due to it's small redshift, so slit light loss is negligible for almost all of our sample. Our standardized strategy for model fitting is based on the experience of modeling NGC 4395 (see Section 5.1).

4.5 Best Model Fits

We fit our data with the best-fitting combination of torus, NLR, and host galaxy models we can assemble. The torus model is parameterized by the disk angular thickness (σ), the torus outer radius scaled by the inner radius (Y), the average number of clouds through any equatorial ray (N_0), the power-law exponent of the radial density equation (q), the optical depth of the individual clouds (τ_v), and the inclination of the torus normal compared to the line-of-sight (i). The normalization scales with the bolometric luminosity of the AGN. The only NLR parameters are the ionization factor (U) and the normalization. The host galaxy model is described by the fraction of dust that is circumstellar (γ), the starlight intensity for the diffuse ISM dust (U_{min}), and the PAH mass fraction (q_{PAH}). The host galaxy normalization describes the dust mass observed through the slit aperture.

To isolate the continuum, the 13 prominent narrow emission lines in the IR spectra are modeled as Gaussians (Table 4.2). The low-resolution data suffers from subtraction of a strong off-target emission line resulting in the apparent absorption line at 6.47 μm. This is not a real feature, it can be seen as emission in the off-target spec-

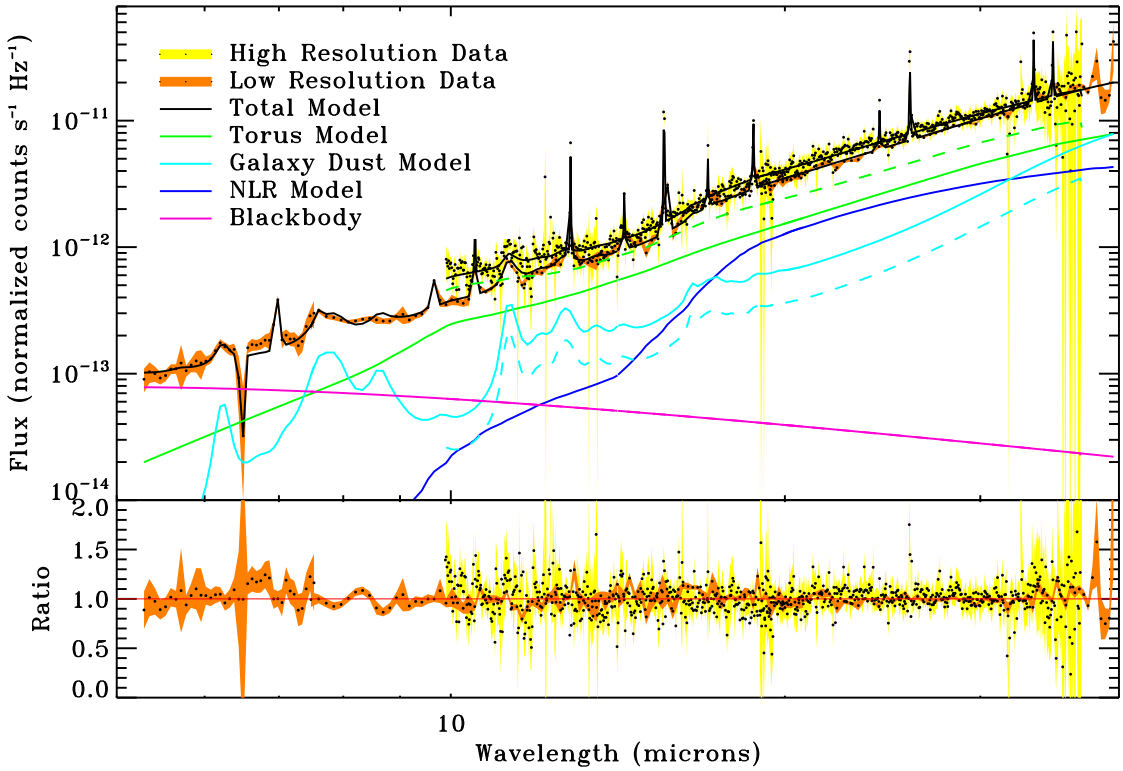

Figure 4.3: NGC 4395 *Spitzer* IRS data with cumulative model and components. Gaussian emission line not shown individually for clarity

trum as well as the photometric IRAC 8.0μm image. Following this, we fit our data with combinations of our continuum models in an attempt to minimize χ^2/ν. For both the high- and low-resolution data sets, we find that the combination of all four models results is the best fit despite the decrease in the number of degrees of freedom with each additional model. We show the data, models, and residuals in Figure 4.3 while model parameters are listed Table 4.1. The asterisks in Table 4.1 are indicative of parameter errors hitting the extreme of tested values beyond which we cannot extend our errors (see section 3.3.1). The high- and low-resolution models capture both the spatially varying host galaxy components as well as the time varying clumpy torus components. The IR spectrum contains the expected high-ionization emission lines due to the AGN, such as [O IV] 25.89 μm and [Ne V] 14.33 μm, 24.34 μm (Table 4.2). Typical AGN IR lines are observed similar to those in Weedman et al. (2005).

We find that our host galaxy model (Figure 4.3, light blue lines) corroborates the previously determined low metallicity of the nucleus of this galaxy (Kraemer et al., 1999) with a PAH mass fraction set at the lower hard limit. Our data is best fit with a starlight intensity distribution dominated by the delta function ($\gamma = 6.7^{+1.9}_{-2} \times 10^{-3}$) at $U_{min} = 1.48^{+0.04}_{-0.05}$ indicating dust almost entirely uniformly illuminated by low intensity stars. The normalization parameter varies between models as expected given

Table 4.1: NGC 4395 best-fit model parameters

Model	Parameter	High Res (June '08)	Low Res (June '07)
Clumpy Torus	$\sigma(deg)$	$41.5^{+6.6}_{-3.5}$	$55.0^{+17.5}_{-5.1}$
	Y	$100.0^{+0.00*}_{-10.2}$	
	N_0	$2.63^{+0.40}_{-0.50}$	
	q	$0.00^{+0.21}_{-0.00*}$	
	τ_ν	$50.5^{+7.2}_{-6.8}$	
	i (deg)	$41.9^{+14.7}_{-13.5}$	
	$F_{bol}(\frac{erg}{s \cdot cm^2})$	$1.28^{+0.09}_{-0.09} \times 10^{-11}$	$7.42^{+0.60}_{-0.41} \times 10^{-12}$
NLR	$\log U$	$-1.27^{+0.03}_{-0.04}$	
Host Galaxy	γ	$6.7^{+1.9}_{-2.0} \times 10^{-3}$	
	U_{min}	$1.48^{+0.04}_{-0.05}$	
	qPAH	$0.47^{+0.02}_{-0.00*}$	
	norm	$0.024^{+0.011}_{-0.007}$	$0.043^{+0.023}_{-0.003}$
Blackbody	Temp (K)	1800^{+0*}_{-353}	
	norm	$8.72^{+0.51}_{-0.51} \times 10^{-5}$	
Statistics	χ^2/ν	1.141	

Table 4.2: NGC 4395 emission lines

Wavelength (μm)	Identification	Flux (photons cm^{-2} s^{-1})
6.471	[Ni V]	-0.063 ± 0.046
6.707	[Cr II]	0.063 ± 0.028
6.964	[Fe IV]	0.131 ± 0.025
9.590	[Co II]	0.088 ± 0.015
10.508	[S IV]	0.093 ± 0.011
12.817	[Ne II]	0.217 ± 0.015
14.326	[Ne V]	0.068 ± 0.018
15.551	[Ne III]	0.390 ± 0.062
17.015	[Cr III]	0.096 ± 0.038
18.708	[S III]	0.252 ± 0.037
24.337	[Ne V]	0.142 ± 0.030
25.888	[O IV]	0.552 ± 0.039
33.504	[S III]	0.579 ± 0.131
34.817	[Si II]	0.494 ± 0.094

extended galactic emission. Despite the probability of having different populations of stars in the extended region, we model both data sets with the same renormalized curve to limit the number of free parameters. This does not dramatically affect the overall fit making it a worthwhile statistical trade.

The best fit torus model (Figure 4.3, green lines) gives an average number of clouds per equatorial ray $N_0 = 2.63^{+0.40}_{-0.50}$. Although low in the tested range of values ($N_0 = 1$ to 10), the very small filling factor required for clumpiness implies a huge number of clouds with a high best fit opacity ($\tau_v = 50.5^{+7.2}_{-6.8}$). Additionally, the N_0 value is larger than nearly 30% of the distribution of values found by M09. The model inclination is $41.9^{+14.7}_{-13.5}$ degrees. The torus angular width varies from $55.0^{+17.5}_{-5.1}$ to $41.5^{+6.6}_{-3.5}$ degrees while the bolometric luminosity adjusts from $0.742^{+0.060}_{-0.041} \times 10^{-11}$ to $1.28^{+0.09}_{-0.09} \times 10^{-11}\,\mathrm{erg\,s^{-1}\,cm^{-2}}$.

It is of note that neither of these parameters affects the total number of clouds, merely their distribution. The best fit radial power law has exponent $q = 0^{+0.21}_{-0.0}$ which implies a constant radial distribution. This impacts the anisotropy of the model but does not have a substantial impact on the SED shape (M09). Our model is of course limited to a finite outer disk with best-fit $R_o = 100^{+0.0}_{-10.2} \times R_i$ but this value is at the hard maximum. N08 admit that due to ambiguity between models, the clumpy torus size cannot be well constrained by SED analysis. We therefore do not experiment with Y values greatly exceeding what has previously been observed.

We use the NLR model (Figure 4.3, dark blue line) to confirm our presumption

that all of the NLR light is captured by the high- and low-resolution apertures. We check this by fitting the high- and low-resolution data with separate NLR models and confirm that the best fits are nearly identical. We then attempted to fit both datasets with a pair of geometrically different NLR models. The ionization parameter U and normalization (giving different covering factors) are allowed to vary implying stratified NLRs at different radii to account for the two structures seen by Matthews et al. (1999). Although a decent fit was possible, the statistical improvement is negligible. The single NLR approach assumes the NLR is dominated by emissive material subjected to an identical ionization field, or rather all the material is at the same distance to our predicted ionizing spectrum.

We derive the NLR radius from the ionization parameter ($\log U = -1.27^{+0.03}_{-0.04}$) and find $R_{NLR} = 0.72^{+0.03}_{-0.02}$ pc. This value is significantly below the resolved NLR of Matthews et al. (1999) (4.8 and 19.4 pc) and therefore possible. It remains reasonable when compared to prior photoionization work by Kraemer et al. (1999) which predicts an NLR subjected to ionization parameter $\log U = -1.7$. The low luminosity of NGC 4395 limits our NLR models to a radius between 0.05 to 23.5 pc; but the continuum emission of the more distant NLR are several orders of magnitude below our detected continuum. We can put a lower limit on the radius of an additional NLR ($\log U < -2.92$ yielding $R > 4.8$ parsec) but statistically the model does not improve with its inclusion.

4.6 Validity of our models

4.6.1 Theoretical underpinning

Although selected for its proximity, prior observations, and uniquely low luminosity; we need to ascertain whether or not our models are appropriate for this test case. Namely, we need to assure ourselves that generalized thin disk accretion models are applicable and that NGC 4395 is not a member of a different class of objects with accretion processes substantially different from typical AGN. One reassuring extrapolation may be made using the Kaspi et al. (2000) M-L relationship. Using their empirically fit AGN mass-luminosity trend (equation 11) and the observed $\lambda L_\lambda(5100\text{Å}) = 5.9 \times 10^{39}$ erg s^{-1} (Peterson et al., 2005), one can extrapolate an Eddington ratio of 1.0×10^{-3}. This value is of the same order of magnitude as our ratio of 7.2×10^{-3} which is substantial given the incredible variability seen in our SED and the inherent errors of the original fit. This suggests that the same process powers classical type 1 AGN across three orders of magnitude in mass.

First we examine the applicability of the toroidal dust model for this low luminosity AGN. If we presume that the broad-line region and toroidal obscuration region (BLR/TOR) are both a clumpy wind driven outflows from the accretion disk (Emmering et al., 1992), we can assume that the presence of the one (Kraemer et al., 1999) directly implies the presence of the other. Furthermore, we note that NGC 4395 lies well above the M-L cutoff for torus existence determined by Elitzur & Ho

(2009). The argument they posit is that a weakly accreting disk will be incapable of producing a steady state mass outflow (BLR/TOR). Therefore a region of observed low luminosity type 1 AGN on the mass-luminosity plane can define a condition for TOR existence. Our AGNs position on the M-L plane along with the cutoffs theoretical underpinning (Elitzur & Ho, 2009) allow us to derive a maximum radiative efficiency for our object of $\eta \leq 0.05$. This implies NGC 4395 is not necessarily within the domain of radiatively inefficient or advection dominated accretion flow.

If we assume normal thin disk accretion, we can use the empirical fit of mass, bolometric, and optical luminosity to the detailed relativistic disk models of Davis & Laor (2011) to estimate the accretion rate and radiative efficiency of NGC 4395. Using a galactic extinction corrected optical Palomar spectra (Filippenko et al., 1993), we extrapolate down to our mass and luminosity to give estimate $\eta = 0.44$, a value which is unphysical given the outflow argument. Presuming the optical luminosity is actually six times brighter, supported by the bolometric luminosity, we get a much more realistic value of $\eta = 0.030$. Although this value represents an extrapolation an order of magnitude lower in mass than actually modeled by Davis & Laor (2011), it confirms that the presumption of thin disk accretion is quite reasonable for NGC 4395.

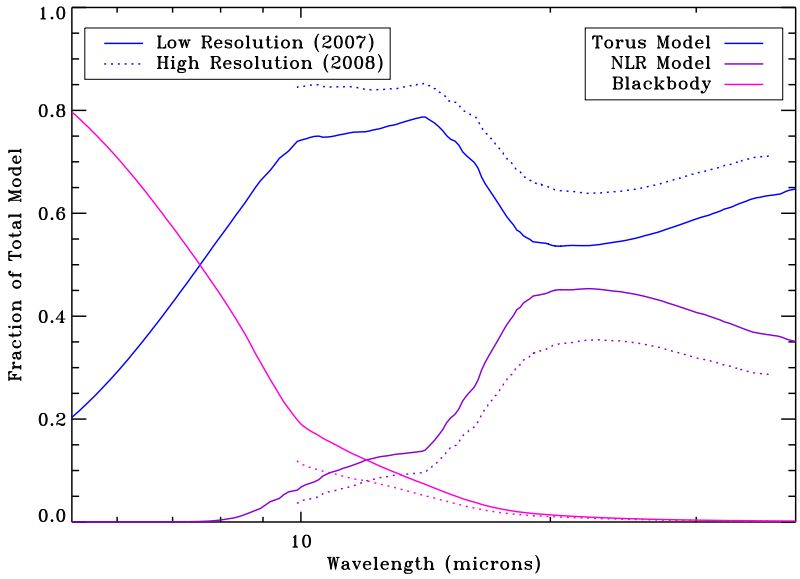

Figure 4.4: NGC 4395 fractional contribution of model components to total model; emission lines and host galaxy model omitted for clarity.

4.6.2 Model fit analysis

We plot the fractional contribution of each model component compared to the total model as a function of wavelength (Figure 4.4). The clumpy torus model is responsible for 58% and 43% of the emission for the high and low-resolution fluxes (different flux states) respectively. This is in contrast to the 25-28% contribution for the NLR model, 13-25% for the host galaxy model, and 0.8% for the blackbody model. This flux breakdown highlights the dominance of the clumpy model to our analysis while demonstrating that all of our models have substantial flux contributions at different wavelengths. For instance, below 9.8μm, the blackbody is responsible for 34% of the flux. Additionally, the host galaxy model is visibly important because of the dominant broad PAH features (Figure 4.3), despite its relatively low overall

flux contribution. This reassures us that the total model does not contain spurious components contributing statistically but not qualitatively to our fit.

The variability of the two data sets is clear, especially when the data are binned identically (Figure 4.5). We have been able to improve upon our understanding of this variability by isolating the AGN variability from the host galaxy and NLR emission with our models. This gives a shift of 3.11×10^{-12} to 4.82×10^{-12})erg s^{-1} cm^{-2} (between 9.86μm and 37.13μm). Isolating the AGN emission changes the degree of variability from a 12% increase, not accounting for slit size, to a 35% absolute increase in AGN IR flux. Additionally, our best-fit clumpy models suggest a bolometric flux change of $7.42^{+0.60}_{-0.41} \times 10^{-12}$ to $1.28^{+0.09}_{-0.09} \times 10^{-11}$ erg s^{-1} cm^{-2}, or a 42% increase.

4.7 Observed NGC 4395 Variability

In order to explain the context of our AGN IR variability we delve into the hard X-ray data collected by the *Swift* BAT. Figure 4.6 shows the hard X-ray variability of NGC 4395 and the fortuitous timing of our two IR observations capturing both low and high emission epochs. Data is binned into two month bins and the six months prior to each *Spitzer* observation are shown. Our low-resolution data were taken during a period of low hard X-ray luminosity (0.95σ below the weighted average) and our subsequent high-resolution data were taken during a period of very high luminosity (3.41σ above). These two observations mirror our flux increase in the IR.

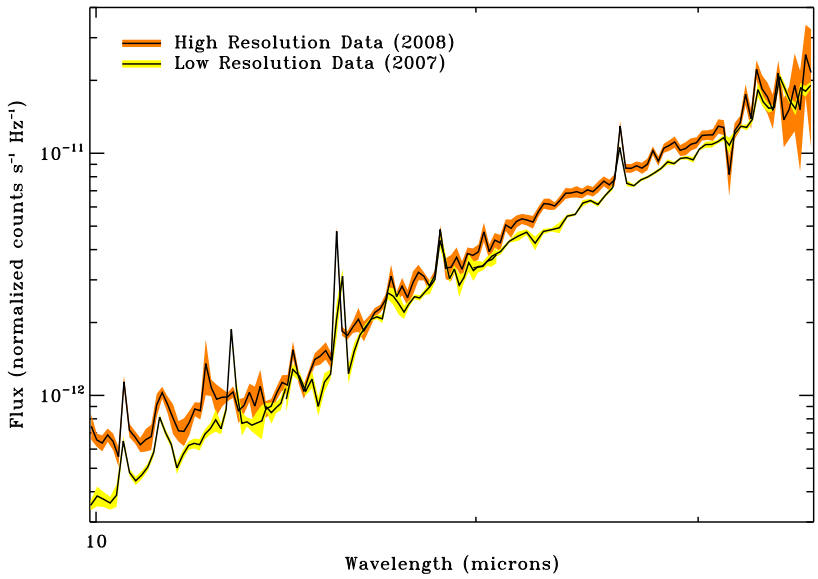

Figure 4.5: NGC 4395 high- and low-resolution data binned identically in overlap region to demonstrate flux disparity.

In addition to the time of observation flux disparity, the six months prior to the high luminosity observation are 1.5 times more luminous than the six months before the low-resolution observation. Although this confounds the issue of the IR response time to the hard X-ray rate increase, its consistency simplifies the general analysis.

In addition to similar flux shifts, the observed spectral index of the two data sets are close, despite differing in energy by almost five orders of magnitude. The IR model for the AGN emission (clumpy torus and blackbody) can be replaced with a single power law ($\chi^2/\nu = 1.50$) with a photon index of 2.50 ± 0.04. The hard X-ray photon index of $1.99^{+0.31}_{-0.29}$ ($\chi^2/\nu = 1.19$) and the photon index of the power law connecting the data sets (1.87) strongly correlate and suggest similar origin to the IR emission (with the slightly steeper IR curve explained by reprocessing).

Based on the simultaneous increase in IR and hard X-ray emission, we conclude that obscuring dust is not driving the variability we observe in NGC 4395. Whereas cool absorbers can be used to explain soft X-ray variability (Nardini & Risaliti, 2011), neither the IR response nor the hard X-ray power-law spectrum of NGC 4395 points towards obscuration. Instead, we conclude that the disk/corona system drives both energy regimes of variability. The best fit IR model suggests that the toroidal obscuring region flattens (σ decreases), without affecting the overall number of clouds, in response to an increase in disk luminosity. We hypothesize this is due to an increased radiation pressure driven outflow oriented parallel to the disk. This is corroborated by the radial cloud density power law and outer disk radius best fit by the hard lower and upper limits respectively ($q = 0^{+0.21}_{-0.0*}, Y = 100^{+0.0*}_{-10.2}$). Our model represents the largest disk we allow with a maximum number of clouds at the outer radius. Both these values were relatively insensitive to changes in other aspects of the model. We do not think that the outer region of our obscuration region has a hard cutoff as modeled; instead we believe the IR emission manifests the behavior of cloud outflow from the disk as best it can.

Clumpy, dusty outflows have been previously observed through H_2O masers in several objects, including Circinus (Greenhill et al., 2003). These masers denote X-ray illuminated dusty clumps occupying the observed ionization cone and possibly tracing the edges of the clumpy obscuration region (Tristram et al., 2007, their Figure 9). They likely feed the toroidal obscuration region. Although variability of

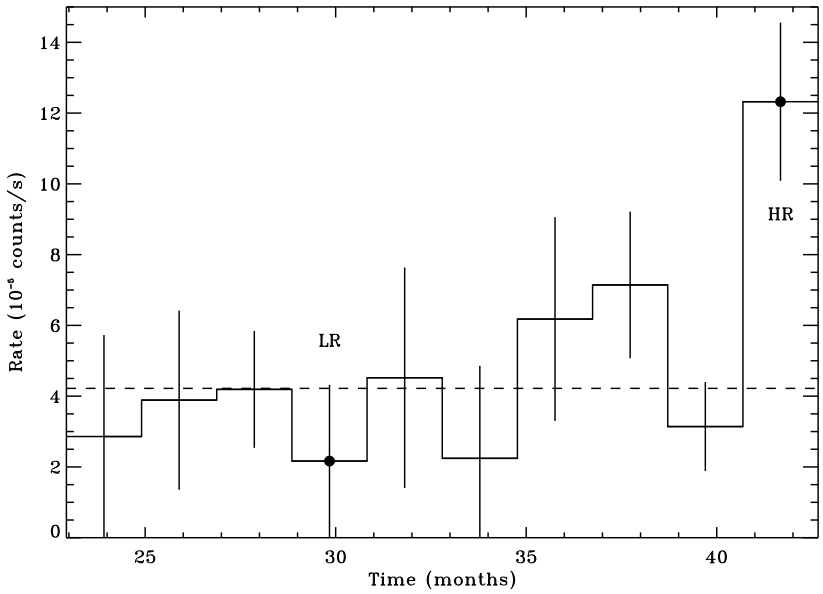

Figure 4.6: *Swift* BAT 14-195 keV light curve for NGC 4395. Data is plotted with two month bins. Circles indicate times of the high and low resolution *Spitzer* observations. The flux averaged over the entire observation is plotted with a dashed line.

the maser field is not analyzed, the masers placement suggest that a large shift in AGN luminosity could exert radially directed radiation pressure thinning the toroidal obscuring region.

4.8 NGC 4395 Conclusions

Our analysis reveals through spectral modeling that the IR emission of NGC 4395 is both variable and well modeled using existing theoretical models. The host galaxy model captures the PAH emission features well despite intermodule differences due to extended emission and non-empty subtraction regions. The point-like AGN light is unaffected by these problems and is substantially more robust. The IR emission

is dominated by AGN light (71-84% of total IR flux) and our models represent a significant improvement in fit over a simple power law model ($\chi^2/\nu = 1.14$ vs. 1.50). The non-host galaxy light is clearly variable and our models are capable of accounting for both shifts in flux and spectral shape.

Extensive parameter testing indicates that the data is best fit by a variable clumpy torus model in which the AGN bolometric luminosity increases while the cloud distribution flattens. The luminosity increase is also seen with concurrent hard X-ray observations suggesting that this variability is intrinsic to the AGN and not an obscuration effect. We conclude that the flattening equatorial obscuring region is the result of increased outwardly directed radiation pressure driving a substantial cloud outflow. This is supported by a the remaining cloud distribution parameters which are best fit with a uniform density of clouds at the maximum allowable distance from the AGN.

While demonstrating the effectiveness of our models at fitting and describing this unique object in our sample, several important notes must be made. Firstly, the clumpy torus model dominates our NGC 4395 emission. This AGN serves as a middle of the road object with a notable (statistically significant) host galaxy contribution, yet is dominated by smoother toroidal emission. This is encouraging because it implies that fits should be possible with objects both host galaxy or AGN dominated. Secondly, our modeling software is capable of adjusting for significant model complications. The ability to account easily for variable IR emission as well as imperfect

background subtraction demonstrates the inherent strengths of our methodology and code. Finally, we must consider the fitting statistics of our software. Although capable of finding the best possible fit for our data, χ^2/ν did not change dramatically between models. This is partially because of the faintness of NGC 4395 and inherent large errors on much of our data. The smooth continuum also makes it more difficult to find a definitive model solution. There is no escaping that many good fits exist. Our BAT AGN sample as a whole, however, contains many more peculiar data sets with discerning features, smaller errors, and a large variety of continuum shapes. This is where our models and methodology excel.

Chapter 5

Sample Analysis

In this chapter, I present the analysis applied to the full sample. The model fitting techniques here are the same as those used in Chapter 4. I describe the distribution of models used as well as the best-fit parameter distributions for each model component.

5.1 Model Components

We fit the 66 AGN of our sample with the combination of models taken from the discussion in Chapter 3 and the work presented in Chapter 4 that most accurately matches our data. The model parameters are given in Table 5.1 and 5.2, and Figure 5.9 contains the data and best-fit models for every object of our sample. Our sample demonstrates great variety in spectral shapes, all of which can be accounted with our baseline set of physically motivated models.

Most of our AGN classifications are taken from NED. Where multiple classes are given, or the origin of the classification is unknown, we use cited references or available optical spectra to make our own classifications. Several of the Tueller et al. (2010) classifications are updated to reflect our optical spectra analysis and literature review. Details regarding this process, and the references for the individual AGN can be found in Section 6.1. Frequently, we use the Veron-Cetty & Veron (2010) catalog to find literature with classifications that we cite directly. Our optical classifications are based on SDSS (Ahn et al., 2012) and 6DF Galaxy Survey (Jones et al., 2009, 2004, 6df) optical spectra. For the Sy 1 subclass assignments, we use the Winkler (1992) Hβ/[O III]λ5007 line ratio criteria. To distinguish between Seyferts, HII galaxies, and LINERs, we use the same line ratio diagnostics as Winter et al. (2010, hereafter W10). These include the theoretical HII galaxy-AGN diagnostic of Kewley et al. (2001), the empirical HII galaxy-composite galaxy diagnostic of (Kauffmann et al., 2003), and the Seyfert-LINER empirical division of Kewley et al. (2006). Our classification strategy is similar to Tueller et al. (2008, 2010). We update several classifications taken from the 22-month BAT AGN catalog (Tueller et al., 2010) where we find compelling evidence that the type has been mislabeled.

We use optical images from NED to identify the morphology and orientation of the AGN host galaxies. A representative image of each AGN and it's host is shown in Figure 5.5.

Under the assumption that all AGN contain tori and that the IR spectra of these

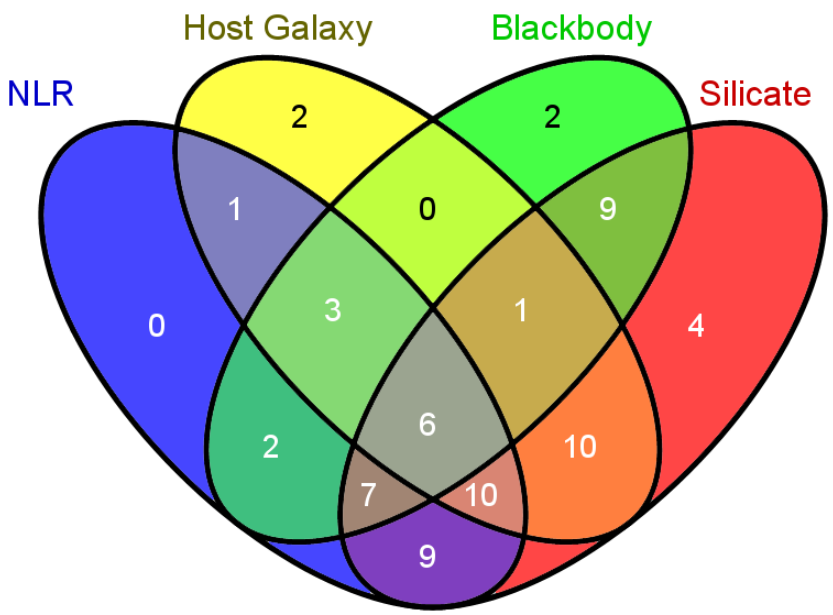

Figure 5.1: Venn diagram of model combination frequency, all models also include the clumpy torus model.

BAT AGN are dominated by their AGN (as suggested by analysis of their emission line ratios – Weaver et al., 2010), we use the torus model in all cases. With the inclusion of up to four optional models (NLR, host galaxy, blackbody, silicon absorption), we have 16 possible model combinations (Figure 5.1). Because we have a large number of models and an extensive parameter space, we cannot uniformly test all possible models. This necessitates a standardized procedure for the inclusion of additional models that slowly adds complexity (Section 4.4). We begin every model fitting using the clumpy torus model and the NLR model. If obvious PAH features are present we also include a host galaxy model.

After fitting extensively, we then add a silicate extinction curve to the model and

find 56 of our 66 objects (85%) have a statistically significantly better fit. Brandl et al. (2006) find 82% of their starburst spectra models are improved with the use of silicate absorption models supporting the idea that inactive galaxies also frequently demonstrate silicate absorption. Given the great impact of adding this extinction curve, the lack of attention paid to this component in previous attempts to model AGN continuum (Section 3.4) is clearly a substantial oversight. We experiment with each of three extinction curves for every model (Section 3.3.5). The best fit absorption curve type and silicate optical depths will be discussed in Section 5.3.2. At this stage we removed model components if their total flux was low enough to have no statistical impact on the total model. Delaying removal until this stage insures that NLR and host galaxy models that are heavily obscured by galactic dust at 9.7 and 18 μm can still be incorporated. It is also of note that the silicate extinction curves are applied identically to all model components. The single absorption curve comes from the implicit assumption that this obscuration is not intrinsic to the AGN, rather it originates in the either the host galaxy or Milky Way ISM.

Where the model still fails to fit the data, we add a blackbody component as was needed in Chapter 4 for NGC 4395. Blackbody models are frequently used in the literature (S08, M09). The blackbody is limited to temperatures between 100K and 1800K. We set the upper limit with the maximum possible grain sublimation temperature given our grain mixture. The lower limit is set because we only want to consider warm torus dust, not the cool ($T = 35 - 65$K) reprocessed stellar emission

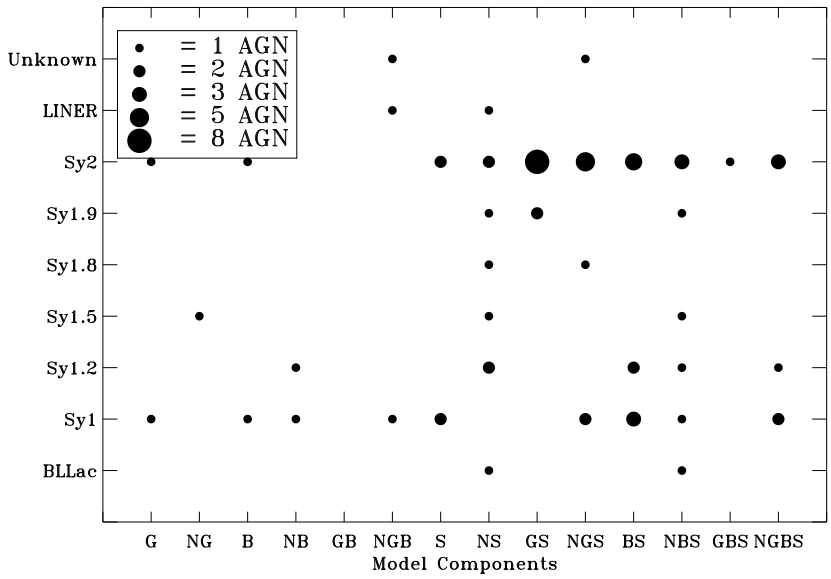

Figure 5.2: A two dimensional histogram of model components of the best-fit model versus AGN type. The area of the circle used denotes how many AGN have a given type and model combination.

(S08) which should be captured by our variable host galaxy model. Tests of our host galaxy dust model show that a wide variation is possible in the low wavelength end of our models, representative of differing quantities of low temperature gas. This variation is controlled by the U_{min} parameter, which sets the strength of the ionization parameter at the location of the diffuse ISM dust. The majority of the time the blackbody component is used, the model fit pegs at the high temperature limit. This is likely because above 557K our data are incapable of observing the blackbody peak and can only poorly constrain the temperature.

We plot the model components required for each galaxy used against the AGN type of each galaxy in Figure 5.2. The trend to favor models that include silicate

absorption is apparent, with a slightly stronger tendency for obscured Seyferts to be absorbed than unabsorbed. In the results section we will discuss whether this trend is a result of attributing AGN absorption to the galactic dust absorption, or instead if non-AGN obscuring material is affecting AGN classification. Figure 5.2 also shows that no AGN type is dominated by a single model combination.

5.2 A Comparison of Fit Statistics

Although our fits are qualitatively impressive given the narrow parameter space allowed for each model, the distribution of χ^2/ν values is large (Figure 5.4a). Other authors add artificial errors or weighting to enhance fit statistics (i.e. the 10% error added by M09, Section 3.4) and in the process redefine χ^2. In order to compare with the literature, we calculate an adjusted fit statistic (χ^2_{M09}/ν) for our sample using an artificial 10% error and plot it with the actual χ^2/ν distribution (Figure 5.4a). The χ^2_{M09}/ν values for our sample have a mean of 0.63 which implies we have overestimated error, similar to the M09 sample (mean $\chi^2_{M09}/\nu = 0.27$). Their fit statistics are lower because they smooth their data, omit host galaxy uncertainties, and only model Type 1 AGN. In the end, using the standard fit statistic produces better models because inconsistent fluxes and data with large systematic errors are taken into account by the fitting algorithm as originally intended.

Six of our models with the largest χ^2/ν values fit spectra with very small flux

errors (mean error $< 1.6\%$ of flux) compared to the rest of the sample (mean error $=$ 5.8% of flux). NGC 7582 highlights the flux bias of our fit statistic with $\chi^2/\nu = 82.89$ (our worst statistical fit), the largest measured IR flux, and a mean displacement of the data from the model of 7.8%. We show in Figure 5.3 that the total χ^2 value is dominated by small flux deviations from the low-resolution PAH spectral features. The model however shows strong adherence to the complicated spectrum. These models have qualitatively good fits, but because of their high flux, deviations from the data are considerably larger than the flux errors. When we plot the IR flux against our χ^2/ν values (Figure 5.4b), a clear flux bias of our fit statistic is apparent. The correlation highlights that although χ^2/ν is adept at accurately determining the best possible model for a given spectra, it is not an objective fit statistic to compare between models in our sample. Our AGN continuum modeling improves upon both the methodology and model quality of the latest work in the field (Section 3.4), however the physics of our models is still not adequate to exactly match the high quality of our data. We realize that in order to work at the front of this burgeoning field, we have to settle for imperfect continuum models. Several authors have come to similar conclusions (S08, M09, M12) and have redefined the fit statistics. We choose to continue using the established means of fitting while acknowledging that individual models are limited in the constraints they can place AGN characteristics. Our spectral fitting software requires a $\chi^2/\nu < 2$ in order to compute errors (Section 3.3.1). Instead we focus on the ensemble properties of our AGN model parameters.

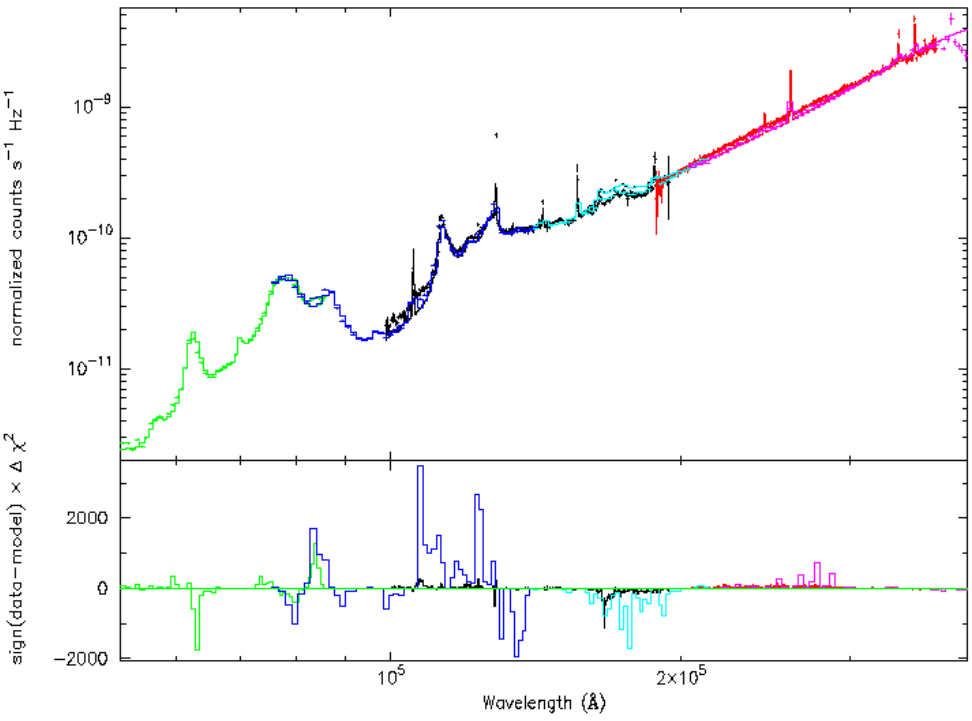

Figure 5.3: Demonstration of large χ^2/ν value for NGC 7582. The top figure shows the spectrum with errors and the cumulative model. The bottom panel shows the contribution to the χ^2 statistic for each data point. Models and data are color coded by module: SH = black, LH = red, SL2 = green, SL1 = dark blue, LL2 = light blue, LL1 = magenta.

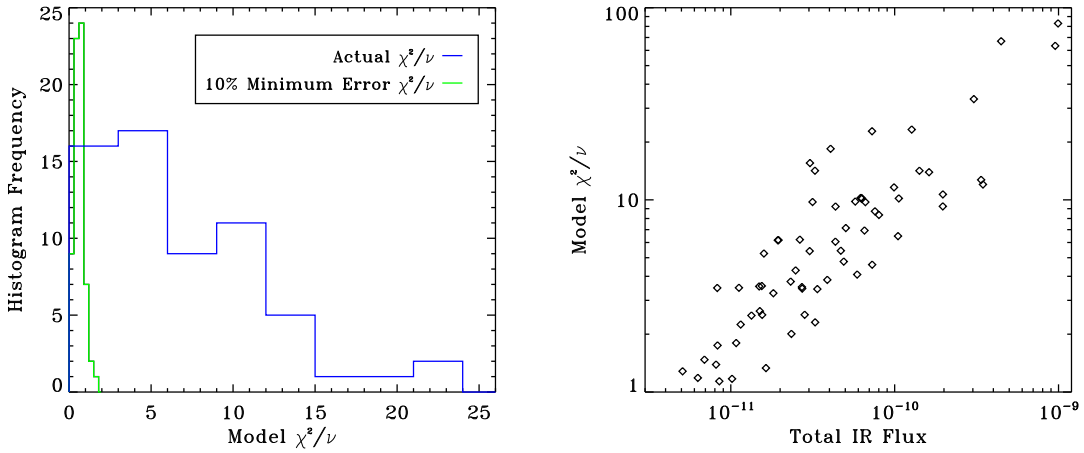

Figure 5.4: Model fit statistics plots: (left to right) a.) Histogram of both true χ^2/ν values and χ^2/ν values assuming minimum 10% error for every flux bin (see text, M09). Six high χ^2/ν values omitted. b.) Plot of total IR flux versus model fit statistic, χ^2/ν.

5.3 Parameter Distributions

5.3.1 Clumpy Torus Model Parameter Distributions

In this section we analyze the distribution of best-fit parameters for our entire sample to examine the physics of the galaxy nuclei. In our histograms, we bin the model parameters at or above the multidimensional input model parameter resolution. The clumpy torus model component is used in all cases with a combination of other models and histograms of the distribution of best-fit parameters are shown in Figure 5.5.

For the torus model, the Gaussian width of the cloud distribution about the disk

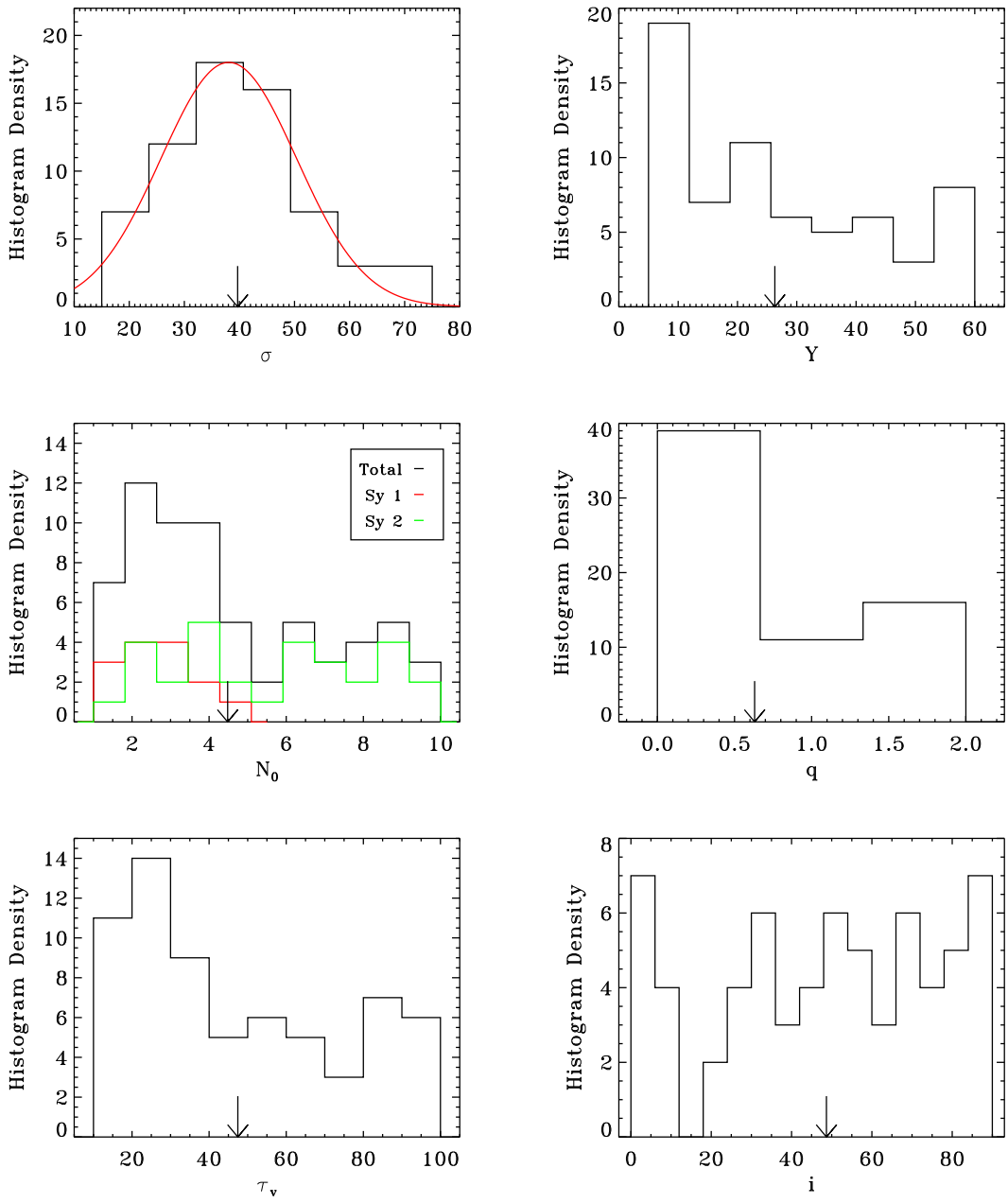

Figure 5.5: Distribution of parameters for clumpy torus model used in fitting all data sets. See figure 3.5 and Section 3.3.3 for parameter definitions. Large arrows denote parameter averages.

plane is the parameter that most directly affects disk thickness and the shape of the clumpy medium. The distribution of σ values appears normal with a best-fit peak at 39.6°. Previous efforts using a clumpy torus model on a sample of type 1 AGN yielded a mean σ of 34° (M09). We consider whether an excess of thicker disks occurs with the inclusion of obscured AGN. We perform a two-sample Kolmogorov-Smirnov test (K-S test) on the σ parameter for the Sy 1 and Sy 2s of our sample. A K-S test is a nonparametric statistical test to determine if two parameter distributions are drawn from the same population. The probability that σ is drawn from the same population for these two samples is 82%, supporting unification. Correlations between σ and other parameters will be explored in Chapter 6.

The Y parameter distribution is consistent with prior observations (M09) despite its small affect on model curvature. The Y parameter is a stand in for the outer radius of the obscuring torus as the inner radius is set by the bolometric luminosity of each AGN. The distribution peaks at the low end with a relatively flat distribution out to the upper extreme that was tested. The mean of Y values found is 27.4. The impact of this parameter on the model curvature is noted to be small (N08), especially when the radial density parameter (q) is large yielding a poorly defined edge. N08 postulate that nothing in currently available IR data implies a torus radial thickness larger than $\sim 20 - 30$. We include larger parameter values but realize that their significance is small given their small effect on spectral shape.

We find the distribution of the equatorial number of clouds (N_0) in the torus

is relatively flat with a small peak around three. M09 observe a similar uniform distribution with a peak at two. Interestingly, all of our Sy 1s have N_0 values under five, whereas the Sy 2s have a flatter distribution spanning the entire parameter range. We discuss this dichotomy in Section 6.4.1 and deduce that the Type 1 AGN densities are being underestimated by our models because it is difficult to distinguish between the high- and low-density face-on spectral models. We show this has little impact on other elements of the model.

Our q distribution is relatively flat with a tendency towards low values ($\bar{q} = 0.630$) implying the emission is less isotropic. Instead of a gradual decrease in cloud density that we might expect for an outflow, low q values imply a sharp radial cutoff for many of our objects. Given the unknown nature of cloud suspension outside of the accretion disk, especially at the outer edge of the torus, we cannot discount this possibility.

The optical depth parameter distribution (τ_v) is between the values found by M09 and M12. N08 discuss the complicated nature of this parameter in a clumpy medium and express the difficulty of isolating its impact from that of the other parameters. Given that any $\tau_v > 10$ implies high mid-IR optical depth, it is not surprising that we are relatively insensitive to it's exact value and show a broad distribution.

The distribution of inclinations is relatively flat with an average inclination (i) of 49°. Although a perfect model and an unbiased sample would yield a completely flat distribution, we are comforted that a K-S test of the data yields an 83% likelihood that our data are drawn from a uniform distribution. The relationship between the

model inclination found and the known AGN type will be studied in Section 6.2.

5.3.2 Best-fit Parameters of Additional Model Components

We find the use of the NLR model improves the fit of 58% of our AGN. We assume the AGN best fit without NLR components contain NLR but they are too faint to be distinguished from the other IR components. Bright host galaxy emission, small NLR covering factors, or large NLR distances could all make the NLR continuum flux to weak to observe. The inclusion of the NLR model appears independent of AGN type, a fact which validates our models and unification. The parameterization of the NLR shape is limited to only the dimensionless ionization parameter ($\log(U)$). Its distribution is centered on the mean value, $\log(U) = -0.37$, with broad asymmetric wings yielding a negatively skewed distribution. The NLR luminosity scales with both AGN luminosity, ionization parameter, and the covering factor. In the next chapter, we will examine the geometric ramifications of the NLR parameter.

The host galaxy models span a large parameter space and provide a substantial contribution to the IR spectral models, especially in type 2 AGN (Figure 5.7). Our host galaxy dust model is dominated by diffuse dust ($1-\bar{\gamma} = 96.2\%$) represented by a delta function at U_{min} in our starlight intensity distribution. This is remarkably close to the average found by DL07, albeit in a sample of five, of 96.14%. Our best-fit U_{min}

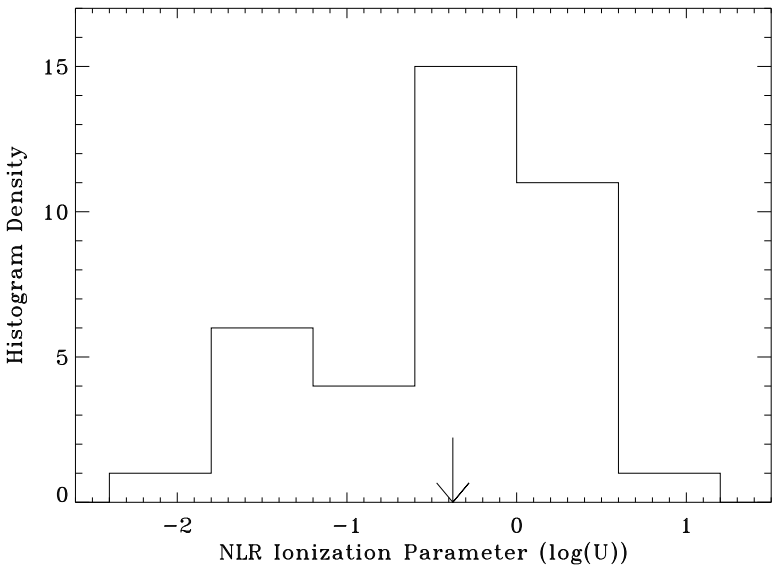

Figure 5.6: NLR ionization parameter distribution, large arrow denotes parameter average

values locating that delta function covers the parameter range allowed and has an average roughly double that of DL07 sample (10.6 vs 4.9). We consider this reasonable given the apertures of our spectra are focused on the galactic nuclei compared to the DL07 observations which encapsulate the entire galaxy. It is presumed that nuclear dust is exposed to a stronger radiation field than the extended galaxy dust. We find our distribution of PAH fractions (q_{PAH}) is split into high and low groups divided at the mean (2.53). Analysis of these groups reveals no AGN type bias, but correlations with other parameters will be explored in the Section 6.4. Because the small extraction regions omits the majority of the host galaxy for our sample, we plot its normalization in terms of the fraction of total IR light within our spectra (f_{host}). This is substantially more informative than the usual parameterization, which can

be reduced to the mass of dust observed within the aperture. The host galaxy flux fraction ranges from 5-80%. The lower limit demonstrates the minimum detectable host galaxy contribution (all AGN should exhibit some host galaxy IR flux) whereas the upper limit shows the smallest fractional IR AGN contribution within our sample. Individual AGN attributes will be discussed in the analysis. We find that 60% of Sy 2s are best fit with a host galaxy component compared to only 43% of Sy 1s. Obscured AGN are more likely to have a stronger host galaxy contribution to their spectrum, which implies that the AGN light is blocked, even in the IR.

Most (85%) of our models are improved with a multiplicative silicate absorption component. Local and host galaxy reddening is likely for all of our AGN so we are comfortable with this percentage, but we lack comparative statistics as most authors omit details surrounding ISM silicate absorption. The average optical depth at 9.7 μm ($\tau_{9.7\,\mu m}$) is 0.66 with a similar representation of all three absorption models attempted (Figure 5.8. This is in contrast to other authors who find a clear favorite (reference).

Thirty of our best-fit models were dramatically improved with the inclusion of a blackbody component. A low wavelength IR excess is visibly clear in many of our models without this addition. Despite the large allowed temperature range, 30 of the blackbodies had the best statistical fit with a temperature at the upper limit, 1800 K. It is theoretically unlikely that so much dust has a temperature so close to its sublimation temperature so we conclude that our spectral range lacks the short wavelength data to accurately assign a temperature for this component. Our shortest

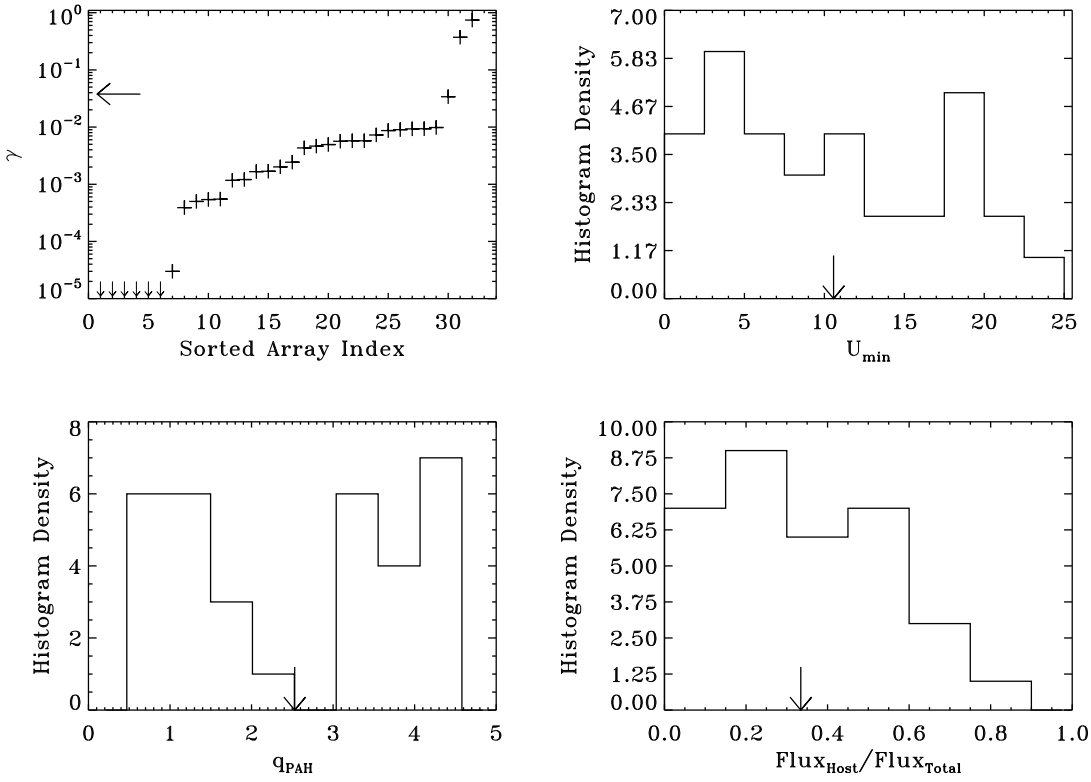

Figure 5.7: Host galaxy parameter distributions, large arrows denote parameter averages. For clarity, γ parameters are sorted and plotted directly with small arrows indicating $\gamma = 0$. Host galaxy normalization is expressed as a fraction of the total modeled IR flux.

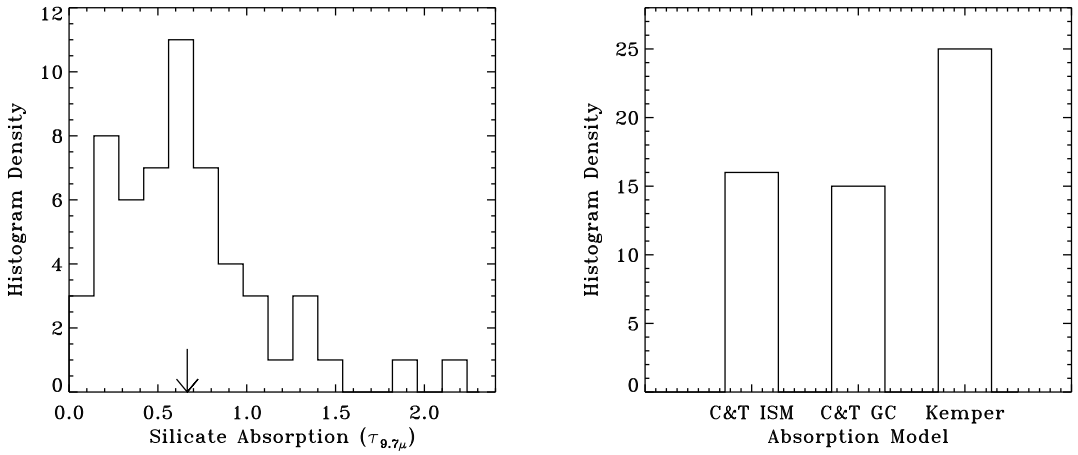

Figure 5.8: Silicate absorption parameter distributions, large arrows denote parameter averages.

wavelength data ($\sim 5\,\mu$m) does not capture the peak of the blackbody at temperatures higher than 580K. Fortunately, our blackbody component only contains, on average, around 16% of the total IR flux. We will discuss the possible location and explanations for this component in the next chapter.

Table 5.1: Best-fit clumpy torus model parameters

Name	χ^2/ν	σ	Y	N	q	τ	i
2MASX J05580206-3820043	9.25	41.67	11.79	4.21	1.38	47.58	11.83
2MASX J09043699+5536025	1.39	29.39	35.38	1.37	1.71	25.43	44.06
2MASX J09112999+4528060	3.55	40.08	20.04	3.87	1.86	84.48	75.94
2MASX J19595975+6508547	1.75	53.77	5.71	1.19	2.00	37.38	40.06
ARK 120	6.52	38.41	21.03	2.77	0.35	27.63	11.63
ARK 347	6.06	70.37	29.16	1.98	0.44	52.16	35.06
CGCG 041-020	4.3	42.15	39.75	4.57	1.02	29.51	66.16
CGCG 118-036	5.44	52.28	7.71	5.83	0.00	15.17	28.96
CGCG 420-015	23.23	51.06	27.34	3.67	1.02	36.61	24.64
ESO 005-G004	11.62	55.7	19.52	8.48	0.00	51.56	0.00
ESO 121-IG028	1.47	15.61	22.66	6.79	0.86	73.68	66.55
ESO 140-G043	10.69	45.02	52.02	3.79	0.32	34.13	0.00
ESO 141-G055	8.27	53.92	46.85	4.64	1.47	14.31	13.25
ESO 157-G023	5.26	43.3	10.33	2.98	0.97	94.44	79.9
ESO 198-024	2.52	29.33	15.5	2.73	0.00	33.42	53.84
ESO 297-G018	2.52	25.98	19.65	2.50	1.00	68.4	56.5
ESO 323-077	33.48	42.08	40.34	5.25	1.34	28.18	37.8
ESO 374-G044	18.45	44.82	10.01	6.58	0.75	83.14	72.57
ESO 417-G006	1.8	36.84	60.00	2.59	0.00	31.63	79.85
ESO 426-G002	3.83	40.44	25.64	3.78	0.29	66.21	32.06
ESO 506-G027	4.6	39.21	29.77	7.80	1.37	24.27	42.27
ESO 511-G030	6.21	40.12	39.42	1.43	0.00	12.12	67.24
ESO 548-G081	9.81	30.37	14.67	3.11	1.01	43.45	11.29
ESO 549-G049	22.78	70.00	5.00	2.73	2.00	10.00	58.24
IC 1816	10.13	64.1	10.83	8.85	1.71	100	90.00
IRAS 05218-1212	10.25	50.51	11.14	2.92	0.00	75.20	32.95
LEDA 088639	5.42	28.19	10.00	2.63	0.00	52.93	70.52
LEDA 089420	3.27	39.34	33.35	3.25	2.00	24.02	90.00
LEDA 178130	3.45	33.15	14.61	3.00	0.00	36.79	64.58
MCG -01-13-025	2.64	49.85	60.00	1.00	0.00	10.00	75.00
MCG -01-24-12	4.09	28.49	60.00	7.3	0.56	45.96	48.53
MCG -02-12-050	3.76	45.02	51.18	4.4	0.97	24.64	0.00
MCG -03-34-064	66.99	34.81	40.03	8.34	0.73	51.88	28.4
MCG +04-22-042	7.14	39.29	5.02	2.96	0.00	89.14	62.74
MCG -05-23-016	12.03	44.73	21.8	6.55	0.00	21.65	53.7
MRK 18	8.81	66.2	5.00	2.01	2.00	10.00	0.00
MRK 50	1.17	47.48	29.83	1.88	1.73	24.38	29.42
MRK 352	1.28	37.03	20.54	2.13	0.00	21.08	64.36
MRK 417	15.55	31.97	5.00	9.11	0.00	59.39	90.00
MRK 501	1.33	34.81	18.02	1.53	1.99	88.36	56.87

Table 5.1: (continued)

Name	χ^2/ν	σ	Y	N	q	τ	i
MRK 915	9.24	32.08	21.26	3.87	0.00	64.40	47.27
NGC 4102	63.36	75.00	43.68	10.00	0.00	100	79.5
NGC 4388	12.69	21.92	30.66	9.43	0.00	39.12	63.27
NGC 4395	1.14	42.08	100	4.00	0.00	80.5	42.37
NGC 454	9.74	36.33	56.94	6.97	0.33	27.66	10.91
NGC 4686	2.50	24.84	5.06	3.4	0.00	87.87	85.26
NGC 4992	2.31	60.07	11.95	7.6	0.00	16.04	2.97
NGC 513	3.43	34.98	55.87	3.77	0.21	100	30.1
NGC 5252	9.75	20.14	60.00	1.83	0.00	15.85	90.00
NGC 526A	8.72	35.79	9.85	3.78	0.00	29.4	53.84
NGC 5728	14.18	27.49	35.7	8.5	0.00	36.25	55.94
NGC 612	14.19	15.28	5.00	6.53	2.00	18.71	84.06
NGC 7172	13.94	44.75	35.18	8.68	1.37	14.36	90.00
NGC 7582	82.89	46.75	60.00	7.86	0.00	100	11.62
NGC 7682	2.25	27.66	33.78	10.00	0.5	100	68.66
NGC 788	7.47	28.67	20.52	4.06	0.00	20.33	84.18
NGC 973	4.78	43.25	60.00	4.84	0.00	40.66	22.72
PGC 13946	3.48	17.55	5.00	1.36	2.00	29.94	75.65
SBS 1301+540	1.18	19.05	9.76	1.21	0.00	68.47	19.65
UGC 03601	6.18	33.97	10.49	2.27	0.00	42.67	79.71
UGC 04013	3.52	32.61	23.18	4.8	0.00	78.4	50.83
UGC 06728	2.02	47.28	15.77	1.85	0.00	39.93	51.87
UGC 11871	10.18	38.94	8.88	6.14	0.00	17.53	32.77
UGC 12282	6.18	33.1	22.56	2.65	0.00	60.87	36.46
UGC 12741	3.49	19.53	48.14	6.36	1.13	88.33	59.91
UM 614	3.86	46.45	16.03	2.05	1.17	51.55	40.07

Table 5.2: Best-fit optional model parameters

		NLR Components		Host Galaxy				BB Model		Silicate Model		
Name	χ^2/ν	log(U)	Covering Factor	γ	U_{min}	q_{PAH}	f_{host}	Temp. (K)	BB Frac.	$\tau_{9.7\mu m}$	β	type
2MASX J05580206-3820043	9.25	-0.24	0.034					1789	0.22	0.3148		0
2MASX J09043699+5536025	1.39	-1.042	0.106	0.00432	14.99	1.13	0.341			0.6468		0
2MASX J09112999+4528060	3.55			0.00169	20	1.12	0.418	1801	0.024	0.9001	0.0219	2
2MASX J19595975+6508547	1.75	-1.389	0.026							0.7982		1
ARK 120	6.52							1801	0.205	0.2267		0
ARK 347	6.06	-0.121	0.034					1748	0.134	0.3817	0.6454	2
CGCG 041-020	4.3			0.00003	19.83	4.38	0.273			0.5224	0	2
CGCG 118-036	5.44	-0.136	0.065	0	12	3.91	0.403			1.2715		1
CGCG 420-015	23.23	0.241	0.068							0.1307	0	2
ESO 005-G004	11.62			0	7	4.58	0.476			1.2632		1
ESO 121-IG028	1.47									0.79	0	2
ESO 140-G043	10.69	0.107	0.023	0.0005	10	3.37	0.048	1702	0.081	0.2543	0.2116	2
ESO 141-G055	8.27	-0.211	0.086							0.6185		1
ESO 157-G023	5.26							1801	0.16			
ESO 198-024	2.52									0.2423	0	2
ESO 297-G018	2.52			0	19.99	3.89	0.178			0.5816	0.1205	2
ESO 323-077	33.48	-0.028	0.057	0.37187	0.84	4.58	0.189	1455	0.098	0.109		0
ESO 374-G044	18.45	0.236	0.196							0.1908		1
ESO 417-G006	1.8							1800	0.05	0.7581		1
ESO 426-G002	3.83									0.3387	0	2
ESO 506-G027	4.6			0	15.01	1.78	0.06			1.4496		0
ESO 511-G030	6.21							1800	0.319	0.4708	0.4101	2

Table 5.2: (continued)

		NLR Components		Host Galaxy				BB Model		Silicate Model		
Name	χ^2/ν	$\log(U)$	Covering Factor	γ	U_{min}	q_{PAH}	f_{host}	Temp. (K)	BB Frac.	$\tau_{9.7\mu m}$	β	type
ESO 548-G081	9.81	-0.21	0.02					1801	0.193	0.1344		0
ESO 549-G049	22.78	-0.245	0.276	0.00575	3	3.34	0.616			1.1906		1
IC 1816	10.13	-0.241	0.033	0.00166	0.13	0.47	0.356	1760	0.115	0.654	1	2
IRAS 05218-1212	10.25	0.162	0.129					1801	0.054	0.1872		0
LEDA 088639	5.42	-0.223	0.035					1801	0.121			
LEDA 089420	3.27			0.00117	20	2.11	0.489					
LEDA 178130	3.45							1801	0.145	0.6945	0.6065	2
MCG -01-13-025	2.64							1800	0.245	0.6133		0
MCG -01-24-12	4.09	0.244	0.08	0.00901	7.47	0.47	0.058			0.6801	0	2
MCG -02-12-050	3.76	-1.24	0.041							0.8146		1
MCG -03-34-064	66.99	0.756	0.157	0.00934	10	1.78	0.061			0.5581	0.2607	2
MCG +04-22-042	7.14	-0.243	0.097					1801	0.095			
MCG -05-23-016	12.03	0.019	0.051					1788	0.1	0.5813	0.7352	2
MRK 18	8.81	-1.582	0.208	0.00494	9.99	4.2	0.687			0.3661		1
MRK 50	1.17									0.561		0
MRK 352	1.28							1801	0.168			
MRK 417	15.55	-0.181	0.129					1801	0.11	0.1903	0.8359	2
MRK 501	1.33	-1.589	0.029					1801	0.19	0.3761		1
MRK 0915	9.24	0.312	0.164							0.5671		0
NGC 4102	63.36	-0.241	0.025	0.00054	4.99	4.42	0.415	1784	0.03			
NGC 4388	12.69	0.161	0.084	0.00869	0.69	0.47	0.142	118	0.238	1.0774	0	2
NGC 4395	1.14	-0.751	0.058	0.00465	1.48	0.47	0.241	1800	0.082			
NGC 454	9.74			0	4.99	1.11	0.048			0.6784	0	2
NGC 4686	2.5	0.244	0.011	0.00243	9.99	1.12	0.226	1800	0.177			
NGC 4992	2.31	-0.91	0.025							1.8822		1
NGC 513	3.43			0.00055	10	3.18	0.493					

Table 5.2: (continued)

		NLR Components		Host Galaxy				BB Model		Silicate Model		
Name	χ^2/ν	log(U)	Covering Factor	γ	U_{min}	q$_{PAH}$	f_{host}	Temp. (K)	BB Frac.	$\tau_{9.7\mu m}$	β	type
NGC 5252	9.75							1801	0.254	0.4581		0
NGC 526A	8.72	-0.245	0.078							0.21	0.1597	2
NGC 5728	14.18			0.74364	4.01	4.58	0.48			0.8411	0.0248	2
NGC 612	14.19			0.00039	24.81	4.58	0.802			0.7804		1
NGC 7172	13.94	0.125	0	0.00983	9.99	1.77	0.414	1720	0.188	2.1449		0
NGC 7582	82.89			0.00727	19.86	3.23	0.729			0.8412	0.2752	2
NGC 7682	2.25	-0.608	0.132	0.00201	13.8	1.13	0.185			0.9921		1
NGC 788	7.47							1700	0.064	0.7344	0.7565	2
NGC 973	4.78			0.00565	19.99	1.13	0.163			1.3903		0
PGC 13946	3.48	-1.357	0.096	0.0093	15	3.15	0.466			1.1169		1
SBS 1301+540	1.18							1801	0.284	0.4679	0.4402	2
UGC 03601	6.18	-0.052	0.083	0	3.26	3.19	0.263					
UGC 04013	3.52	-0.099	0.088	0.03393	19.99	0.47	0.142	1801	0.093	0.4502	0.3966	2
UGC 06728	2.02							1801	0.175	0.2442	0.6614	2
UGC 11871	10.18	-1.588	0.175	0.00575	5	0.47	0.498			0.9219		1
UGC 12282	6.18			0	6.99	3.89	0.2			0.4431		0
UGC 12741	3.49	-2.343	0.003	0.00121	3.99	4	0.475			0.7938		0
UM 614	3.86	0.224	0.09							0.3095		0

2MASX J0558 ESO Danish	2MASX J0904 SDSS	2MASX J0911 SDSS	2MASX J1959 2MASS	ARK 120 SDSS
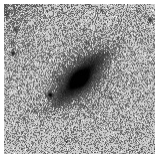			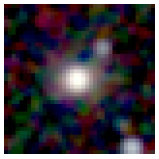	
ARK 347 SDSS	CGCG 041-020 SDSS	CGCG 118-036 SDSS	CGCG 420-015 WFPC 2	ESO 005-G004 2MASS
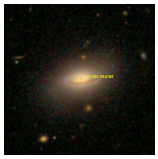			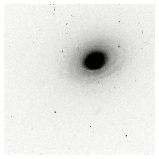	
ESO 121-IG028 DSS	ESO 140-G043 DSS Schmidt	ESO 141-G055 DSS	ESO 157-G023 DSS	ESO 198-024 2MASS
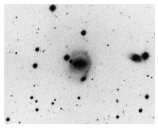	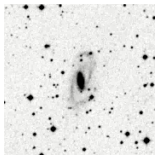	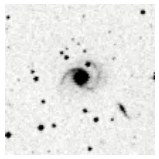		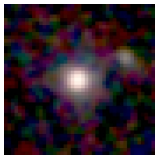
ESO 297-G018 2MASS	ESO 323-077 WFPC2	ESO 374-G044 DSS	ESO 417-G006 DSS	ESO 426-G002 DSS
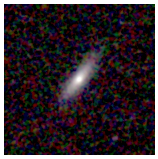	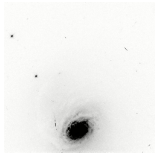	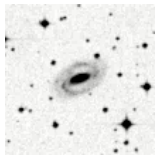	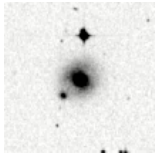	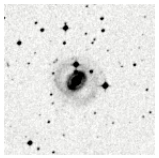
ESO 506-G027 2MASS	ESO 511-G030 DSS	ESO 548-G081 2MASS	ESO 549-G049 DSS	IC 1816 WFPC2
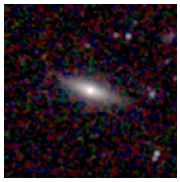	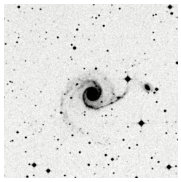			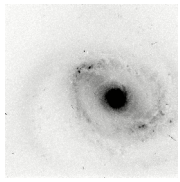

Table 5.3: Thumbnails of host galaxies taken from NED

IRAS 05218 DSS	LEDA 088639 WFPC2	LEDA 089420 2MASS	LEDA 178130 2MASS	MCG -01-13-025 SDSS
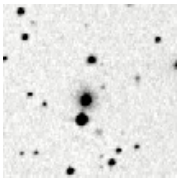	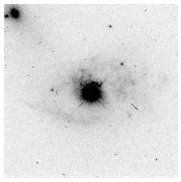	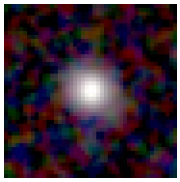	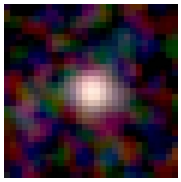	
MCG -01-24-12 DSS	MCG -02-12-050 DSS	MCG -03-34-064 DSS	MCG +04-22-042 SDSS	MCG -05-23-016 DSS
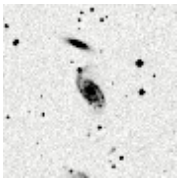	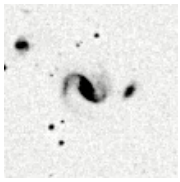	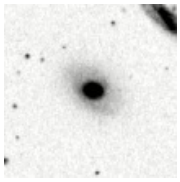		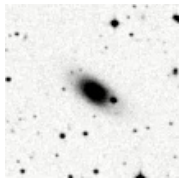
MRK 18 SDSS	MRK 50 SDSS	MRK 352 SDSS	MRK 417 SDSS	MRK 501 SDSS
	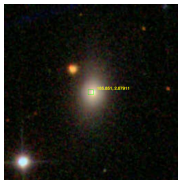			
MRK 0915 WFPC2	NGC 4102 SDSS	NGC 4388 SDSS	NGC 4395 SDSS	NGC 454 2MASS
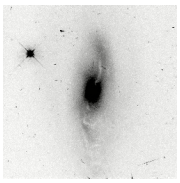		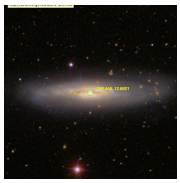	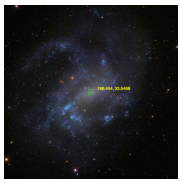	
NGC 4686 SDSS	NGC 4992 SDSS	NGC 513 SDSS	NGC 5252 SDSS	NGC 526A DSS
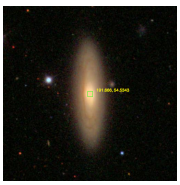	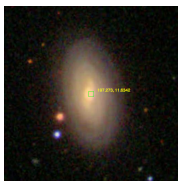	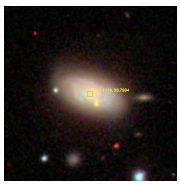		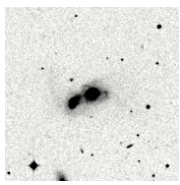

Table 5.4: Thumbnails of host galaxies (continued)

NGC 5728 DSS	NGC 612 DSS	NGC 7172 WFPC2	NGC 7582 GALEX	NGC 7682 SDSS
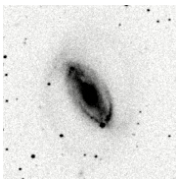	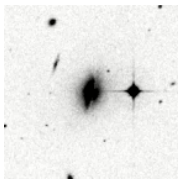	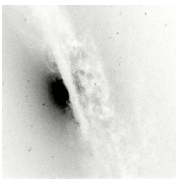	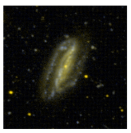	
NGC 788 SDSS	NGC 973 2MASS	PGC 13946 DSS	SBS 1301+540 SDSS	UGC 03601 2MASS
		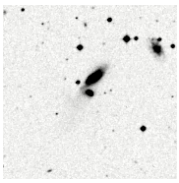		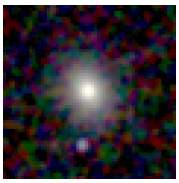
UGC 04013 WFPC2	UGC 06728 2MASS	UGC 11871 SDSS	UGC 12282 2MASS	UGC 1274 SDSS
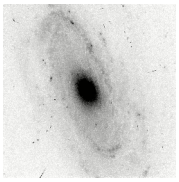	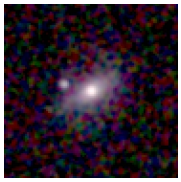	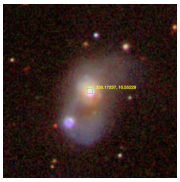	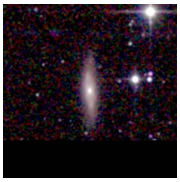	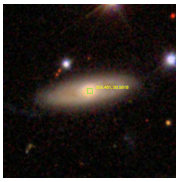
UM 614 SDSS				
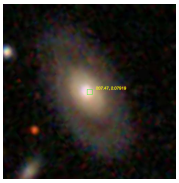				

Table 5.5: Thumbnails of host galaxies (continued)

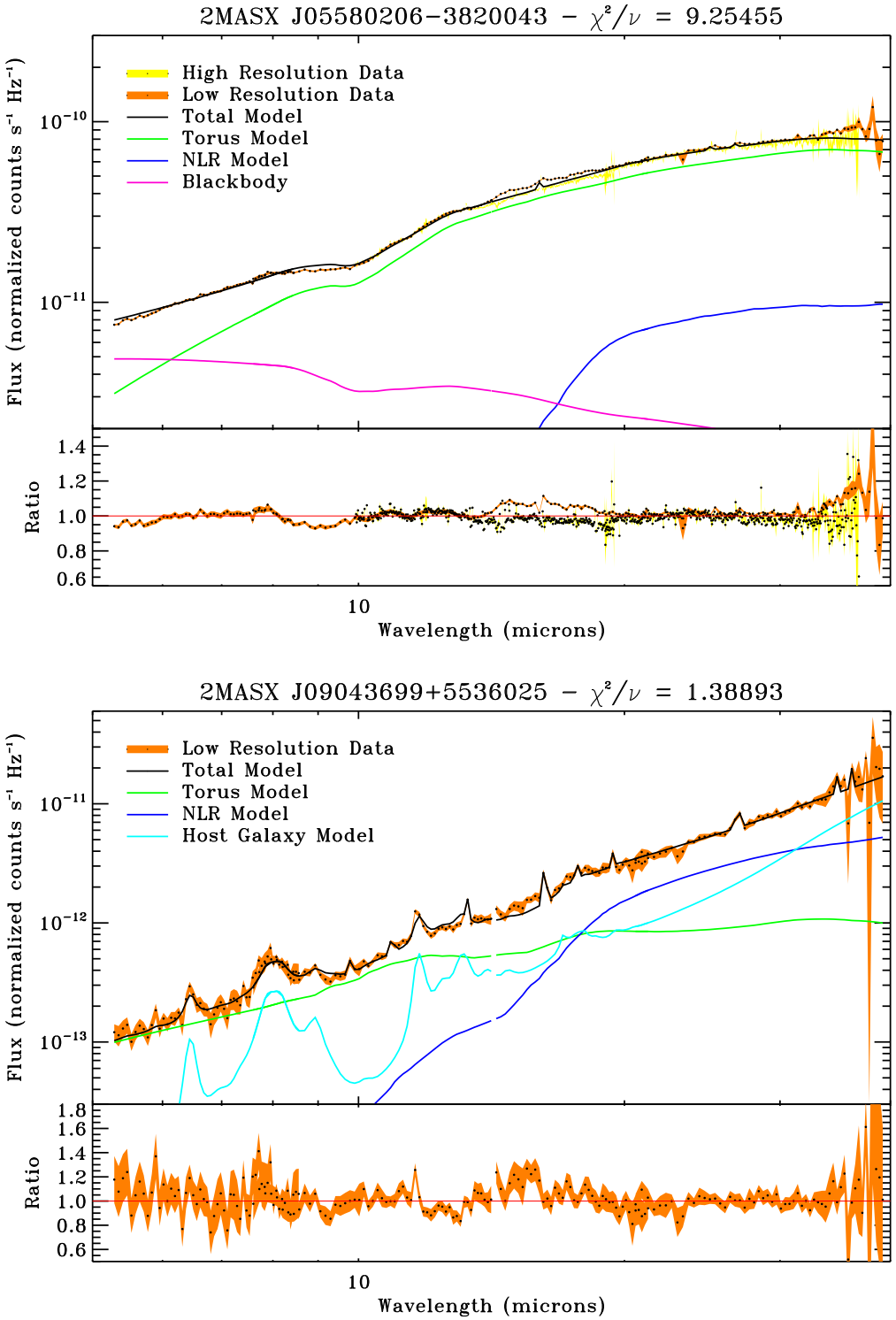

Figure 5.9: Complete models

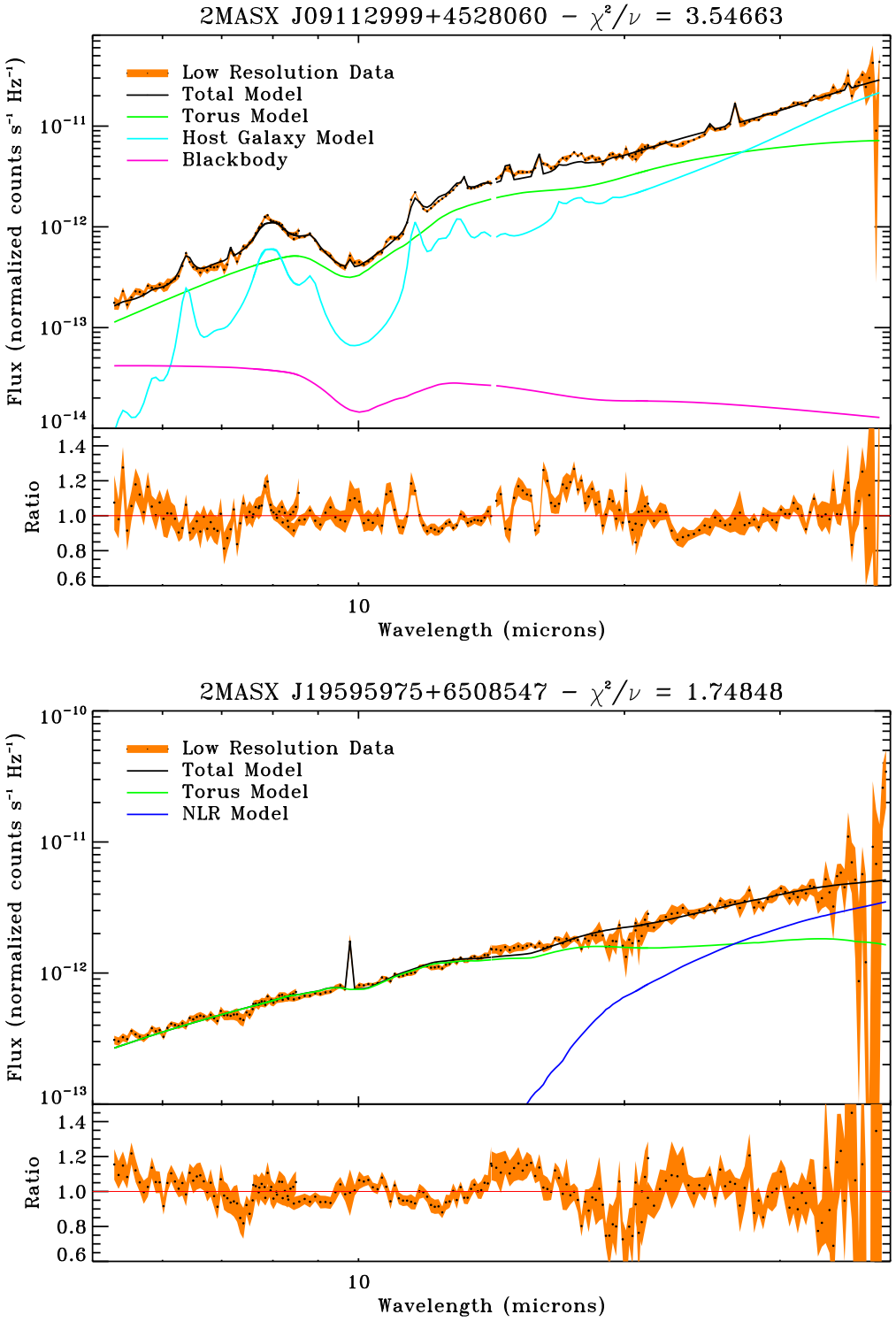

Figure 5.9: (continued)

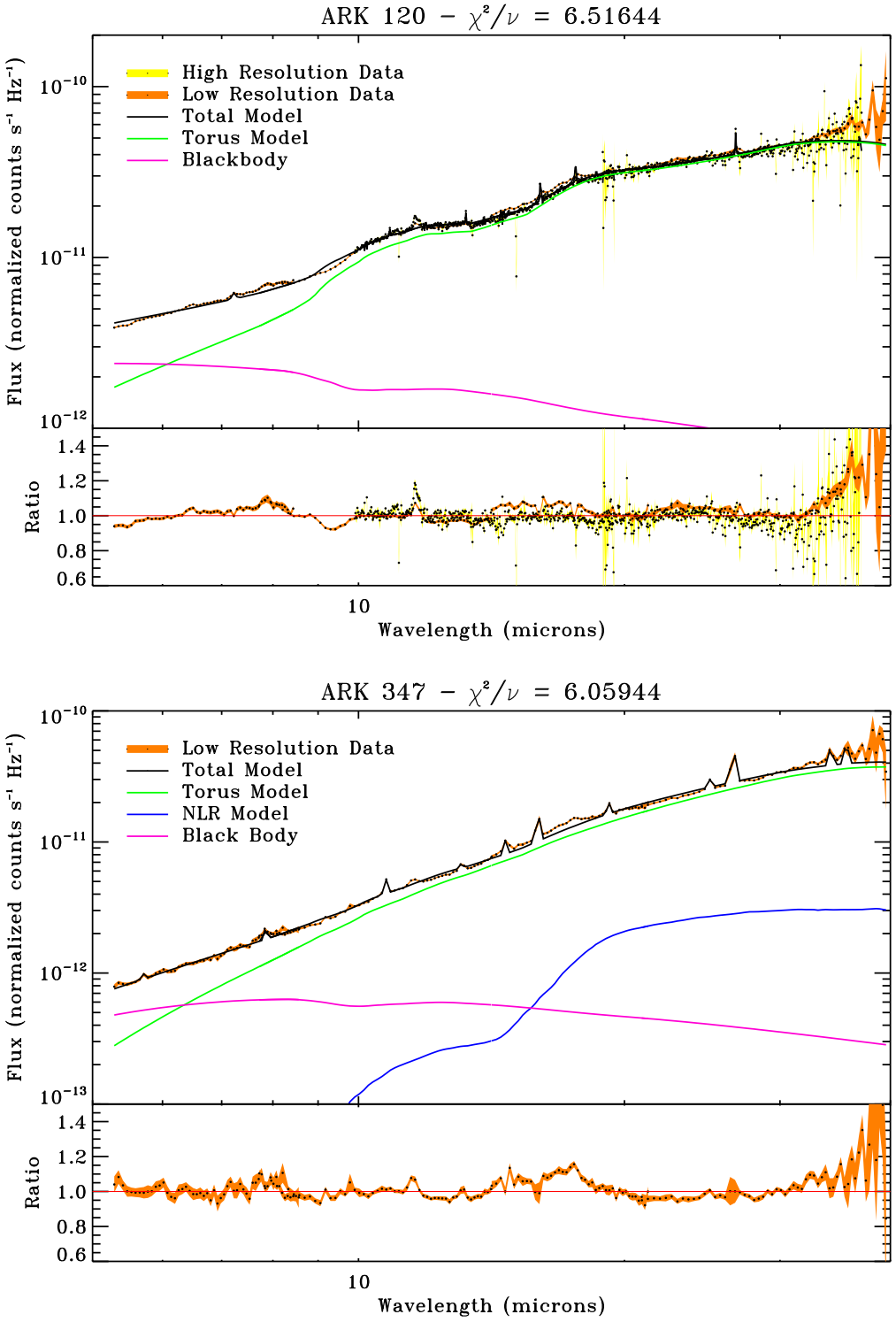

Figure 5.9: (continued)

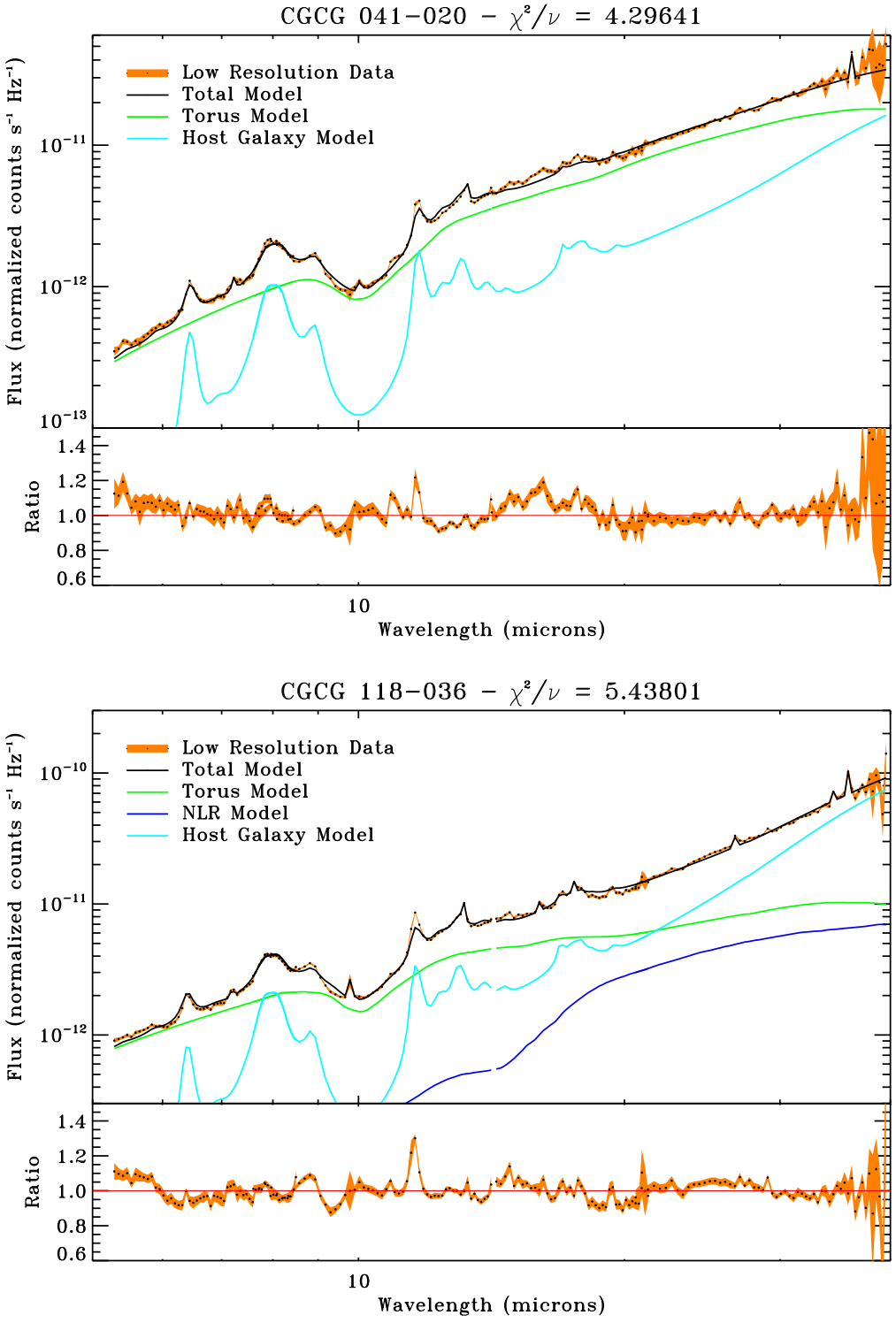

Figure 5.9: (continued)

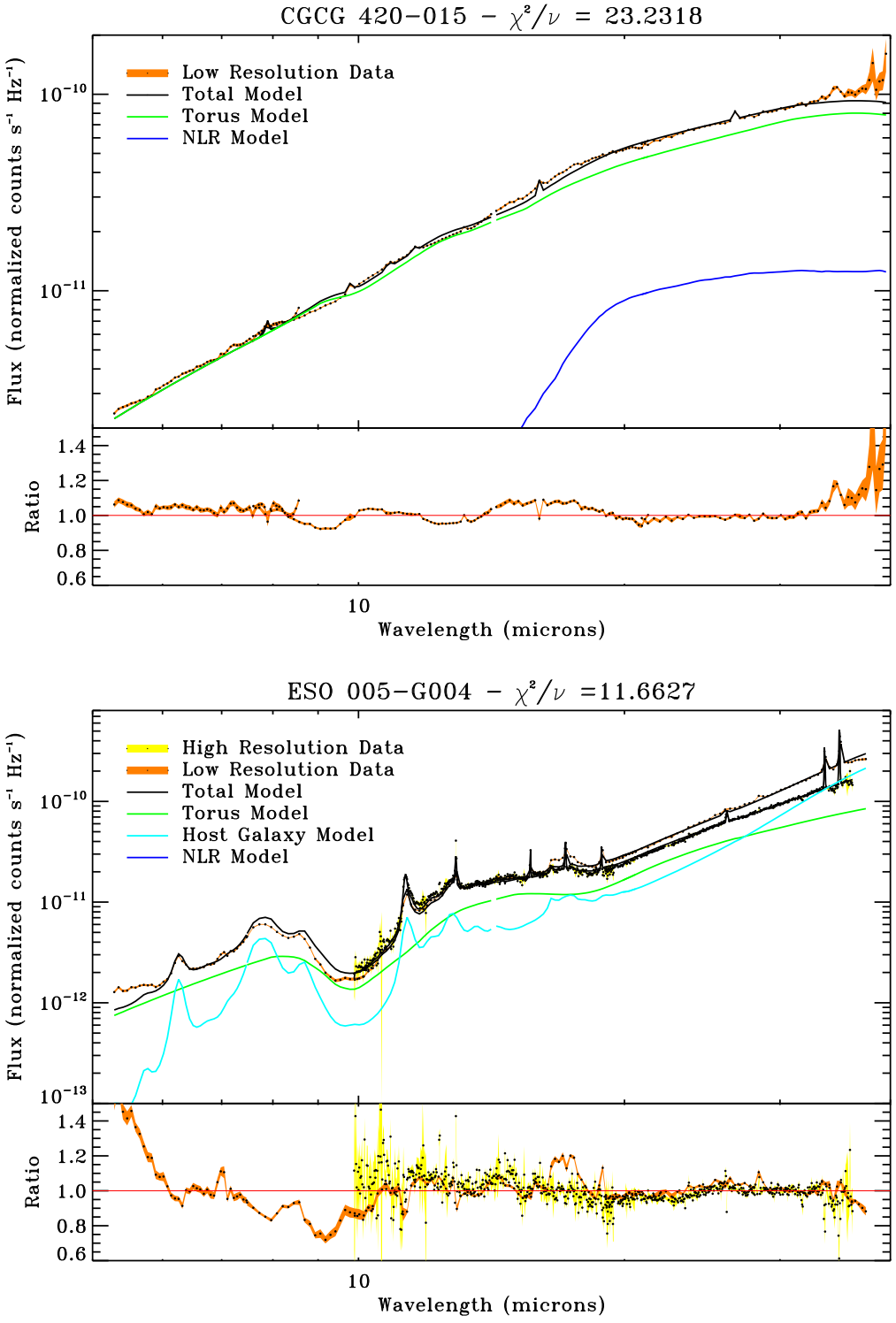

Figure 5.9: (continued)

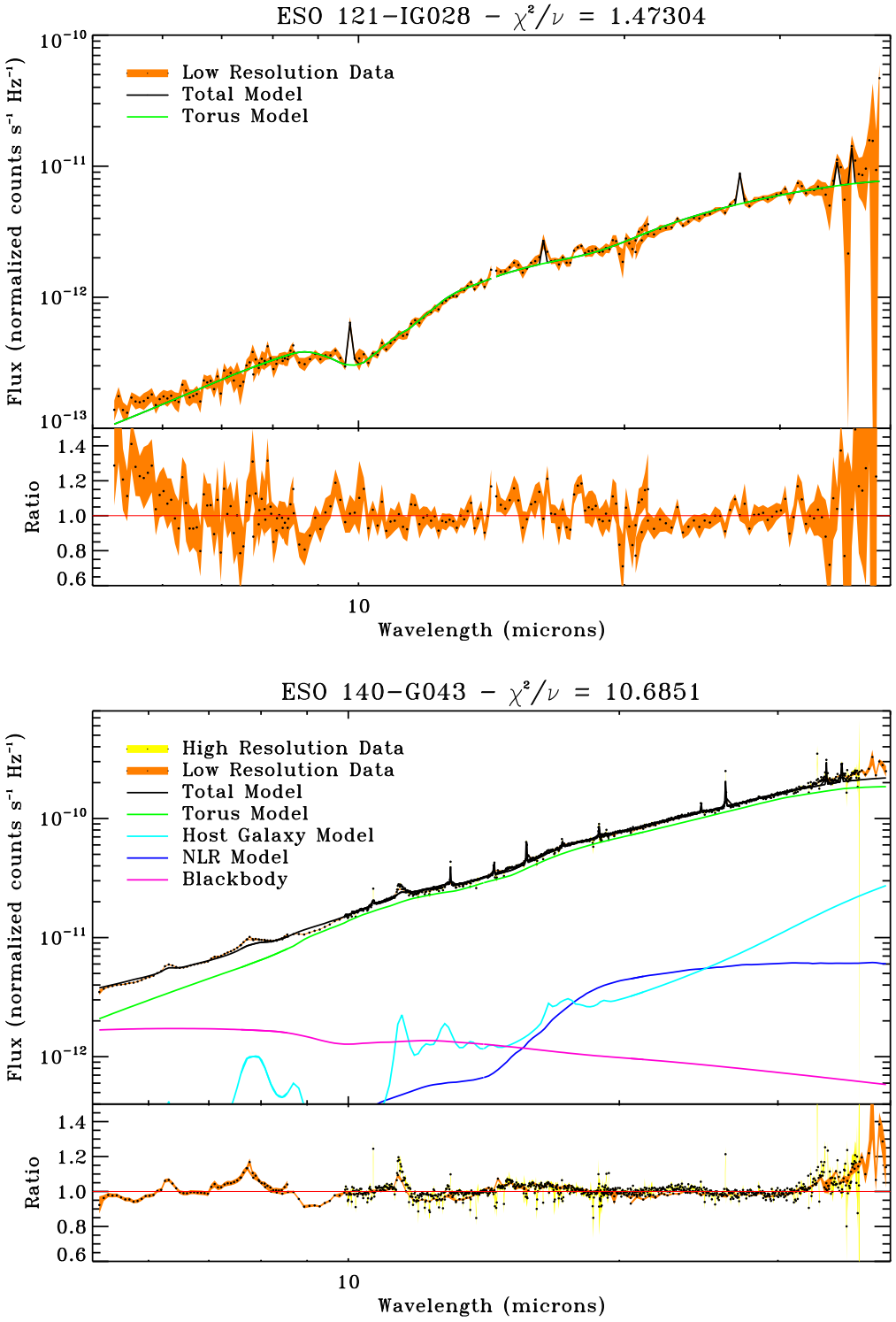

Figure 5.9: (continued)

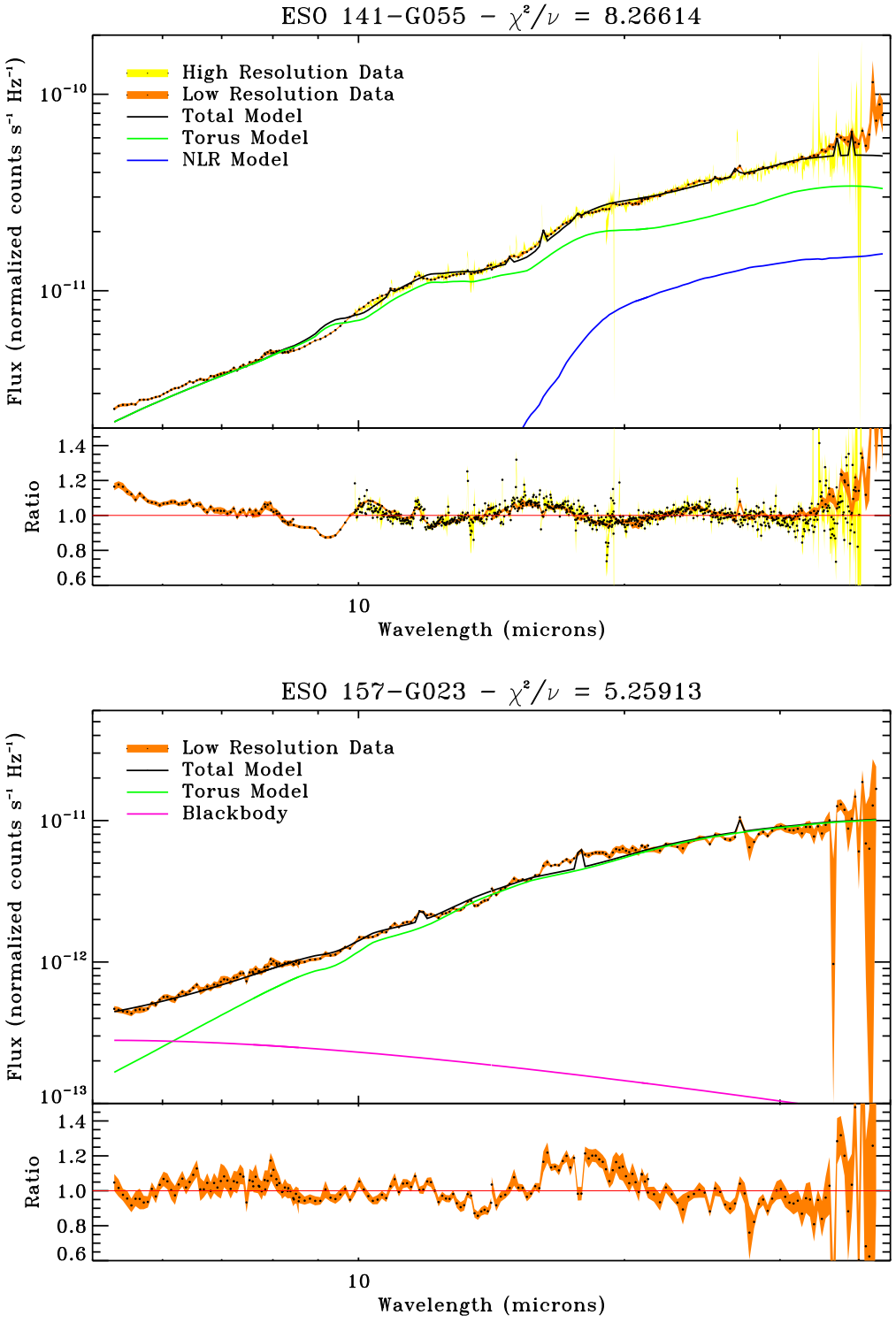

Figure 5.9: (continued)

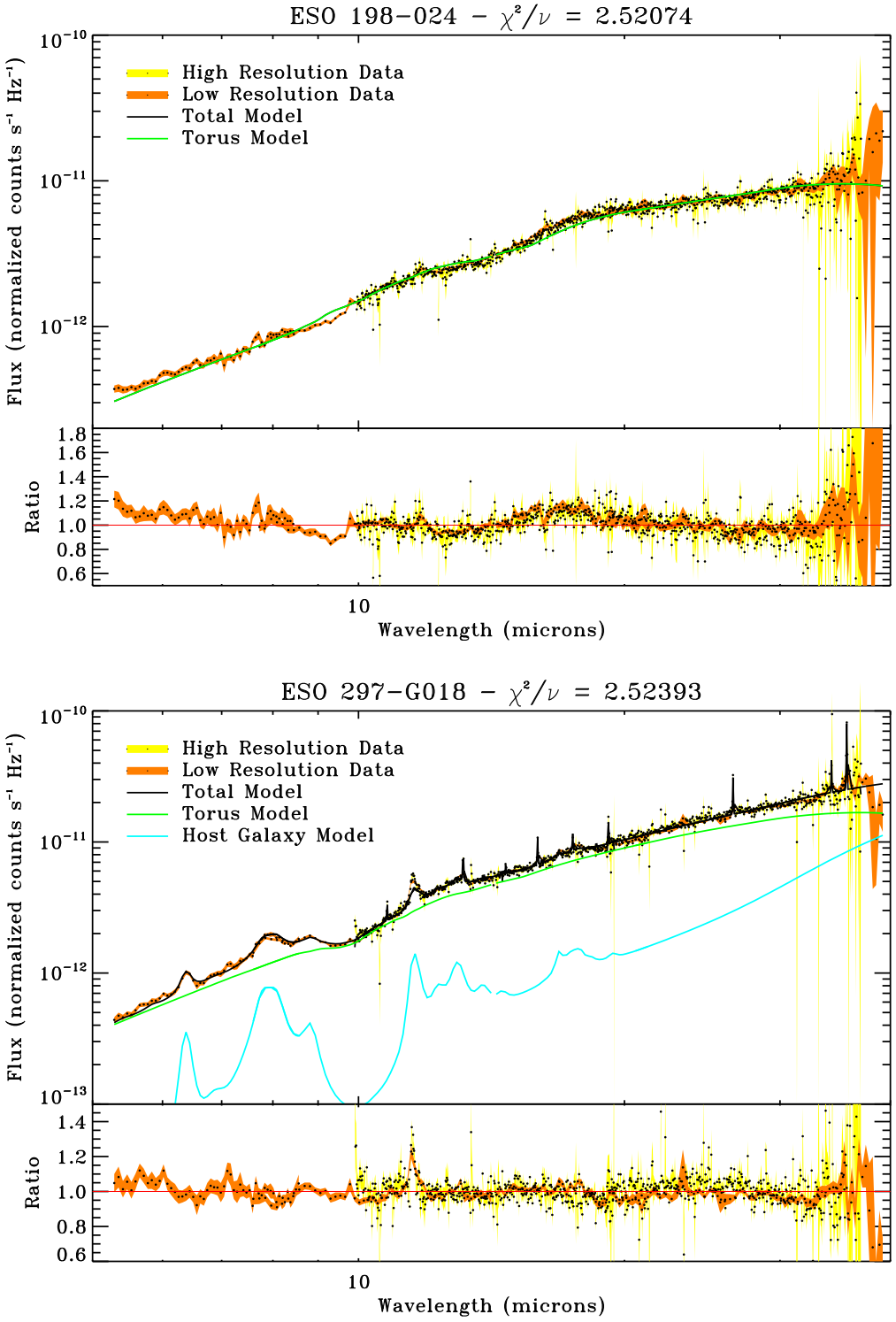

Figure 5.9: (continued)

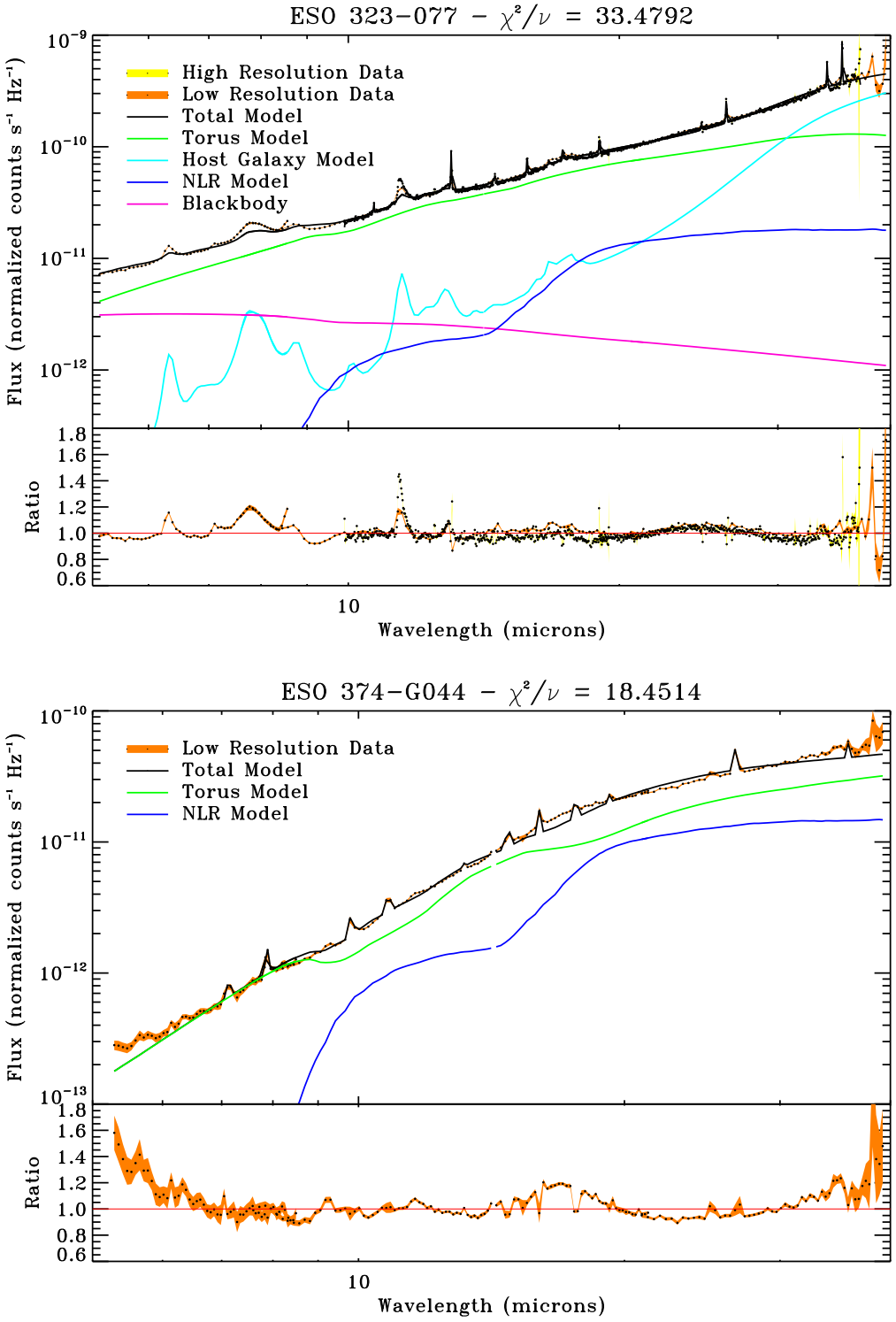

Figure 5.9: (continued)

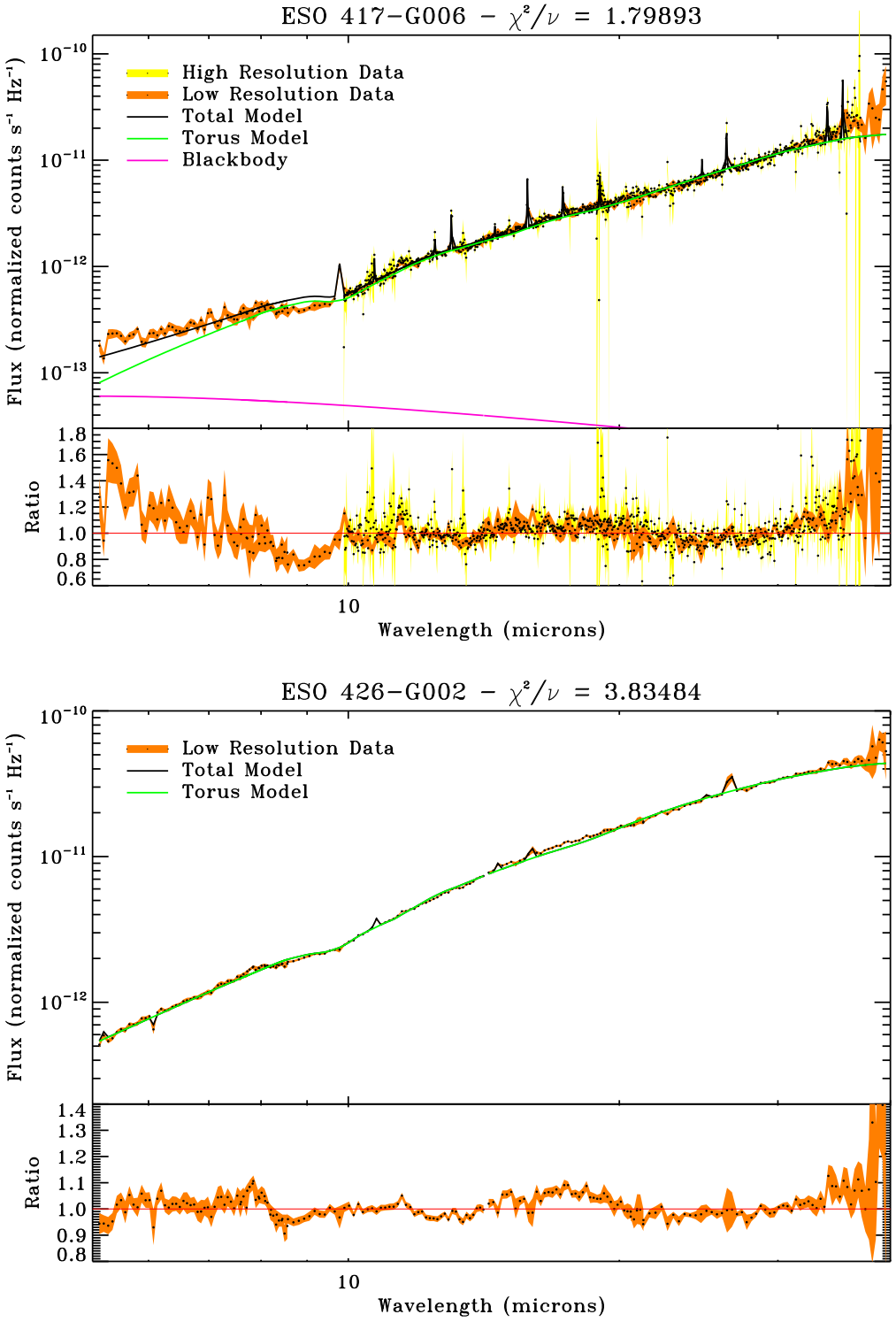

Figure 5.9: (continued)

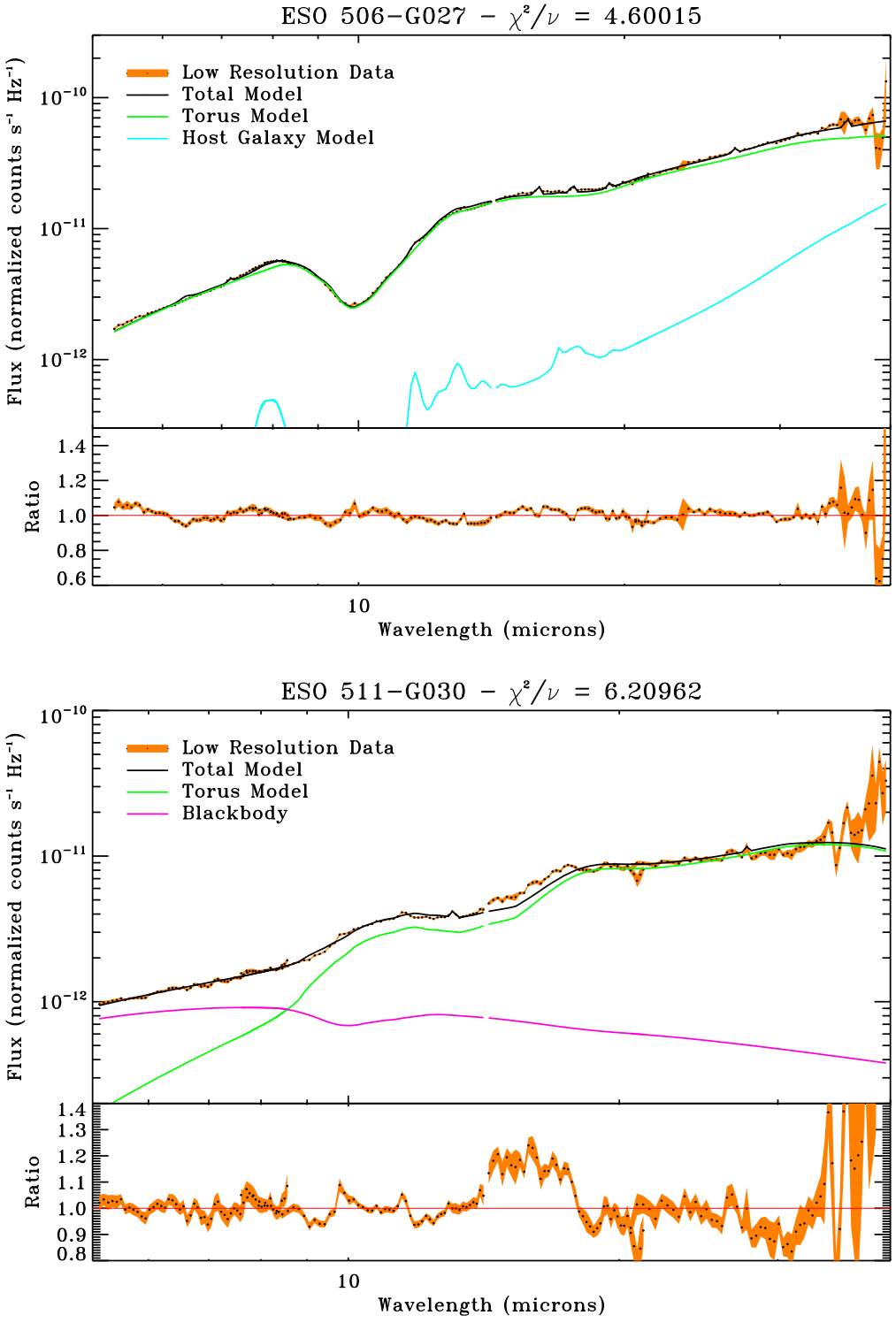

Figure 5.9: (continued)

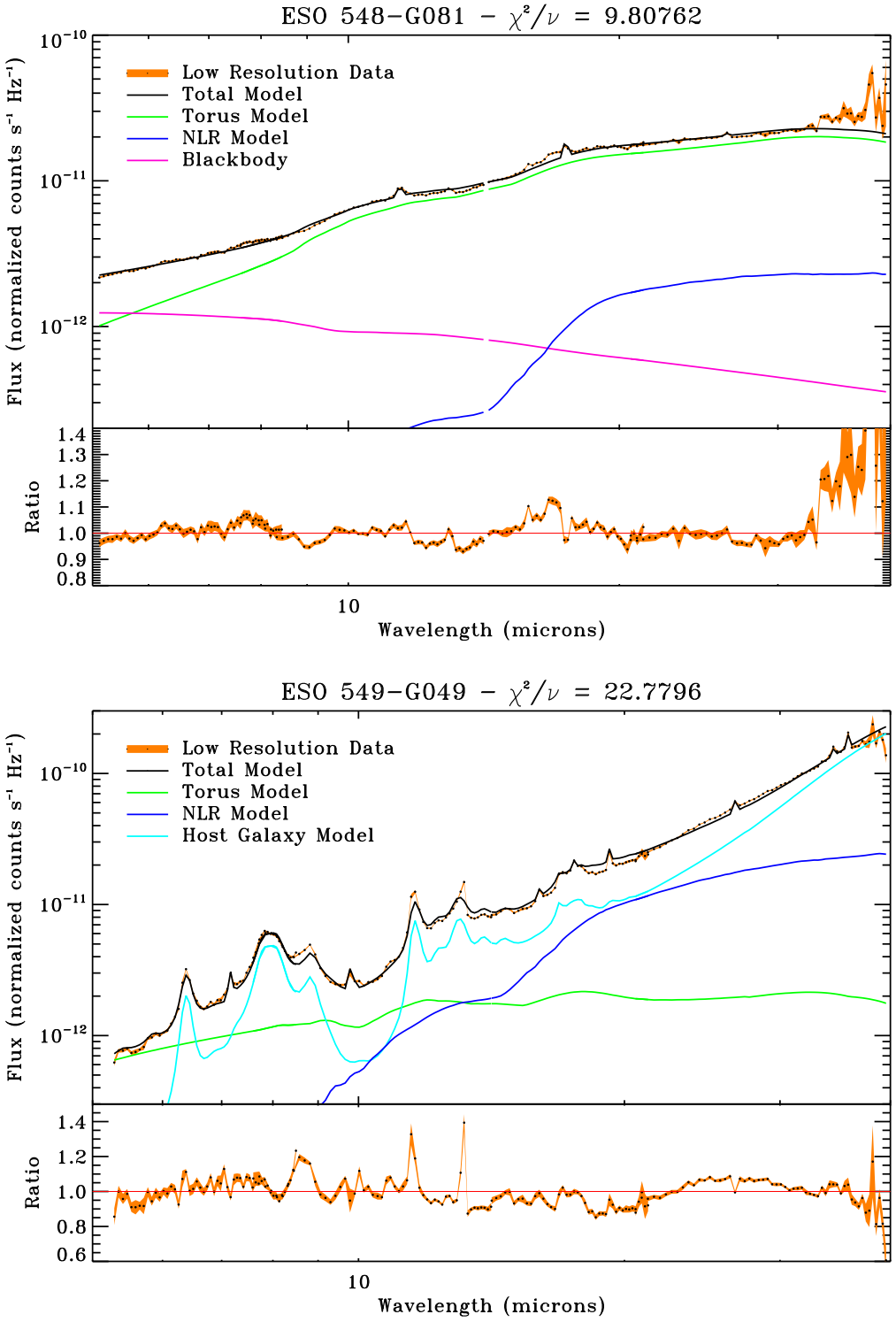

Figure 5.9: (continued)

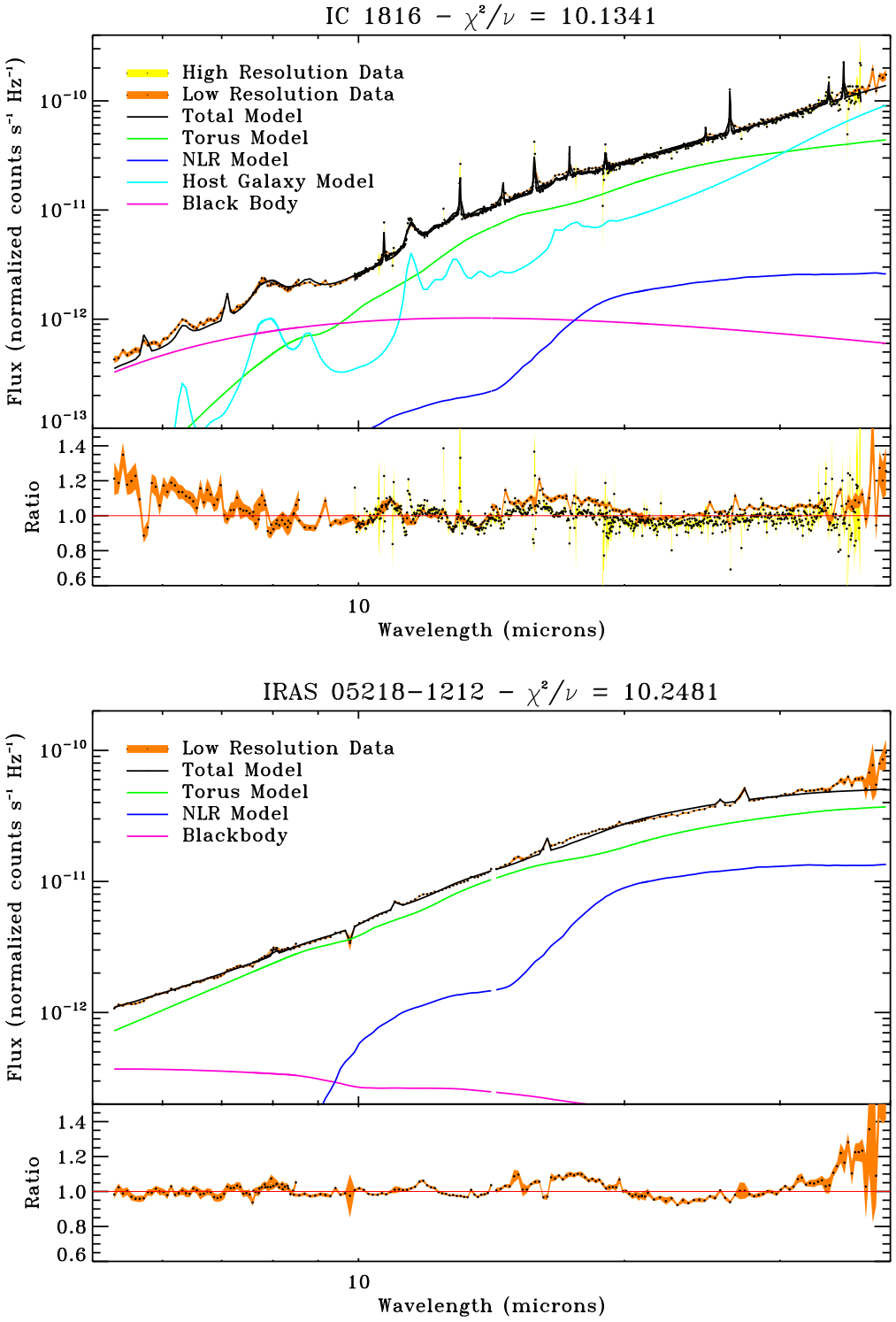

Figure 5.9: (continued)

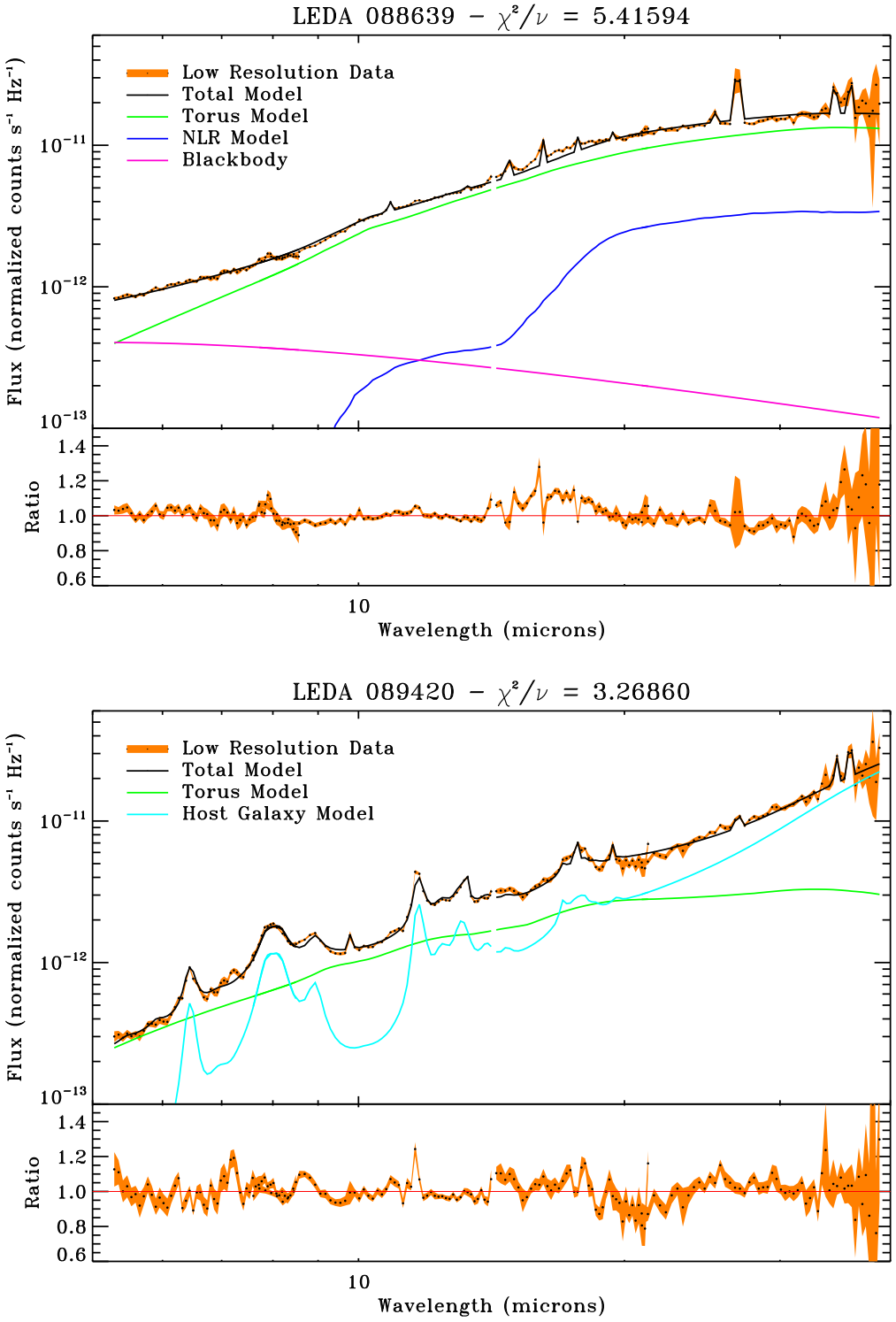

Figure 5.9: (continued)

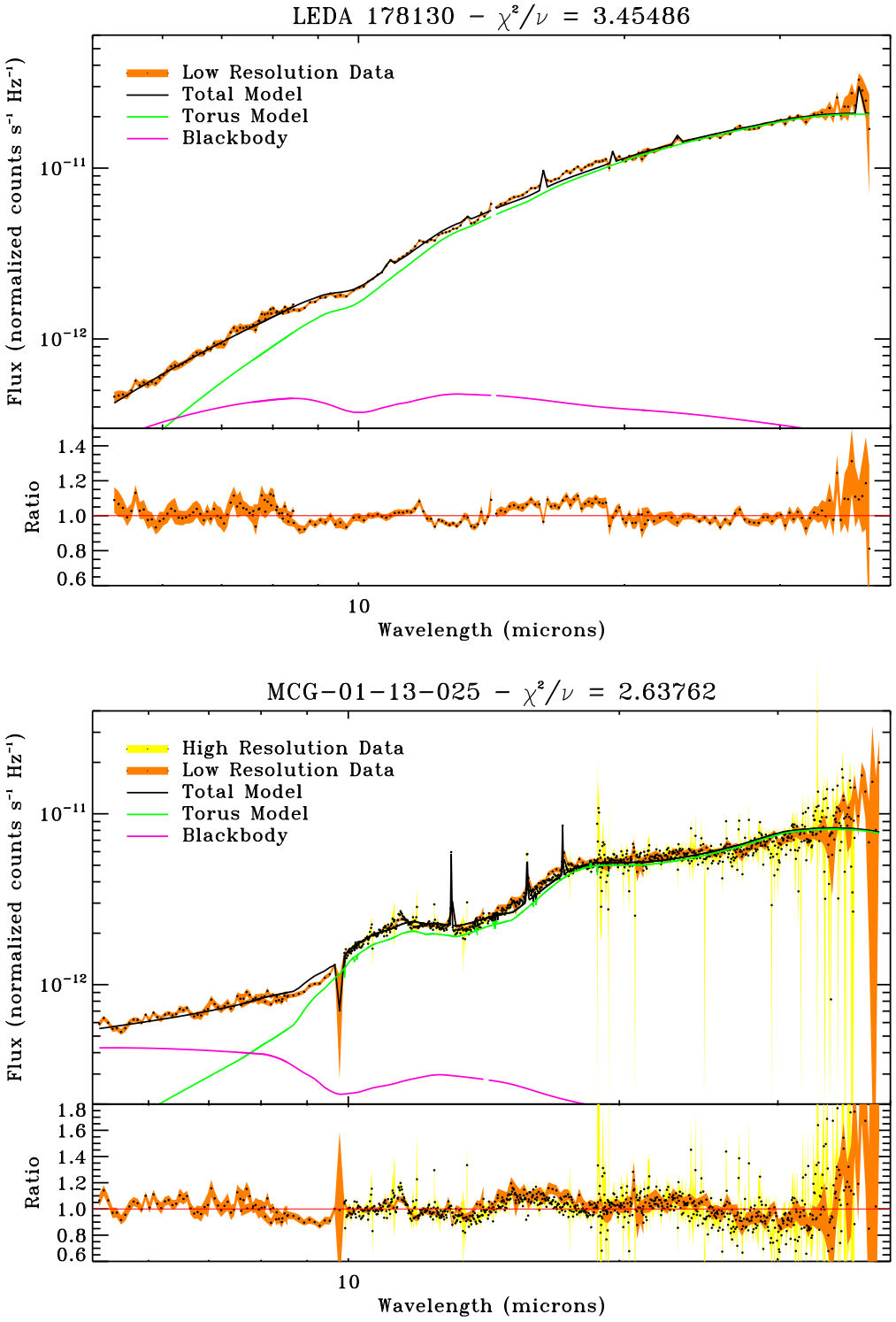

Figure 5.9: (continued)

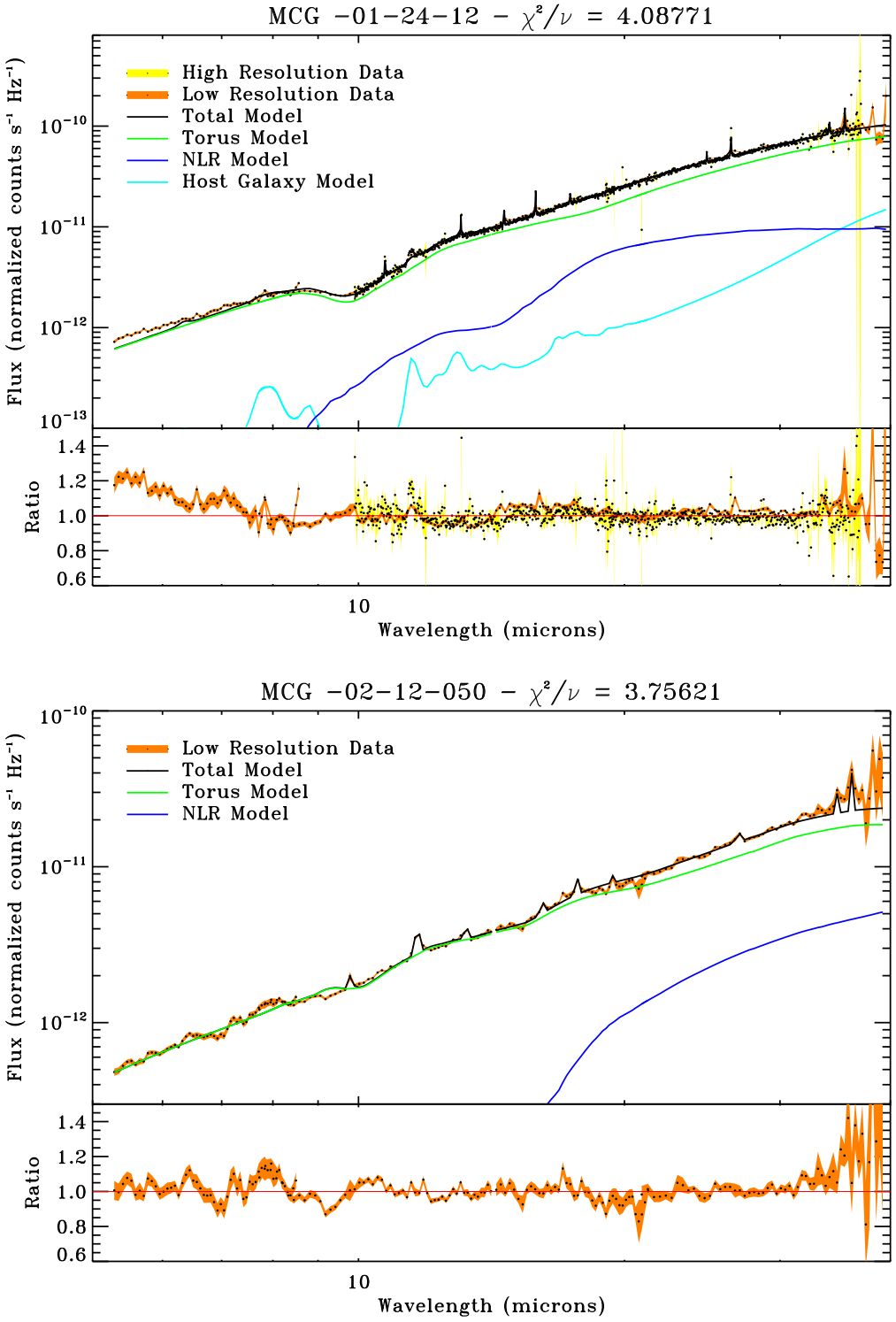

Figure 5.9: (continued)

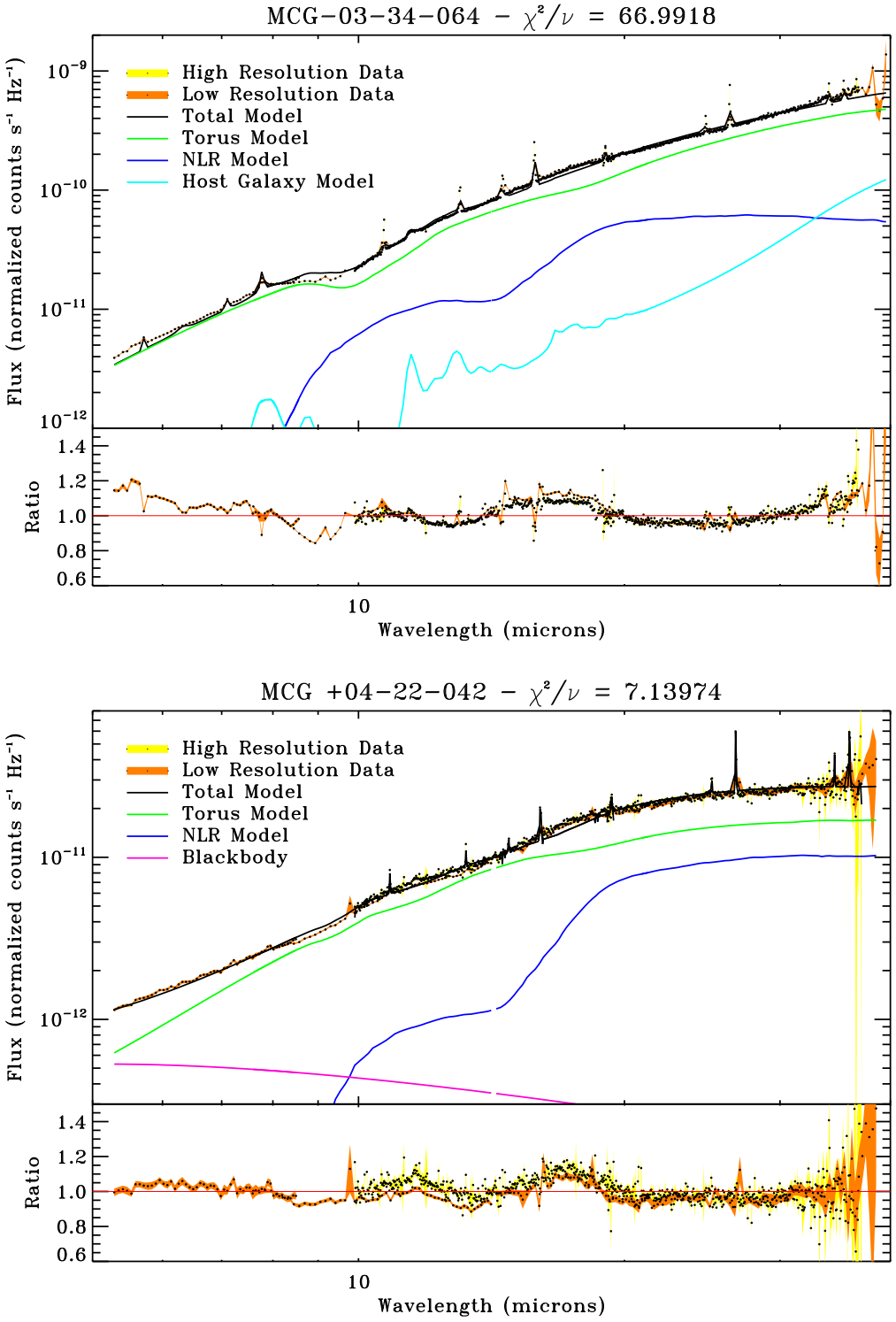

Figure 5.9: (continued)

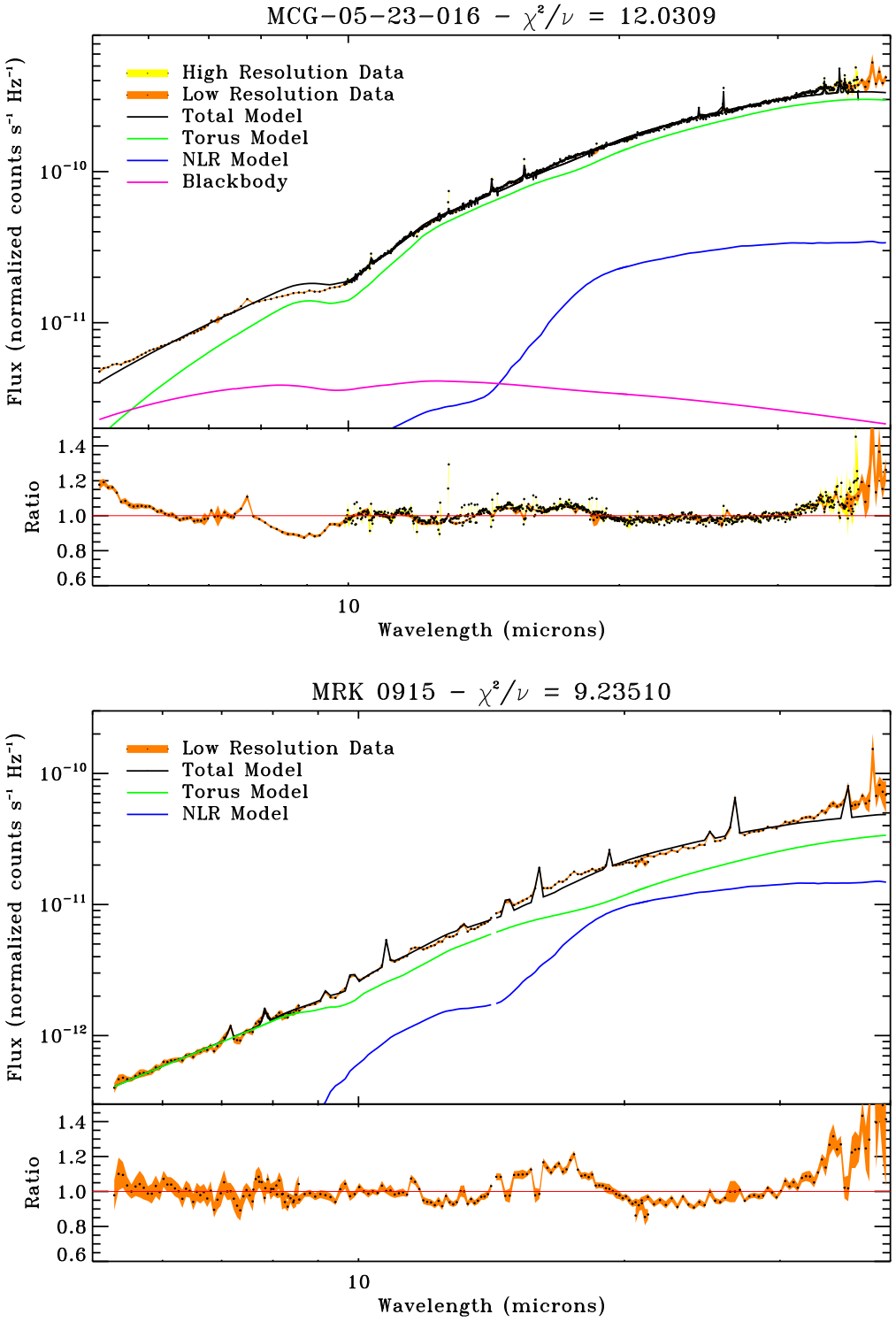

Figure 5.9: (continued)

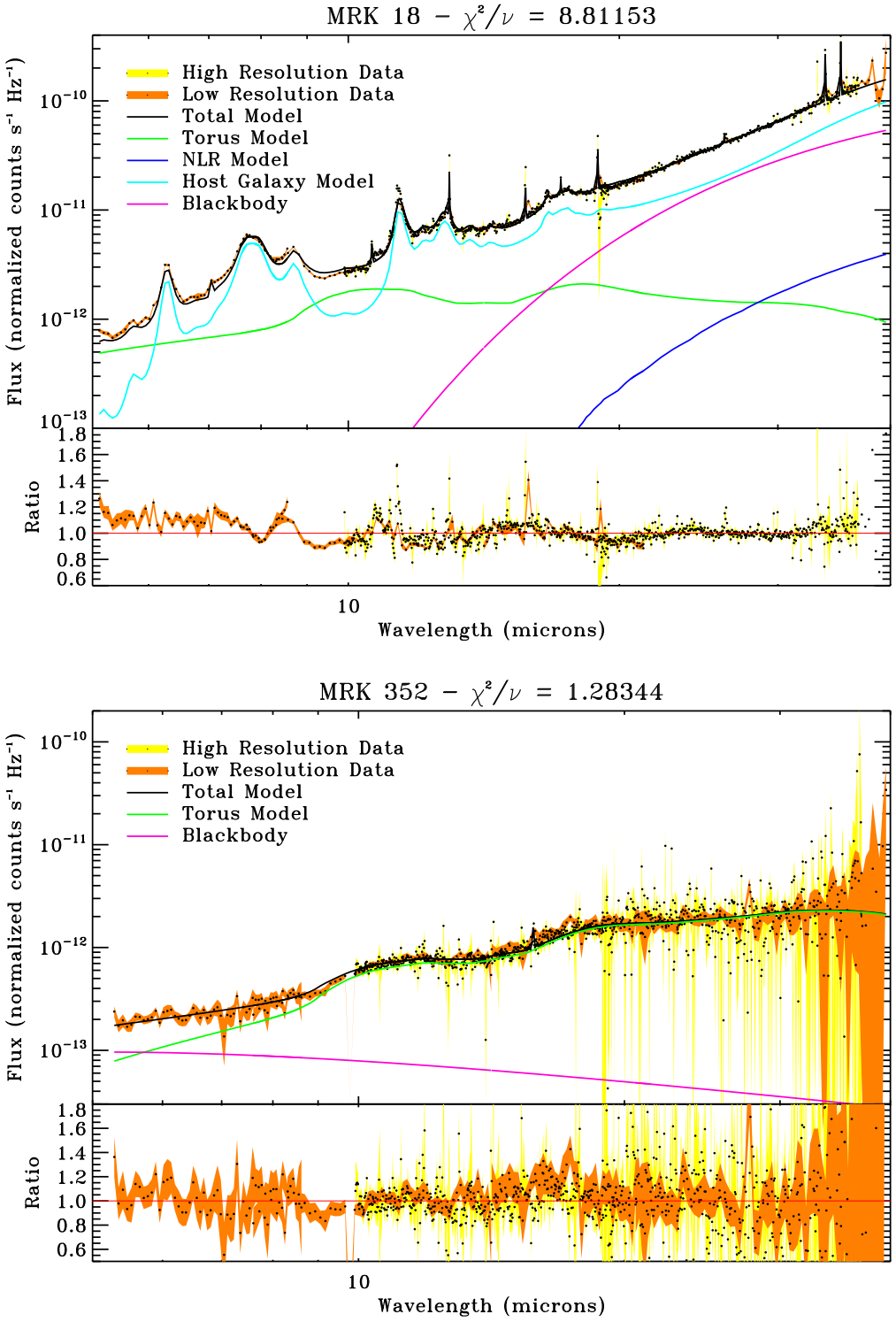

Figure 5.9: (continued)

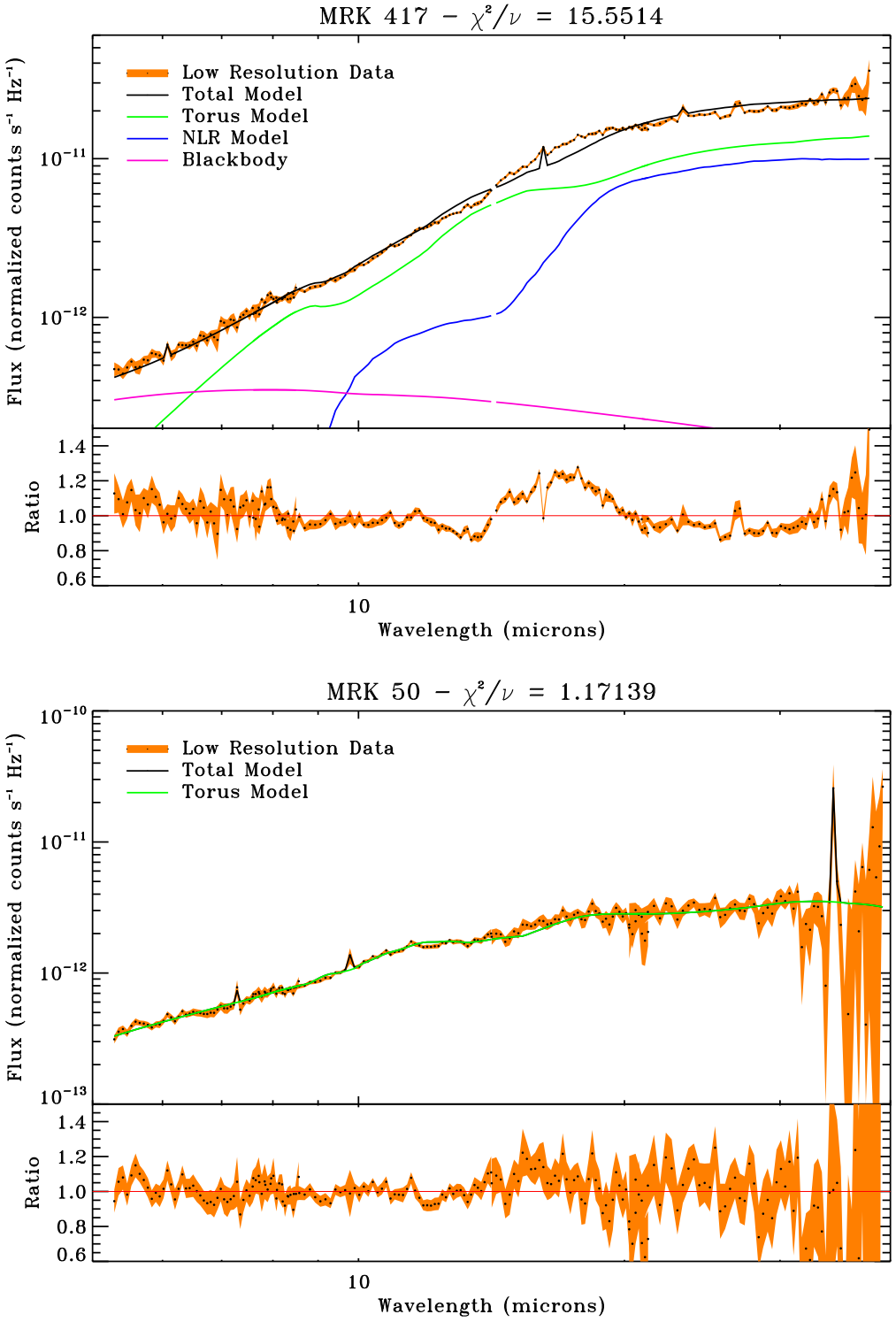

Figure 5.9: (continued)

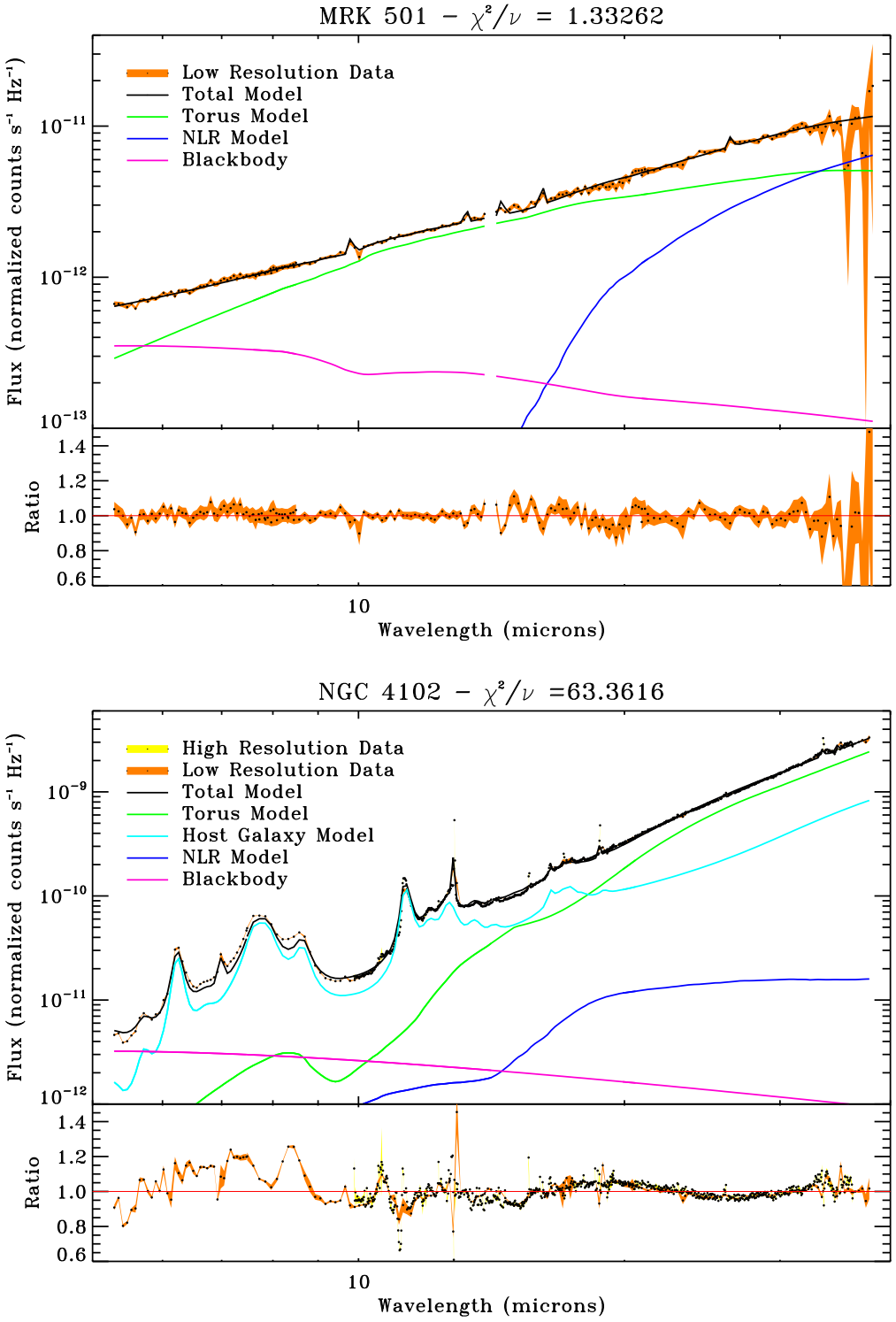

Figure 5.9: (continued)

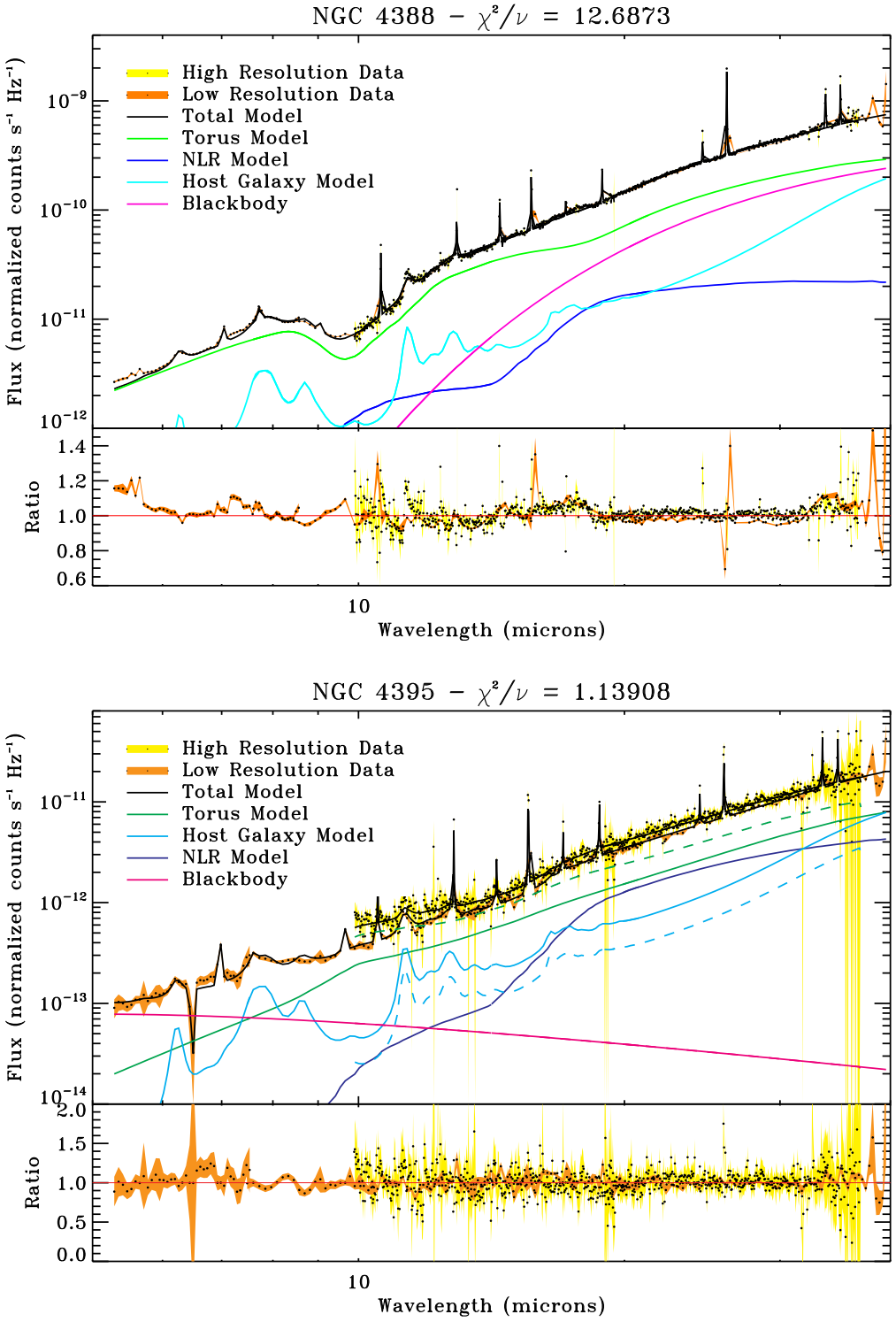

Figure 5.9: (continued)

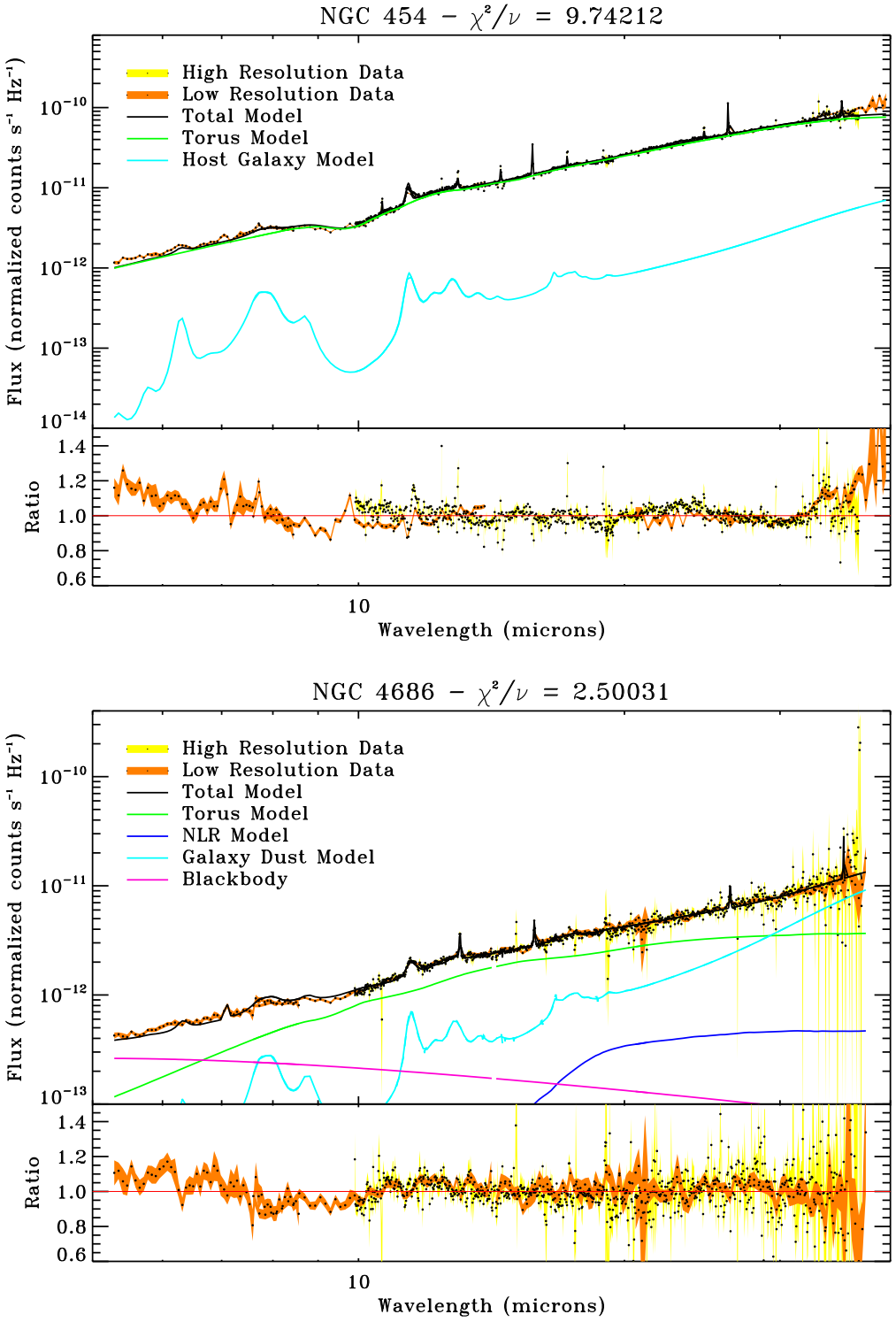

Figure 5.9: (continued)

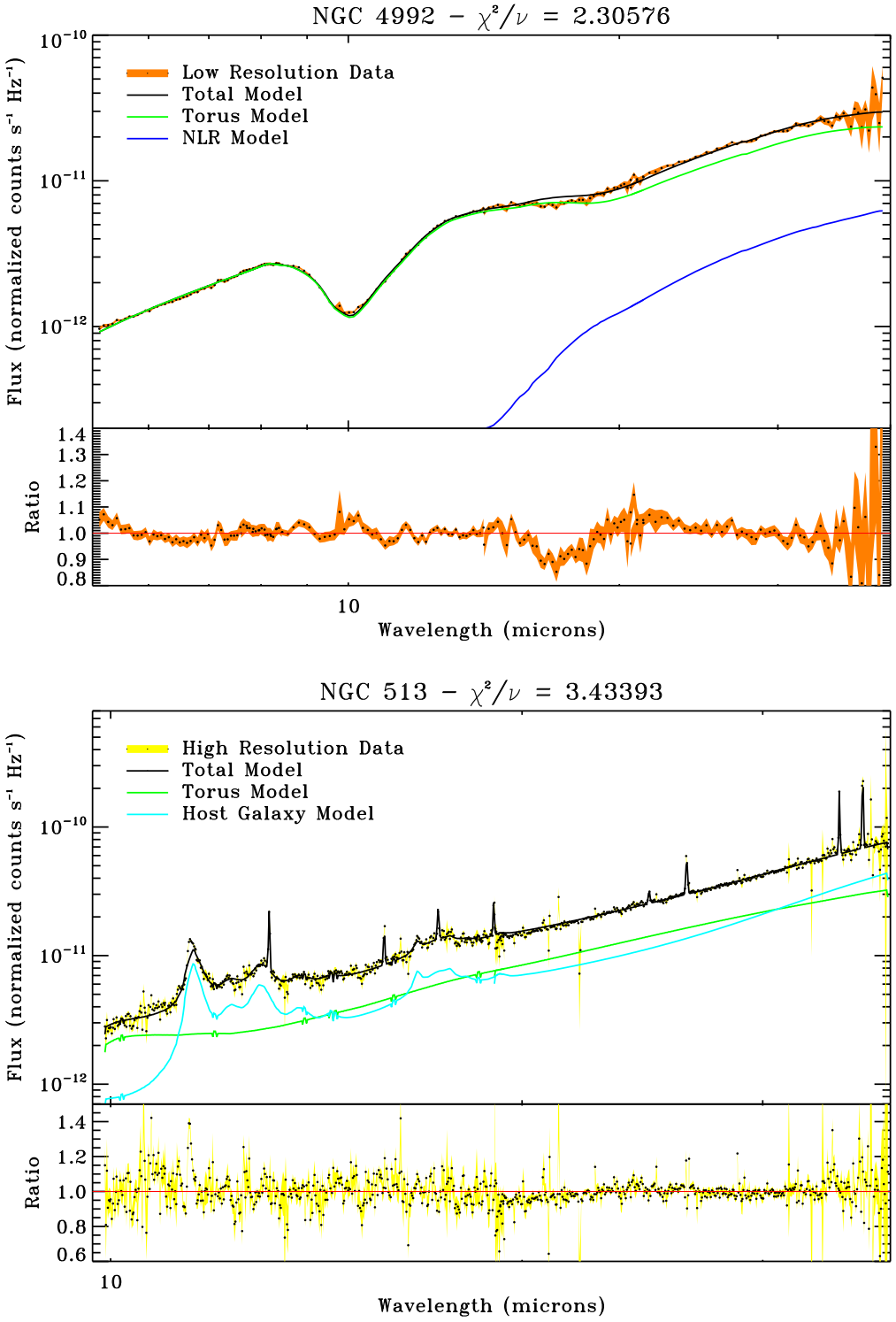

Figure 5.9: (continued)

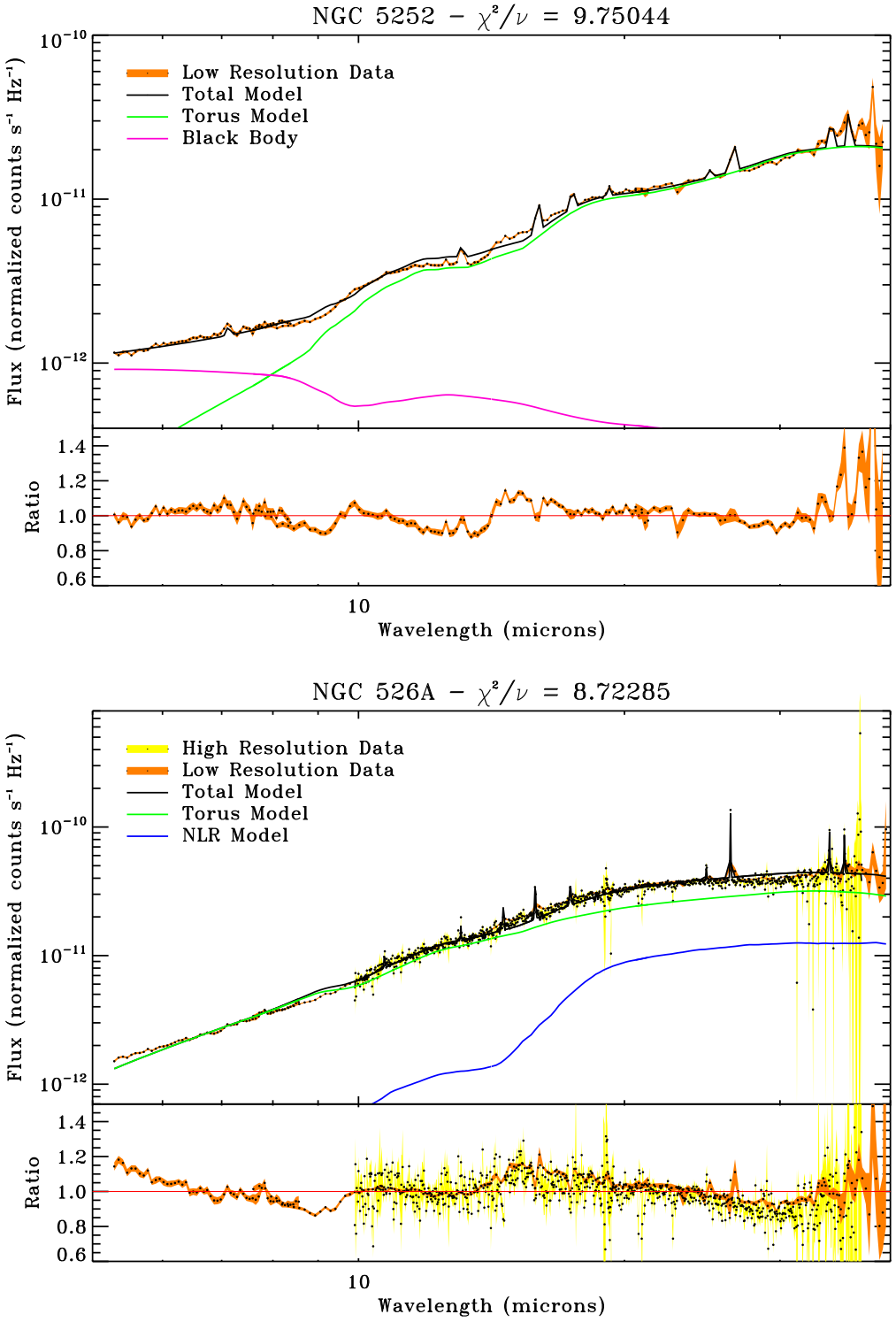

Figure 5.9: (continued)

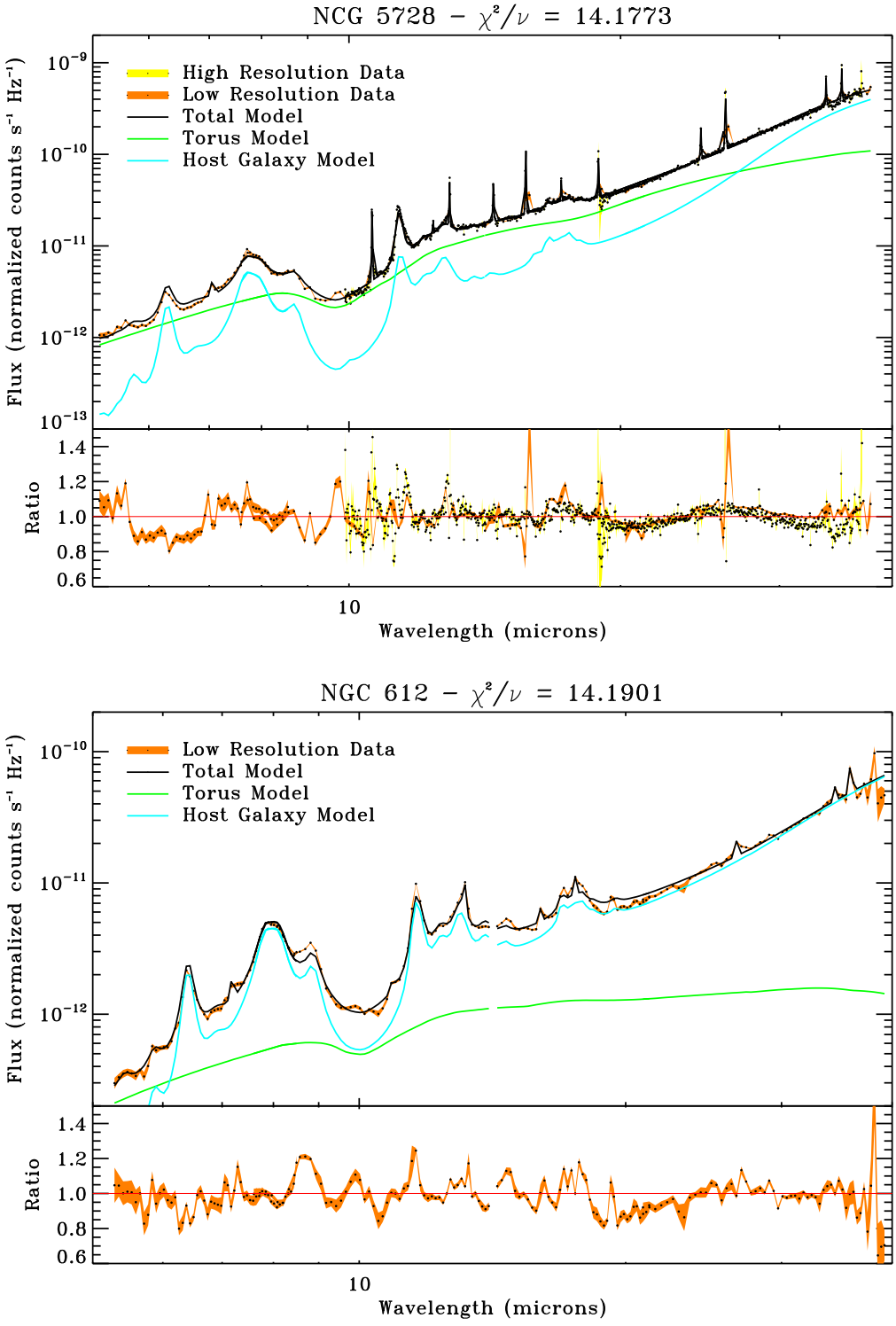

Figure 5.9: (continued)

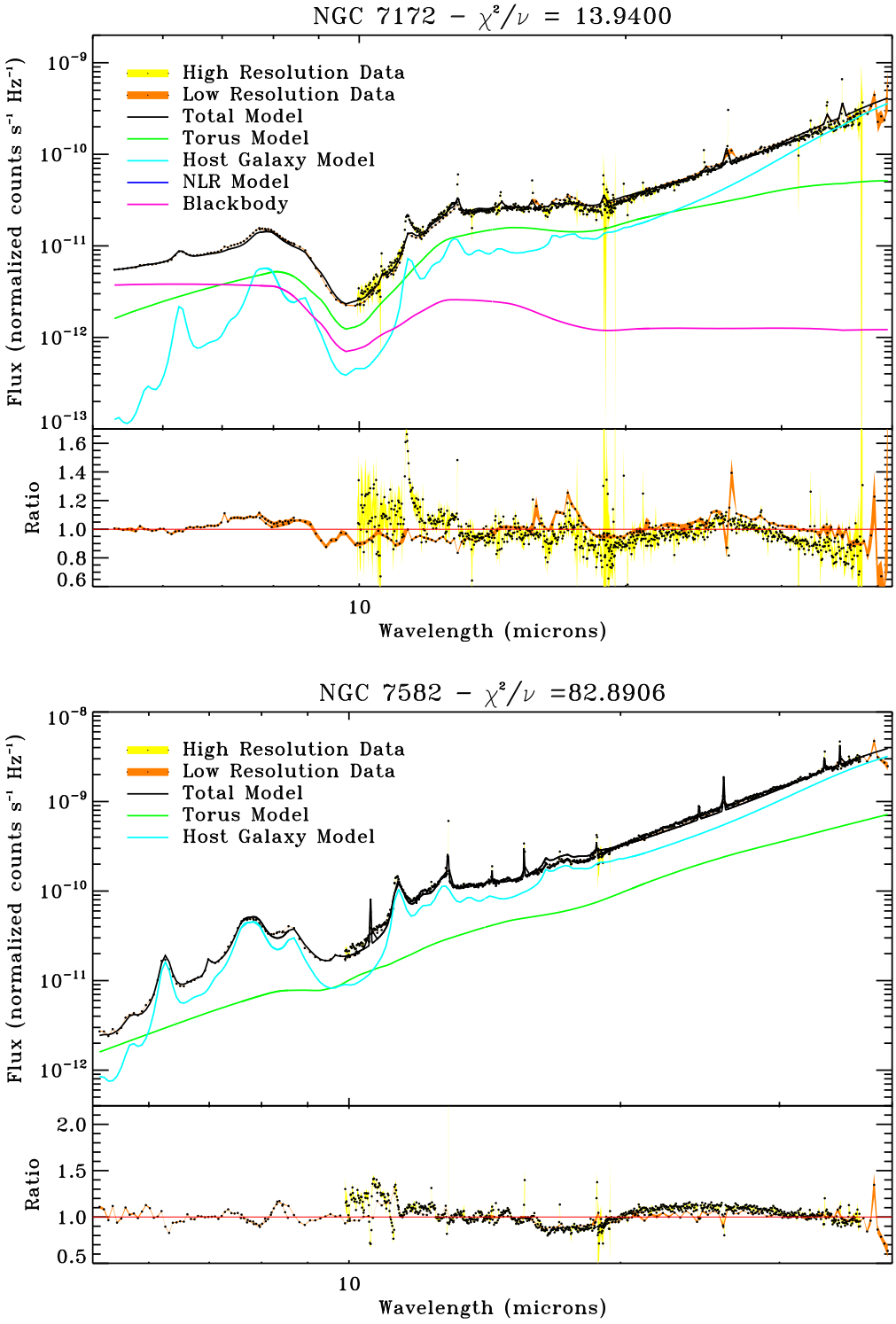

Figure 5.9: (continued)

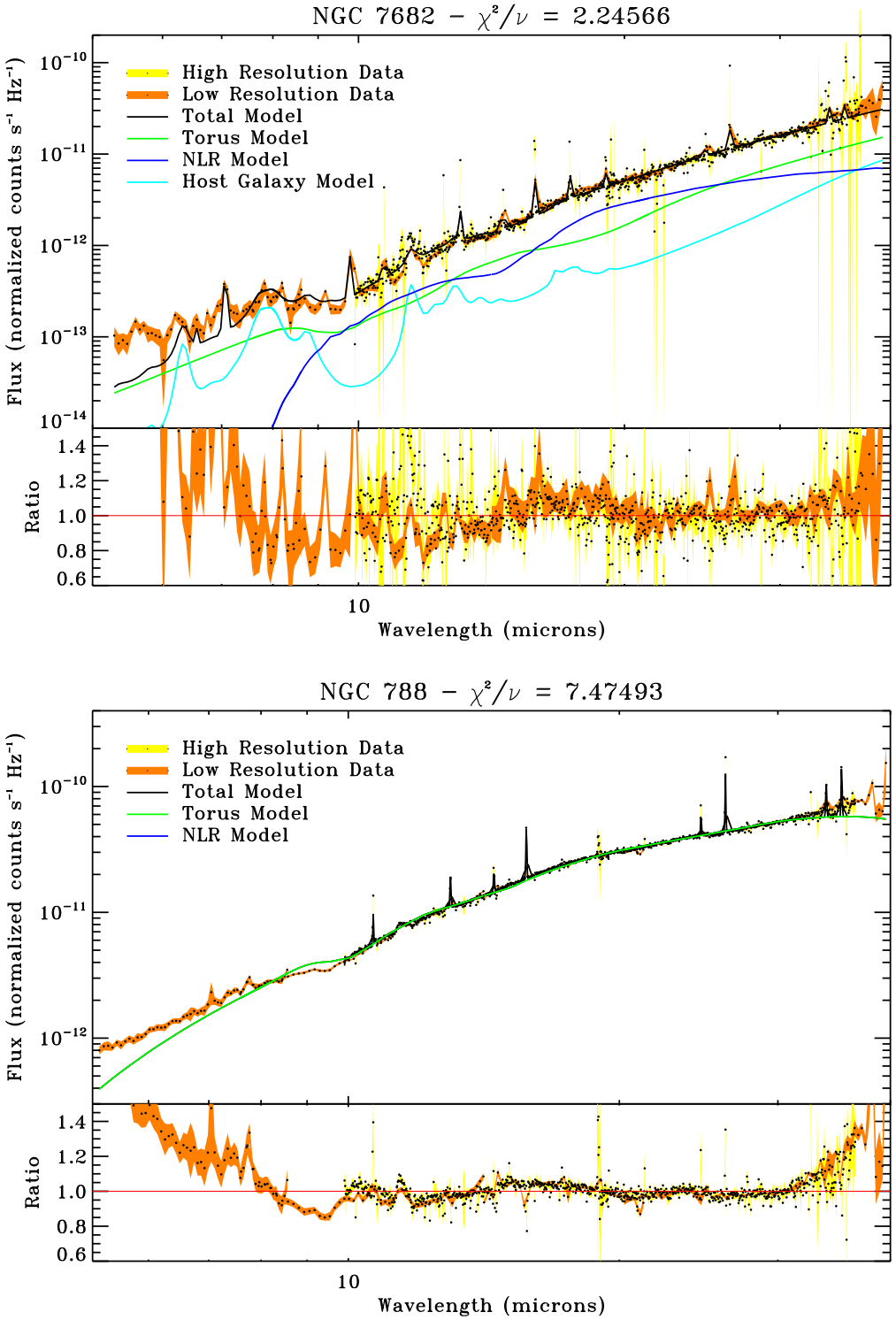

Figure 5.9: (continued)

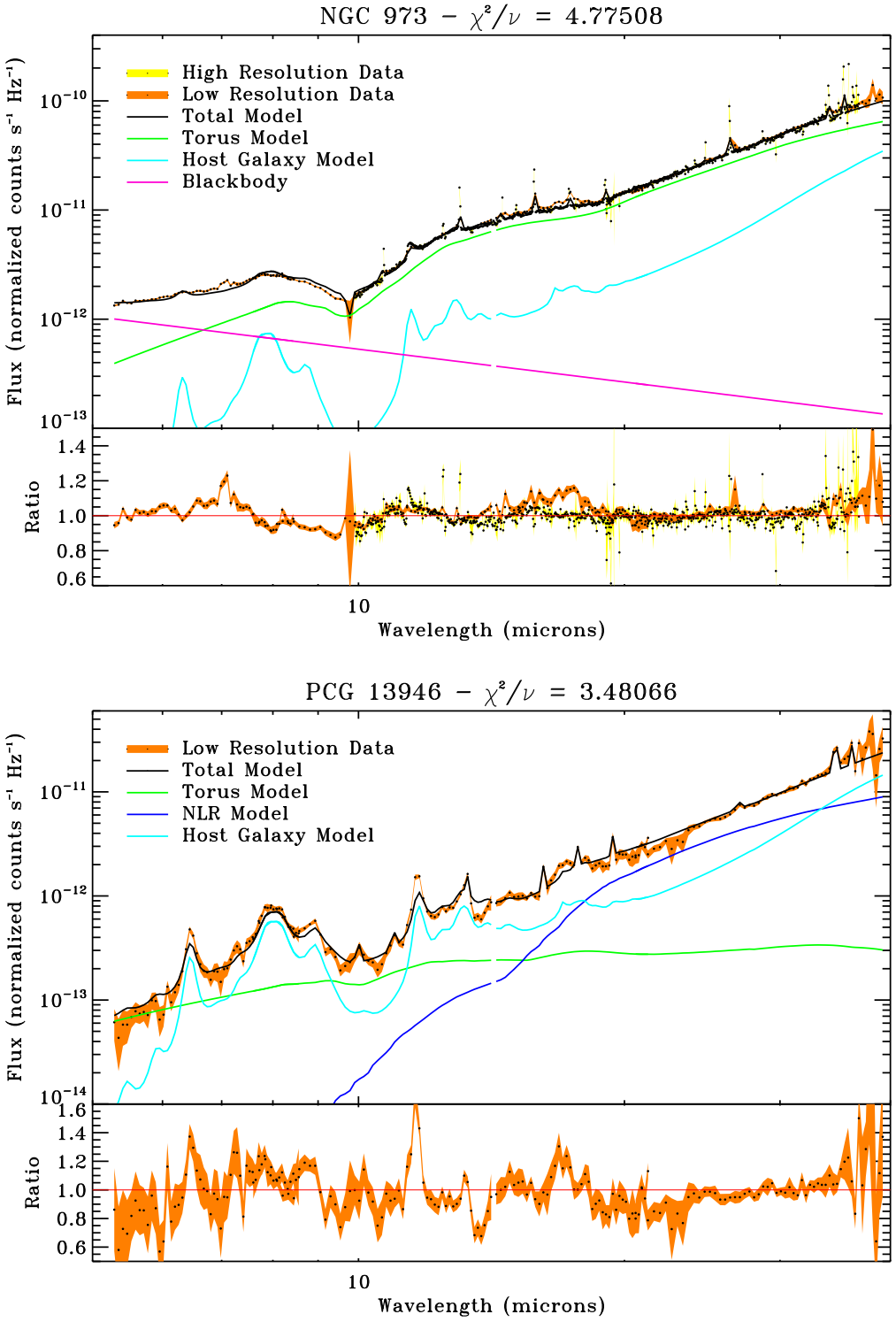

Figure 5.9: (continued)

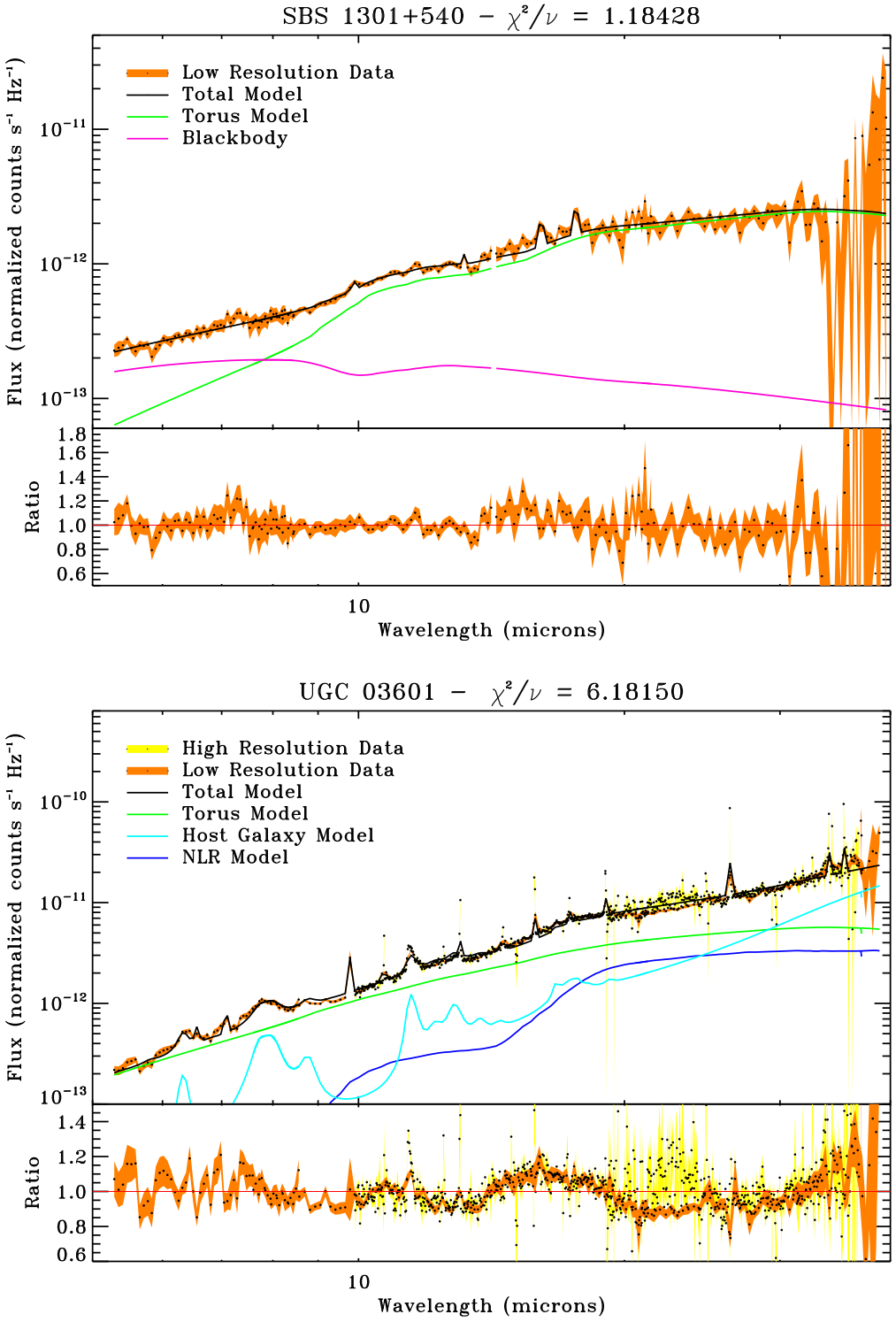

Figure 5.9: (continued)

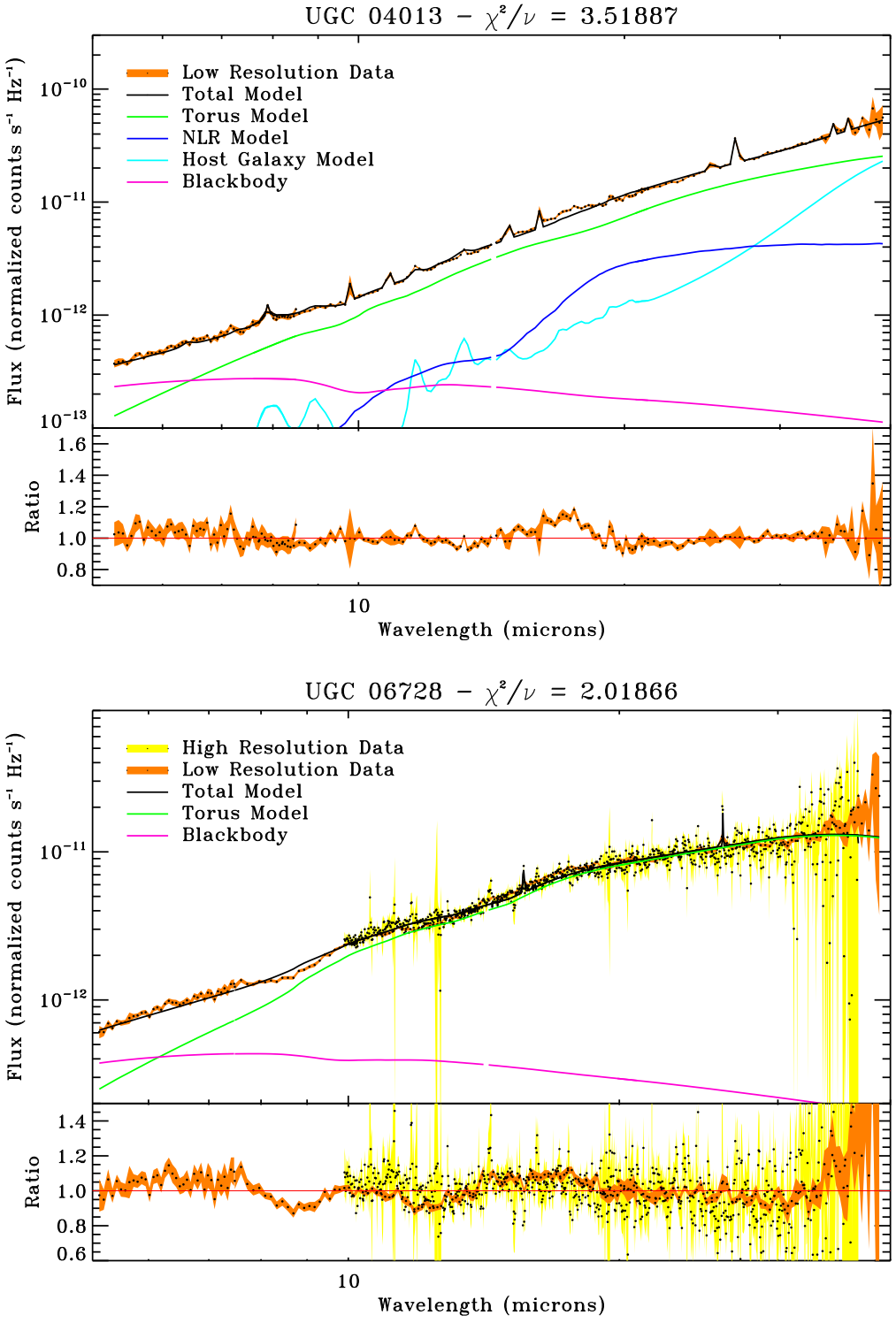

Figure 5.9: (continued)

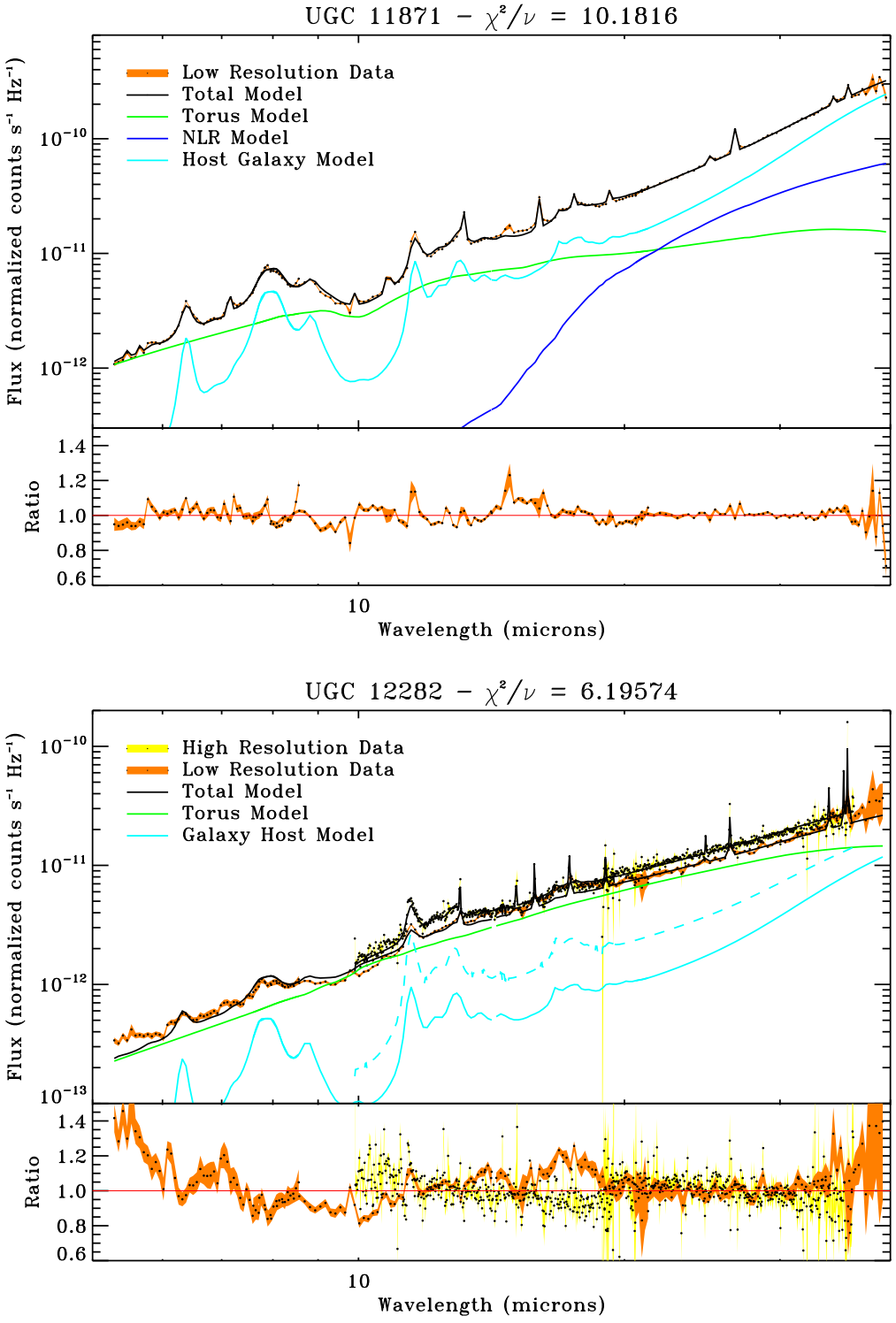

Figure 5.9: (continued)

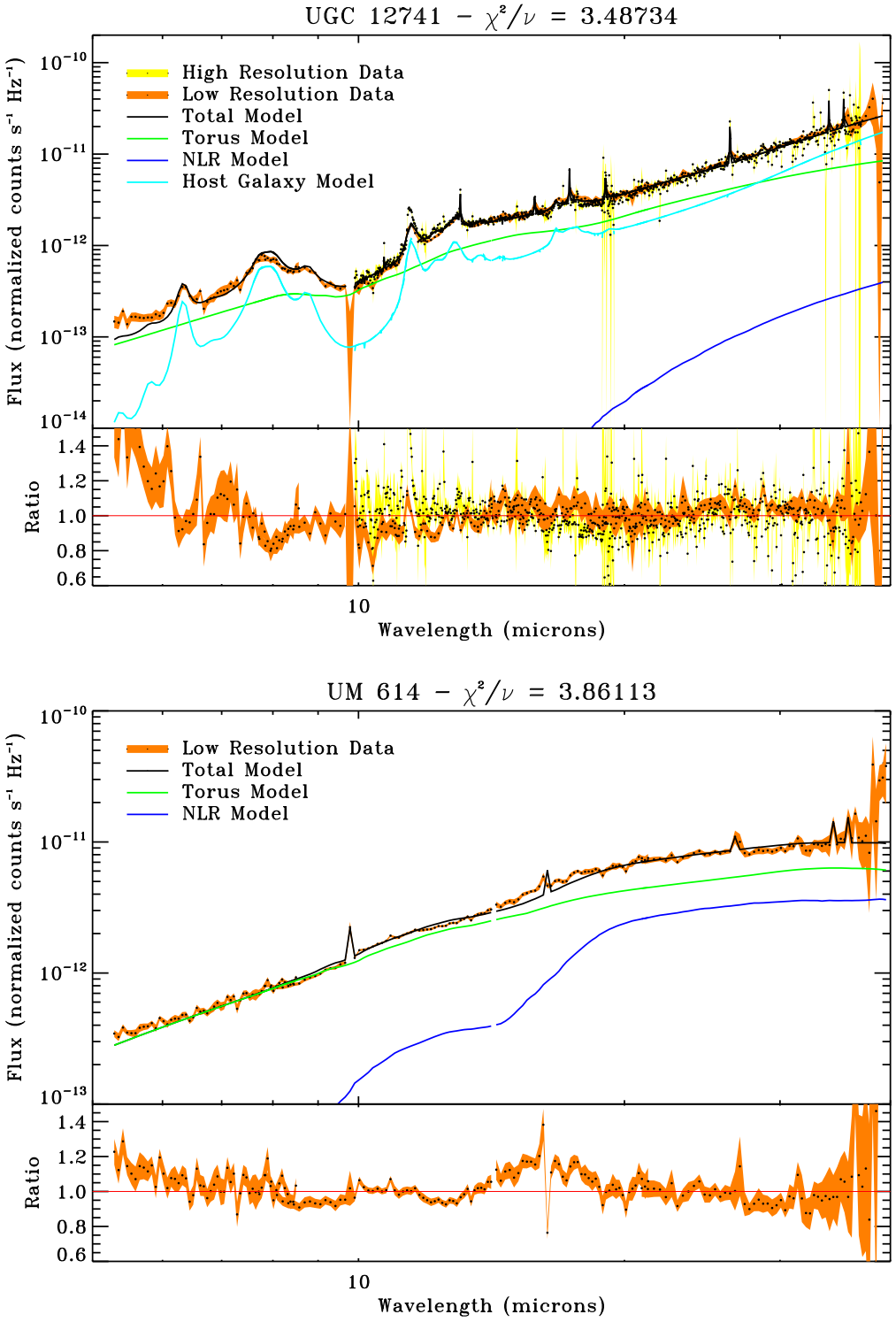

Figure 5.9: (continued)

Chapter 6

Results

6.1 Individual AGN and Best-fit Model Properties

In this Chapter, detailed fitting results are presented for the sample, discussing each object individually and then examining the properties of the sample as a whole.

Most of our AGN classifications are taken from NED and Tueller et al. (2008, 2010). Where multiple classes are given, or the origin of the classification is unknown, we use cited references or available optical spectra to make our own classifications. Frequently, we use the Veron-Cetty & Veron (2010) catalog to find literature with classifications that we cite directly. Our optical classifications are based on SDSS (Ahn et al., 2012) and 6DF Galaxy Survey (Jones et al., 2009, 2004, 6df) optical spectra.

For the Sy 1 subclass assignments, we use the Winkler (1992) Hβ/[O III]λ5007 line ratio criteria. To distinguish between Seyferts, HII galaxies, and LINERs, we use the same line ratio diagnostics as Winter et al. (2010, hereafter W10). These include the theoretical HII galaxy-AGN diagnostic of Kewley et al. (2001), the empirical HII galaxy-composite galaxy diagnostic of (Kauffmann et al., 2003), and the Seyfert-LINER empirical division of Kewley et al. (2006). Our classification strategy is similar to Tueller et al. (2008, 2010), but we believe several of their classifications are taken directly from NED data tables without strong evidence. Our process updates these classifications when we find compelling evidence that the type has been mislabeled.

We use optical images from NED to identify the morphology and orientation of the AGN host galaxies. A representative image of each AGN and it's host is shown in Figure 5.5. For each AGN description, we also list the model components used in addition to the torus with the following abbreviations: NLR, HG (host galaxy), BB (blackbody), and S (silicate absorption).

2MASX J05580206-3820043 Model = NLR, BB, S

This Sy 1.2 (Winkler, 1992) has no NED assigned galaxy morphology, but appears to be an oblique disk with strong bulge in poorly resolved optical images. Tueller et al. (2010) classify as a Sy 1 but do not provide references or spectral evidence. Soft X-ray ($2-10\,\mathrm{keV}$) observations show weak absorption with $N_H = 1.82^{+0.08}_{-0.07} \times 10^{22} cm^{-2}$ (Turner et al., 1996). The IR continuum is relatively featureless and smooth with minimal non-AGN silicate absorption ($\tau_{9.7\mu m} = 0.31$). The AGN emission is

luminous, entirely outshining the host galaxy IR emission. We use the blackbody and NLR models to account for short and long wavelength flux respectively, but both components are relatively faint. The model deviations from the data ($> 36\,\mu$m and near the $10\,\mu$m absorption trough) are relatively small.

2MASX J09043699+5536025 Model = HG, NLR, S

The host galaxy of this Sy 1 has no NED morphology. The AGN is modeled in the soft X-ray with almost no absorption ($N_H = 0.06^{+0.02}_{-0.03} \times 10^{22} cm^{-2}$, Winter et al., 2008). A strong bulge is visible in SDSS data, with asymmetric extended emission. It appears adjacent (< 15 arcsec) to another galaxy with no known radial velocity information but similar asymmetric emission indicative of a possible interaction. The IR continuum is relatively flat with weak PAH features and almost no $10\,\mu$m feature. Our best fit model reproduces this curvature with slight $10\,\mu$m torus emission (a result of the low torus density, $N_0 = 1.37$) countering the host-galaxy $10\,\mu$m absorption trough. Both of these features are subject to slight intervening silicate absorption ($\tau_{9.7\mu m} = 0.65$) near the average of our sample. The NLR component contributes significant fraction of the IR flux above $18\,\mu$m indicative of a large covering factor.

2MASX J09112999+4528060 Model = HG, BB, S

Another Sy 2 with no NED morphology, SDSS images depict an elongated disk within a bright elliptic halo. The Sy 2 classification is supported by a large column density ($N_H = 33.02^{+11.01}_{-12.76} \times 10^{22} cm^{-2}$, Winter et al., 2008). The low resolution Spitzer spectrum shows strong $10\,\mu$m absorption in both the AGN and host galaxy

emission. Our torus model inclination ($i = 75.9°$) causes strong 10 μm absorption which is compounded by moderate ($\tau_{9.7\mu m} = 0.90$) non-AGN absorption. Strong PAH features are well fit by a bright host galaxy model ($f_{host} = 41\%$). The relatively simple model captures all the major features after the addition of a weak blackbody component (2.4% of IR flux).

2MASX J19595975+6508547 Model = NLR, S

A BL Lac object is embedded in an elliptical galaxy in a relatively crowded field. As we would expect for a BL Lac object, X-ray absorption is minimal ($N_H = 0.07^{+0.04}_{-0.04} \times 10^{22} cm^{-2}$ Winter et al., 2009). The low-resolution spectrum is incredibly flat with only one emission line and no visible silicate absorption or emission. The lack of spectral features causes us to believe our model is one of many capable of reproducing the power-law spectrum. Although we can reproduce the data with a simple model, our torus inclination ($i = 40.1°$) implies we be doing so inaccurately.

ARK 120 Model = BB, S

A face-on spiral galaxy with faint well spaced arms (Sb) hosts this unabsorbed (Winter et al., 2009) Sy 1 object. The spectrum contains several gentle humps well fitted by the torus model. These humps are cause by torus silicate emission at 10 and 18 μm because of the low density and inclination ($N_0 = 2.77, i = 11.6°$) of our model. The short wavelength section of the model is poorly fit without the addition of the blackbody (20% of IR flux). Above 34 μm the model dips away from the data

indicating some low-temperature dust, likely in the host galaxy, is not modeled.

ARK 347 (NGC 4074) Model = NLR, BB, S

Although NED assigns the host galaxy of this Sy 2 an S0/peculiar morphology, SDSS images show an oblique disk with clear spiral arms (Sb). Winter et al. (2008) note strong soft X-ray absorption ($N_H = 30.0^{+8.8}_{-8.9} \times 10^{22} cm^{-2}$). The low-resolution IR spectrum reveals an incredibly flat continuum with a handful of emission lines. Subtle curvature at long wavelengths is well matched by our thick ($\sigma = 70.3$), low density ($N_0 = 1.98$), and intermediate inclination ($i = 35.1°$) torus model. Significant blackbody flux (13.4% of IR flux) is required to supplement the torus continuum. The model fit is improved with the inclusion of an NLR component subject to bright AGN flux ($\log(U) = -0.12$).

CGCG 041-020 Model = HG, S

This Sy 2 is classified by W10 but the galaxy morphology is omitted in NED. SDSS imagery reveals an oblique disk structure (Sa?) with a strong equatorial dust lane. The galaxy nucleus is only partially obscured due to the inclination. The modeled X-ray absorption of this AGN is moderate ($N_H = 10.8^{+0.7}_{-0.8} \times 10^{22} cm^{-2}$) for a Sy 2 (Winter et al., 2008). The IR spectrum reveals strong host galaxy emission (27% of total IR emission) with prominent PAH features ($q_{PAH} = 4.38\%$). Our silicate absorption model shows absorption below the average for our sample ($\tau_{9.7\mu m} = 0.52$) indicating the dust lane is likely not in the line-of-sight of the AGN. The AGN contribution is limited to the torus mode with strong silicate absorption, a ramification of the

high-inclination ($i = 66.2°$).

CGCG 118-036 Model = HG, NLR, S

This Sy 2 is located within an SDSS observed inclined spiral galaxy (Sa). No previous morphology has been assigned in NED. Featuring strong host galaxy PAH features ($q_{PAH} = 4.38\%$), the bright host galaxy model (40.3% of IR flux) is entirely modeled by diffuse gas ($\gamma = 0$). Our torus model is thick ($\sigma = 52.3°$), perhaps to accommodate the low inclination ($i = 29.0°$) of this obscured AGN.

CGCG 420-015 Model = NLR, S

HST imagery shows this Sy 2 is hosted by a nearly face on spiral galaxy (Sa) with faint tightly wound arms (Malkan et al., 1998). Its low-resolution spectrum is flat below 20 μm, then curves downward above. Above 34 μm the model overcompensates this curvature. The torus model captures this almost entirely with only a faint NLR model contribution. The NLR ionization parameter ($\log(U) = 0.24$) is larger than 90% of our NLR models indicating small NLR radius.

ESO 005-G004 Model = HG, S

NED describes the nearby ($z = 0.006228$) host galaxy of this Sy 2 as an edge-on spiral (Sb) with strong dust lanes. The activity classification is based on the weak absorption in the soft X-ray ($N_H = 5.58^{+0.16}_{-0.16} \times 10^{22} cm^{-2}$ Winter et al., 2009). In order to fit both high- and low-resolution data, our models must differ above 20 μm because the low-resolution, long-wavelength slit is oriented (randomly) down the length of the galaxy (Figure 6.1). The orientation results in a slightly different slope for the low-

resolution data because the extended slit incorporates significantly more host galaxy flux. The model fit is accomplished by allowing the host galaxy parameters to differ between modules. Host galaxy flux represents nearly half (47%) of the overall IR emission so it's accurate description is key for this AGN. The model fits the data well in the overlap region between the high- and low-resolution data, but deviates strongly in the low-resolution, low-wavelength region. This could be because the large number of data points in the high-resolution region dominates the attempt to minimize χ^2/ν leaving the low-resolution data poorly fit. We do not attempt to weight the data artificially to correct this problem in order to keep our model fitting standardized. The torus model exhibits strong 10 and 18 μm absorption, but the low inclination of the model ($i = 0°$) leads us to believe the strong silicate absorption component ($\tau_{9.7\mu m} = 1.26$) is inappropriately fitting AGN absorption. The complex host galaxy contribution may be diminishing our ability to fit the AGN continuum accurately.

ESO 121-IG028 Model = S

This galaxy is classified by NED as a barred disk with possible spiral arms (SB0/a). It hosts a Sy 2 in its nucleus but the soft X-ray absorption is moderate ($N_H = 16.19^{+12.60}_{-9.40} \times 10^{22} cm^{-2}$, Winter et al., 2009). The low-resolution spectrum is best fit with an absorbed ($\tau_{9.7\mu m} = 0.79$) torus model and a few emission lines. The torus model has a thin ($\sigma = 15.6°$) highly inclined ($i = 66.6°$) torus with very opaque individual clouds ($\tau_v = 74$).

ESO 140-G043 (Fairall 51) Model = HG, NLR, BB, S

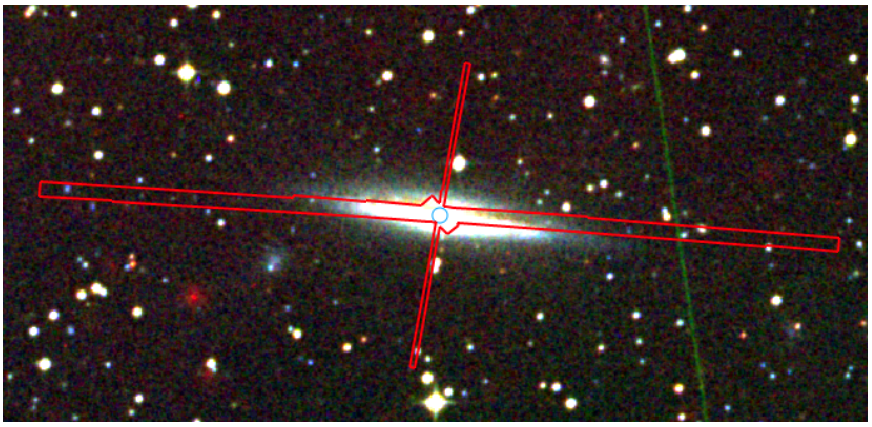

Figure 6.1: We project the location of the IRS slits for each module over an SDSS image of ESO 005-G004. By random chance, the long-wavelength, low-resolution slit is projected across the extended host galaxy. One summed slit region is given for each module for clarity.

Both NED and Bennert et al. (2006) describe the activity in this barred spiral (SBb) as Sy 1. The IR spectrum of this AGN is dominated by the clumpy torus model emission. This accounts for the relative flatness of the data. The torus model has a large radius ($Y = 46.9$) and a thick disk ($\sigma = 53.9°$). Some emission lines and PAH features are visible and well modeled despite the small host galaxy model flux contribution (4.8% of IR flux). Both NLR and blackbody components aid in fitting the flat spectrum. We note minimal non-AGN silicate absorption ($\tau_{9.7\mu m} = 0.25$). Above $\sim 35\,\mu$m the data deviates from the model implying we are failing to fit some portion of cool galaxy dust.

ESO 141-G055 Model = NLR, S

NED and Tueller et al. (2010) label this object as a Sy 1 without listing classification techniques or references. We use the Sy 1.2 optical spectrum classification of

Winkler (1992). The host galaxy is a spiral (Sc?) with a large nucleus. Our torus model is radially extended ($Y = 46.9$) and thick ($\sigma = 53.9°$) with a low inclination angle ($i = 13.25°$). Despite the low flux errors, the data are relatively well fit with a moderately absorbed ($\tau_{9.7\mu m} = 0.62$) torus and NLR model. Below $10\,\mu$m, some small deviations are observed but they never exceed 15% of the model flux.

ESO 157-G023 Model = BB

A Sy 2 is at the core of this barred spiral galaxy (SBbc). Several bright sources are either projected or a part of the spiral arms of this galaxy. We model the low-resolution IR spectrum with just torus and blackbody components. The torus model has the most opaque clouds of our sample ($\tau_v = 94.4$) and is viewed at a highly inclined angle ($i = 79.9°$). Only three weak emission lines are visible. The only poorly modeled feature of the spectrum is a hump at $\sim 17\,\mu$m.

ESO 198-024 Model = S

An elliptical galaxy hosts this Sy 1. Porquet et al. (2004) report no intrinsic $2-10\,$keV absorption. The IR emission is well modeled with only a torus component and a few emission lines. Our torus model is thin ($\sigma = 29.3$), has a small outer radius ($Y = 15.5$), and intermediate inclination angle ($i = 53.8°$). The spectrum is relatively flat with two small characteristic humps similar to those in ESO 141-G043 and ARK 120. A small amount of silicate absorption is observed ($\tau_{9.7\,\mu m} = 0.24$).

ESO 297-G018 Model = HG, S

Tueller et al. (2008) label the AGN at the center of this edge-on spiral (Sa) as a

Sy 2. The IR spectral emission is dominated by the torus component with a small host galaxy contribution (17.8% of IR flux) to fit the PAH features ($q_{PAH} = 3.89$). A thin disk ($\sigma = 26.0°$) is matched with a high inclination ($i = 56.5°$) observation angle to model this significantly soft X-ray obscured AGN ($N_H = 41.71^{+4.70}_{-2.90} \times 10^{22} cm^{-2}$, Winter et al., 2008). Despite a poor fit to the 11.3 μm PAH feature, the data are accurately reproduced with the model.

ESO 323-077 Model = HG, NLR, BB, S

This Sy 1.2 is hosted by a barred disk galaxy ($SB0^0$) with several foreground stars and distant galaxies within 1 arcminute. The IR spectrum is modeled using all the models considered but we fail to reproduce the exact PAH feature flux. We suspect that our host galaxy model is not normalizing correctly because it is overestimating the amount of low temperature gas. Our model supports the intermediate classification as the line-of-sight is very near the edge of the torus ($i = 37.8°, \sigma = 42.0°$). This results in an accurate fit throughout the continuum, but we cannot perfectly reproduce the prominent PAH features.

ESO 374-G044 Model = NLR, S

The inclined barred spiral (SBab) contains a Sy 2 according to Tueller et al. (2010) which we confirm with examination of the 3df optical spectra. The steep IR low-resolution spectrum for this AGN is modeled with a torus and NLR. Despite the slight deviations from the data at either end of the spectrum, our best-fit model matches the data well with a moderately thick torus ($\sigma = 44.8°$) which we view

edge-on ($i = 72°$). The model is very slightly absorbed ($\tau_{9.7\,\mu m} = 0.19$).

ESO 417-G006 Model = BB, S

A Sy 2 occupies the nucleus of this disk galaxy (SA0/a). The relatively simple IR spectrum is well fitted by a flat torus model with a low-resolution blackbody component. Many prominent emission lines are also modeled. The model torus is radially extended to the hard limit ($Y = 60$) and viewed from a high angle ($i = 80.0°$). The spectrum is very well fit showing only slight deviations at the the lowest wavelengths.

ESO 426-G002 Model = S

This barred spiral galaxy with a large outer ring ((R')SB0/a) contains a Sy 2 (Parisi et al., 2012; Tueller et al., 2010). The best-fit model is incredibly smooth with only a few emission lines deviating from the torus component. The data are very well fit everywhere but at long wavelength edge of the LL1 module where Spitzer IRS begins to fail.

ESO 506-G027 Model = HG, S

This large nucleus, edge on disk galaxy ($S0^+$) contains a Sy 2. The low-resolution spectrum is very well fit despite the incredibly small errors of the data. The continuum is relatively smooth with very strong silicate absorption ($\tau_{9.7\,\mu m} = 1.45$) as we expect given the host galaxy orientation. The soft X-ray flux is also very strongly absorbed ($N_H = 76.82^{+7.37}_{-6.79} \times 10^{22} cm^{-2}$, Winter et al., 2008). A host galaxy model is added to the torus model in order to fit the cool long wavelength regime. The resulting host

galaxy model is pure diffuse gas ($\gamma = 0$) and represents only 6% of the model flux. No PAH features are visible.

ESO 511-G030 Model = BB, S

The host of this Sy 1 is a nearly face-on spiral galaxy with strong spiral arms (SAc) extending several arcminutes. We model this low-resolution IR spectrum with a torus component supplemented with a bright short wavelength blackbody which contributes 32% of the IR flux. The data are smooth with a familiar two hump shape (e.g., ARK 120) that our model fails to perfectly reproduce. Our torus model is significantly inclined ($i = 67°$) but with a very low density ($N_0 = 1.43$).

ESO 548-G081 Model = NLR, BB, S

The host galaxy of this Sy 1 is a tightly wound barred spiral (SBa) with a bright nearby (< 1 arcmin from center) foreground star. It exhibits no soft X-ray absorption (Winter et al., 2009). The flat low-resolution spectrum has two small humps and two clear emission lines. The best fit model consists of torus, NLR, and blackbody components. Most of the data are very well modeled with the exception of the long wavelength ($> 33\,\mu$m) regime. The torus model is quite thin ($\sigma = 30.4°$) and viewed nearly face-on ($i = 11.29°$).

ESO 549-G049 Model = HG, NLR, S

This object has been classified both as a Sy 1(Véron-Cetty & Véron, 2006) and Sy2/Liner Tueller et al. (2008). We use the cited Sy 1 result. The host galaxy morphology appears to be spiral with a very bright and large nucleus (Sb). The IR

spectral model suggests that the host galaxy dominates the IR emission (62% of total flux). The NLR model emission is prominent and results in a covering factor of 28%, the highest of our sample. The PAH features are well fit, yet several artifacts remain in the model/data ratio plot. These contribute to the poor fit statistics along with the small errors of the data.

IC 1816 Model = HG, NLR, BB, S

The cited NED classifications call this galaxy a Seyfert 2 (de Grijp et al., 1992; Winkler, 1992) which we use. The host galaxy is a nearly face-on, disturbed/peculiar spiral (Malkan et al., 1998, SBa/b). The IR spectra is relatively flat with obvious PAH features, many emission lines, and slight 10 μm absorption. Our four-component model fits wonderfully excepting a small deviation below the data at short wavelengths ($< 7\,\mu$m). High and low resolution models are slightly mismatched near 18 μm, but we consider the difference too small to necessitate a separate model.

IRAS 05218-1212 Model = NLR, BB, S

Osterbrock & De Robertis (1985) classify this AGN as a Sy 1.5, which we use, in contrast to the uncited NED and Tueller et al. (2010) identification (Sy 1). The morphology of the host galaxy is unclear, it could be either elliptical or a disk galaxy (S0). Our best fit model is dominated by torus emission with contributions from both NLR and blackbody components. The model fits the smooth, gently curving data well; it only deviates strongly at the longest wavelengths ($> 35\,\mu$m).

LEDA 088639 (2MASX J11454045-1827149) Model = NLR, BB

Winkler (1992) classify this object as a Sy 1.5 which we confirm with measurements from 6df optical spectra. Malkan et al. (1998) use HST WFPC 2 images to describe the host galaxy as quasar-like and irregular with filaments and wisps. Winter et al. (2008) note no soft X-ray absorption. The Spitzer spectrum is gently curved with a few weak emission lines. The best-fit model consists of torus, NLR, and blackbody components with no 10 μm absorption. Our model deviates slightly ($< 10\%$) near a small 18 μm undulation.

LEDA 089420 (LCRS B232242.2-384320) Model = HG

A Sy 1 is embedded in this S0 galaxy that emits half (49%) of the emission of our low resolution IR spectrum model. Our model consists of only host galaxy and torus components and matches the data well over the entire spectrum.

LEDA 178130 (2MASX J05054575-02351139) Model = BB, S

The morphology of this Sy 2 is unknown as it has not yet been imaged at high resolution. The low-resolution IRS spectrum is a smooth curve with slight 10 μm absorption. A torus and blackbody with a few weak emission lines fit the data convincingly. The fact that the torus dominates the IR emission is consistent with the Seyfert 2 classification and absorption. In the X-ray, this galaxy shows absorption in the amount of $N_H = 6.57^{+3.03}_{-2.39} \times 10^{22} cm^{-2}$(Winter et al., 2009).

MCG -01-13-025 Model = BB, S

A Sy 1.2 is contained within a slightly inclined disk galaxy with a hint of a bar (SAB0$^+$). The soft X-ray emission is unabsorbed (Winter et al., 2009). The torus and

blackbody model describes well the double humped, relatively smooth IR spectrum. A strong emission line ([S IV] 10 μm) is inadvertently subtracted from the low-resolution data in one of the observations. This is accounted for in the fit, with both modeling and large error bars (because it is only present in one of the observations). The high-resolution long wavelength module is especially noisy in this spectrum.

MCG -01-24-12 Model = HG, NLR, S

The Sy 2 within this partially barred, oblique spiral (SABc) shows strong [O III] 5007 Å emission with two distinct nuclear emission regions (Schmitt et al., 2003). Winter et al. (2009) find significant X-ray absorption ($N_H = 11.45^{+2.82}_{-2.27} \times 10^{22} cm^{-2}$). Our IR model reflects this strong NLR emission but is still dominated by torus flux. We also incorporate a small (6% of total flux) host galaxy component. The model fits the data well at long wavelengths but drifts away below 7.5 μm.

MCG -02-12-050 Model = NLR, S

Optical spectra taken with 6dF reveal the activity of this nearly face-on spiral galaxy (SBab) can be classified as Sy 1.2. Moran et al. (1996) label MCG -02-12-050 a Sy 1, but do not distinguish between type 1 and type 1.2. The Spitzer low-resolution spectrum is nearly flat and is well modeled with torus and NLR components. Slight deviation from the data occurs above 35 μm.

MCG -03-34-064 Model = HG, NLR, S

Following 6df spectral analysis, we classify this S0/a galaxy as a Sy 1.8 echoing the Tueller et al. (2008) finding. This is supported by strong X-ray (2-10 keV) absorption

($N_H = 40.73^{+4.79}_{-4.30} \times 10^{22} cm^{-2}$, Winter et al., 2009). The error bars on the IRS data are very small for this observation (average error is 1.1% of flux), but our three-component model reasonably fits the nearly flat IR spectrum. The datas average deviation from the model is under 5% of the flux, with 95% of the data points within 12% of the model flux. Our model does not perfectly match subtle curves in the data, especially in the low-resolution low-wavelength regime.

MCG +04-22-042 (CGCG 121-075) Model = NLR, BB

We use SDSS images to classify the morphology of this oblique barred spiral (SBa). The IR spectrum of this Sy 1.2 is best fit with torus, NLR, and blackbody components. The AGN shows no X-ray absorption (Winter et al., 2008). We see slight curvature differences between the high and low resolution data sets around 12 μm, but a single model fits both reasonably well.

MCG -05-23-016 (ESO 434-G040) Model = NLR, BB, S

Although this galaxy is classified as a Sy 2, its IR spectrum reveals a broad Paβ 1.28 μm line indicative that the torus IR optical depth is small (Goodrich et al., 1994). X-ray absorption is similarly small ($N_H = 1.60^{+0.01}_{-0.01} \times 10^{22} cm^{-2}$, Turner et al., 1997). Optical images show an inclined disk galaxy (S0) with a bright, unresolved object adjacent ($<$ 15 arcseconds away). The IR spectrum is smooth with slight silicate absorption. Dominated by the torus model, the blackbody and NLR flux contribution to the model flux is small. The data deviate from the model mildly in the low-resolution regime.

MRK 18 (UGC 04730) Model = HG, NLR, BB, S

NED and Tueller et al. (2008) have no classification for this AGN. W10 analyze both an SDSS spectrum and their own 2.1m Kitt Peak National Observatory (KPNO) optical spectrum. Emission line diagnostic plots combined with both theoretical and empirical boundaries come to no consensus regarding its classification. The SDSS emission line ratios imply H II-like emission whereas KPNO emission lines point to H II, LINER, and composite (H II and AGN) emission. Additionally, W10 note a broad component to Hα of approximately 370 km s^{-1}. Parisi et al. (2009) use independent optical spectra to classify MRK 18 as a Sy 2. The X-ray absorption is also significant ($N_H = 18.25^{+3.64}_{-2.71} \times 10^{22} cm^{-2}$, Winter et al., 2008).

In light of the confusing optical spectra, our activity classification remains unknown. The host is either an inclined disk or very elliptical galaxy (S0 or E) based on SDDS imagery. The IR spectrum is host galaxy dominated (69% of model flux) with strong PAH features. The torus and NLR flux are difficult to constrain because of the luminous host galaxy. Our model components are relatively insensitive to changes in several parameters (e.g., inclination) resulting in several parameters best fit at the hard limits (e.g., i, q, τ_v, Y).

MRK 50 Model = S

This object is classified as both a Sy 1 (Khachikian & Weedman, 1974) and a Sy 1.2 (Sargent, 1970). We use the Winkler (1992) Hβ/[O III]λ5007 line ratio criteria with SDSS measured emission lines to determine the type is a Sy 1, agreeing with

the Tueller et al. (2010) assessment. The host galaxy is an inclined S0 galaxy visible in SDSS images. A torus model with a single emission line fits the flat low-resolution IR spectrum very well.

MRK 352 Model = BB

This Sy 1 has a nearly face-on, disk (SA0) host galaxy. The IR spectrum is relatively noisy with large errors in the high-resolution (especially LH) module data. The flat spectrum has two humps, and is fit very well by a combination torus and blackbody model.

MRK 417 Model = NLR, BB, S

This elliptical galaxy has Sy 2 emission lines. Our best-fit model for the low-resolution IR model consists of torus, NLR, and blackbody components. We fail to fit some subtle aspects of its curvature, especially near $18\,\mu$m.

MRK 501 Model = NLR, BB, S

The BL Lac object is within a galaxy morphologically classified as an elliptical. The galaxy features a radio core jet with components that have apparent motion of $0.2 \pm 0.1 \times c$ (Kellerman et al. 2004). The IR spectrum is almost completely flat, so much so that a power law fits the data with $\chi^2/\nu = 1.88$. We instead fit the data with torus, NLR, and blackbody components with meaningful fit parameters and get an even better fit quality.

MRK 915 Model = NLR, S

This galaxy has been classified as a Sy 1 (Tueller et al., 2010, NED), a Sy 1.5

(Bennert et al., 2006), and a Sy 1.8 (Dahari & De Robertis, 1988). We use the Sy 1.5 classification; it is the most recent referenced optical spectrum. Malkan et al. (1998) use HST to describe the morphology as disturbed spiral galaxy (Sa) with filaments and a prominent dust lane partially covering the nucleus. We fit the flat low-resolution IR spectrum easily with a torus and NLR model. The long-wavelength ($> 35\,\mu$m) end of the spectrum has the most poorly fit data.

NGC 4102 Model = HG, NLR, BB

This galaxy is a well-studied LINER with a slightly inclined spiral morphology (Sb). The single spiral arm is thick and lined with dust on the inside edge. We find that our IR model is dominated by the host galaxy component below $20\,\mu$m (66% of model flux). The torus component of the model shows very strong silicate absorption and dominates the long-wavelength spectrum. NLR and blackbody components help to match the data shape, but have a small overall flux contribution. The large fit statistic is more a reflection of the 1.1% flux error than the average 4.6% deviation of the model from the data.

NGC 4388 Model = HG, NLR, BB, S

This is an edge-on spiral galaxy (SAb) with massive dust lanes obscuring the galaxy bulge. NED lists multiple AGN activity classifications, so we use the most recent optical observation (W10) that labels this a Sy 2. The mildly absorbed IR spectrum fits the data well using torus, NLR, blackbody, and host galaxy components.

NGC 4395 Model = HG, NLR, BB

The modeling of this underluminous Sy 1 within a bulgeless dwarf host is described in great detail in Chapter 4. The fit requires all our model components, along with a varying torus and host galaxy contribution between high- and low-resolution modules. The model describes the data well across the spectrum (Section 4.8).

NGC 454 Model = HG, S

This strongly interacting galaxy pair consists of a red elliptical galaxy (NGC 454) and a starbursting, knotty, irregular galaxy (NGC 454 NED01/ESO 141-IG036). There is no NED activity classification for these objects. Although initially presumed inactive because of a lack of high excitation lines, the Johansson (1988) optical spectrum shows large [O III] λ5007/Hα and [O III] λ5007/Hβ ratios (> 1 and 3 respectively) and large line widths ($> 300\,\mathrm{km\,s^{-1}}$) indicating NGC 454 is likely a Sy2. The torus component of the IR spectrum model dominates the host galaxy component (5% of the model flux). The mildly silicate absorbed spectrum is well fitted by the model.

NGC 4686 Model = HG, NLR, BB

Tueller et al. (2010) use KPNO spectra to show this is an X-ray bright, optically normal galaxy (XBONG). The oblique spiral (Sa) host galaxy contributes weak PAH features to our IR spectrum model. The flat spectrum is fit primarily with our torus model with contributions at either end by NLR and blackbody components. The total model approximates the data well.

NGC 4992 Model = NLR, S

The XBONG/Sy 2 label given this spiral galaxy (Sa) by NED and echoed by Tueller et al. (2010). To Masetti et al. (2006), optical spectra appear entirely galactic in nature. In contrast, W10 classify the object as a LINER using SDSS emission line diagnostics. We use the W10 result. The low-resolution IR spectrum contains no prominent emission lines and is well-modeled using only torus and NLR components.

NGC 513 Model = HG

A spiral galaxy (Sb/c) assigned Sy2 classification in Tueller et al. (2010), this AGN features broad polarized Balmer lines (Tran, 2001) thought to be indicative of a hidden broad line region. We stick with convention maintaining this is a Sy 2 galaxy. The IR spectrum is limited to only high-resolution data limiting the spectral coverage at the low-wavelength end. Our data is best-fit with a torus and host galaxy component featuring several strong emission lines.

NGC 5252 Model = BB, S

This edge-on S0 galaxy was originally labeled as a Sy 1.9 (Osterbrock & Martel, 1993). Goncalves et al. (1998) detect a broad Hα component with higher resolution spectroscopy several years later, and identify nuclear LINER emission and Sy 2 emission in two neighboring knots (< 0.37" away). We assign the object a Sy 2 for analysis. The low-resolution data is adequately fit with a torus and blackbody model. The data itself is relatively smooth with two weak humps.

NGC 526A Model = NLR, S

This merging galaxy (S0/E) has an irregular band of dust extending out from the

nucleus (Malkan et al., 1998). Winkler (1992) and Bennert et al. (2006) label it a Sy 1.9 which we use. Our own 6df analysis confirms the Sy 1.9 designation. The IR spectrum appears to be a broken power-law (split at 19 μm) that our torus and NLR model fits reasonably well. Some slope mismatch occurs below 10 μm in the low-resolution only regime.

NGC 5728 Model = HG, S

Pecontal et al. (1990) note a broad line region in a spectrum that isolates the central region emission. We verify this using 6df data and call this object a Sy 1.9. The host galaxy is a barred spiral with low surface brightness outer arms (SAB(r)a). We combine a strong host galaxy component with a torus in order to model this IR spectrum. The fit is quite good everywhere but around the PAH feature at 6.4 μm.

NGC 612 Model = HG, S

With a confusing morphology, this galaxy has been labeled as an S0/a, a dusty elliptical, and in the radio, a hybrid of FR I and FR II. Tueller et al. (2008) classify it as a radio galaxy. Using line ratios from Lewis et al. (2003) and employing all the line diagnostics used by W10 we conclude the emission is definitively a Sy 2. X-ray absorption supports this with $N_H = 129.7^{+12.9}_{-8.3} \times 10^{22} cm^{-2}$, the most X-ray absorbed object in our sample (Winter et al., 2008). The host galaxy component of our low-resolution IR model dominates with 80% of the total model flux. Interesting, the silicate absorption optical depth ($\tau_{9.7\mu m} = 0.78$) is near the average for our sample, meaning all absorption is attributed to the dense ($N_0 = 6.53$) nearly edge-on ($i =$

84.1°) torus model. The resulting small contribution of the torus model does not allow for strong parameter constraints. The overall model fits the data decently, but there are a few instances where the PAH features were not exactly matched.

NGC 7172 Model = HG, BB, S

The dust lane adjacent to the nucleus of this Sy 2 has led it to be classified morphologically as an edge-on spiral galaxy (Sa). The IR spectrum shows the most 10 μm silicate absorption of our sample ($\tau_{9.7\mu m} = 2.14$). Despite this, the soft X-ray absorption is moderate (Turner et al., 1997, $N_H = 8.19^{+3.42}_{-3.30} \times 10^{22} cm^{-2}$). Although all the PAH features of the host galaxy are not perfectly modeled, the model fits the data very well. There are substantial contributions to model flux from the host galaxy, torus, and blackbody model components.

NGC 7582 Model = HG, S

NGC 7582 has a well-studied morphology; the edge-on spiral galaxy (SBab) has an optically obscured nucleus and a large dust lane crossing the nuclear region. The X-ray spectrum is absorbed (Turner et al., 1997, $N_H = 8.19^{+3.42}_{-3.30} \times 10^{22} cm^{-2}$). The galaxy hosts a Sy 2 with broad Paschen lines in the IR (Reunanen et al., 2003). The best-fit IR model for this AGN combines a host galaxy (73% of total flux) and a torus component with notable silicate absorption ($\tau_{9.7\mu m} = 0.84$). The poor statistical fit can be blamed on the 2.0% average error; the mean model displacement ($< 8\%$) is good.

NGC 7682 Model = HG, NLR, S

This face-on SBab galaxy is a member of a pair, confirmed with radial velocity measurements. It hosts a Sy 2 with a hidden polarized broad line region (Tran, 2001). Our IR spectrum model consists of torus, NLR, and host galaxy components each contributing similar flux. The model fits well above 8 μm, but fails at shorter wavelengths.

NGC 788 Model = S

A tightly wound nearly face-on spiral with an intense bulge (SA0), NGC 788 hosts a Sy 2 with broad polarized Balmer lines indicative of a hidden BLR (Kay & Moran, 1998). Substantial X-ray absorption ($N_H = 46.82^{+4.68}_{-4.47} \times 10^{22} cm^{-2}$) was observed by Winter et al. (2009). The IR spectrum is decently modeled using just torus and blackbody components. Below 7 μm and above 33 μm, the model does not produce enough flux to match the data.

NGC 973 Model = HG, BB, S

NGC 973 is an edge on Sb galaxy. Its activity was discovered by Swift and Integral and is classified as a Sy 2 by Burenin et al. (2008). Our model included torus, host galaxy, and blackbody components. The torus model is extended to the hard limits with a sharp radial cutoff ($Y = 60, q = 0.0$). The entire model is best fitted with strong silicate absorption ($\tau_{9.7\mu m} = 1.39$) demonstrating the impact of host inclination on our models. Excepting a small feature at 7 μm, our model fits the continuum very well.

PGC 13946 (2MASX J03502477-5018354) Model = HG, NLR, S

The smaller of two likely interacting galaxies, Parisi et al. (2009) identify the AGN as a Sy 2 using optical spectroscopy. This is supported by $2-10\,\mathrm{keV}$ absorption (Winter et al., 2009, $N_H = 14.40^{+7.40}_{-5.90} \times 10^{22} cm^{-2}$). It lacks high resolution observations, so we cannot identify it's morphology. Using DSS imagery, we note a large elongated neighboring galaxy with asymmetric features possibly indicative of interaction with PGC 13946. The low-resolution IR spectrum shows prominent host galaxy features that our model reproduces well. Both torus and NLR components contribute significantly to the model as well, especially above $20\,\mu$m and below $6\,\mu$m. The entire model is subjected to strong IR silicate absorption ($\tau_{9.7\mu m} = 1.12$).

SBS 1301+540 Model = BB, S

W10 identify this galaxy as a Sy 1 based on broad emission lines, but note these line profiles are complex and "boxy". In SDSS images, it appears to be an edge on disk ($S0^+$) adjacent to a foreground star. Winter et al. (2008) note no X-ray absorption. Our findings are similar with only slight IR absorption ($\tau_{9.7\mu m} = 0.47$). The flat low-resolution IR spectrum is very well fit by a face-on, thin torus ($\sigma = 19.1°, i = 19.7°$) and a blackbody model.

UGC 03601 Model = HG, NLR

A Sy 1.5 is embedded in a symmetric but poorly resolved galaxy of unknown morphology. The IR spectrum continuum is well fit, but the line strength appears to vary between high- and low-resolution data sets. Our error bars completely account for the mismatch, and our models the small error bar, low-resolution data well. We

utilize a dominant torus component along with host galaxy and NLR contributions in order to fit our data.

UGC 04013 (MRK 10) Model = HG, NLR, BB, S

This AGN is classified as a Sy1 galaxy (Contini et al., 1998; Khachikian & Weedman, 1974; Osterbrock, 1977). The host galaxy is a slightly inclined Sb galaxy. In order to reproduce the incredibly flat low-resolution IR spectrum, we use torus, NLR, host galaxy, and blackbody components in our model. We also incorporate weak silicate absorption ($\tau_{9.7\mu m} = 0.45$). The data is well fit statistically despite rather small flux errors on the data.

UGC 06728 Model = BB, S

This inclined SB0/a galaxy contains a Sy 1.2. It is immediately adjacent ($\sim$ 15 arcsec) to a bright point source that is missed by our slits. (Winter et al., 2008) observe no X-ray absorption. We similarly model our data with very weak silicate absorption ($\tau_{9.7\mu m} = 0.24$). The high-resolution modules of the spectrum are quite noisy, especially at the long-wavelength end. The torus and blackbody model we use fits the data with minimal continuum deviation.

UGC 11871 Model = HG, NLR, S

W10 cite KPNO spectra used to classify this AGN as a Sy 1.9. The X-ray spectrum is slightly absorbed supporting this classification (Winter et al., 2009, $N_H = 2.39^{+0.71}_{-0.56} \times 10^{22} cm^{-2}$). The galaxy is asymmetric with a strong southern diffuse feature overlapping the adjacent point source leading earlier researchers to consider

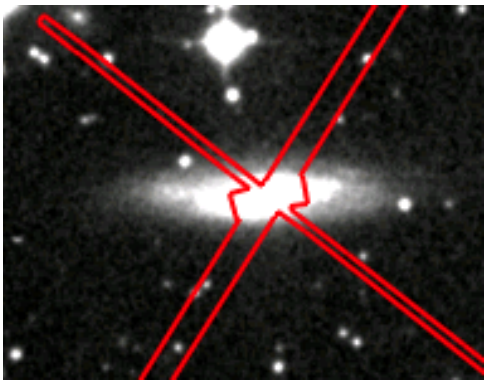

Figure 6.2: We project the location of the IRS slits for each module over an DSS image of UGC 12282. Both high-resolution slits are completely filled by the host galaxy flux. One summed slit region is given for each module for clarity.

it a galaxy pair. Strong PAH features of the low-resolution IR spectrum are well modeled by our host galaxy model. The other 50% of our model flux comes from torus and NLR components leading to an IR model that fits the entire continuum well. The average flux error is 1.8% while the average model displacement is 3.8%.

UGC 12282 Model = HG, S

This is a nearly edge-on Sa galaxy containing a Sy 1.9 at its core. The high- and low-resolution IR spectra for this object differ substantially in continuum flux. We model the data with two different host galaxy normalizations as the only difference in observations was slit size. Visual inspection of the slit location confirms that the host galaxy is extended well beyond the slit widths (Figure 6.2). We expect the slightly different slit size and orientations to encapsulate different amounts of extended host emission. With this caveat, our model includes only torus and host galaxy contributions. The model fits the data reasonably well, but deviates below 6 μm.

UGC 12741 Model = HG, NLR, S

One of the newly discovered AGN, Tueller et al. (2010) classified UGC 12741 optically as a Sy 2 using KPNO spectra. Its host galaxy is an inclined spiral (Sa). We model the spectrum with torus, NLR, and host galaxy models. The host and torus models have nearly equal flux contributions while the NLR is relatively faint. The model deviates from the data below 6 μm.

UM 614 Model = NLR, S

This AGN is classified as a Sy 1.8 (Terlevich et al., 1991). The host galaxy is resolved to have slightly inclined S0 morphology. We fit the relatively simple IR spectrum with a torus and NLR model. The data is well represented by the model throughout the spectrum.

6.2 Testing the Applicability of the Dusty Torus Model

In this section, spectral fitting results are presented within the context of the models being tested. To remind the reader, these models are the dusty obscuring torus region (Section 3.3.3), the NLR continuum model (Section 3.3.4), and the host galaxy emission model (Section 3.3.2). The torus parameterized by its thickness expressed as a Gaussian width about the polar angle (σ), the torus radius, given as a multiple of the inner radius (Y), the number of clouds along an equatorial ray (N_0),

the power law slope of the radial density (q), the optical depth of each cloud (τ_v), and the inclination of the observer relative to the torus normal (i). The NLR model is parameterized by the ionization parameter (U) and the normalization. The host galaxy is parameterized by the fraction of light emitted by circumstellar dust (γ), the starlight intensity for the diffuse dust (U_{min}), and the fraction of IR flux emitted by the host galaxy (f_{host}). We supplement these models with a high temperature blackbody component used by others in the field (e.g., S08, M09) which our data cannot explain. All the emission is subject to intervening silicate emission from non-AGN dust parameterized by optical depth ($\tau_{9.7\mu m}$).

The ensemble nature of the dust clouds of our torus model allows for a more complex relationship between accretion disk inclination and AGN type than a constant density torus. The likelihood of a viewer observing the accretion disk from a direction that is not blocked by torus clouds depends on the interplay between torus inclination (i), cloud density (N_0), cloud optical depth (τ_v), and torus disk thickness (σ). The distribution of individual P_{esc} values (Section 3.3.3) is plotted against torus inclination for the sample in Figure 6.3. A trend of decreasing P_{esc} with increasing inclination is obvious. We note a group of Sy 2s with high inclination and low escape probabilities as we would expect. The probabilistic nature of P_{esc} implies a small fraction of obscured AGN will have high escape probabilities (i.e., if our models are accurate, we predict 10% of the models with $P_{esc} = 10\%$ will be unobscured).

Figure 6.4 shows a histogram of the fraction of AGN within a probability bin that

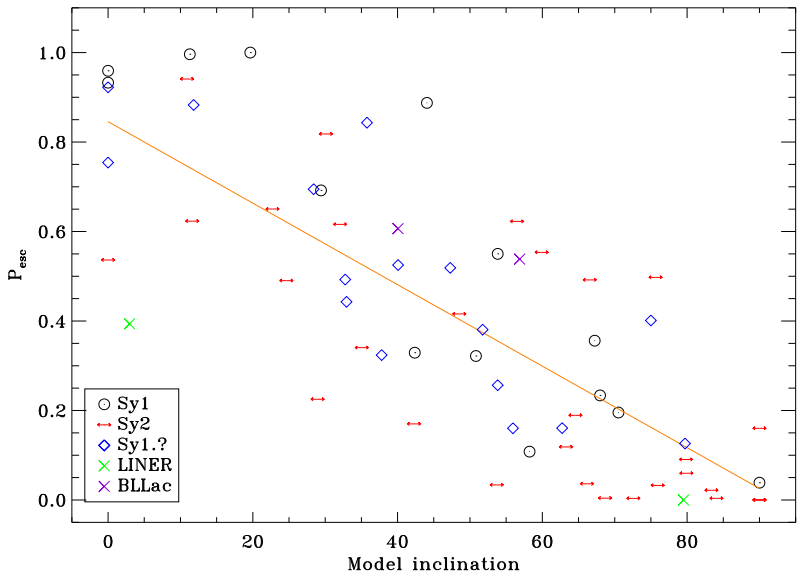

Figure 6.3: Escape probability for visible photons for each AGN plotted against model inclination. The orange line indicates the linear best-fit to the data.

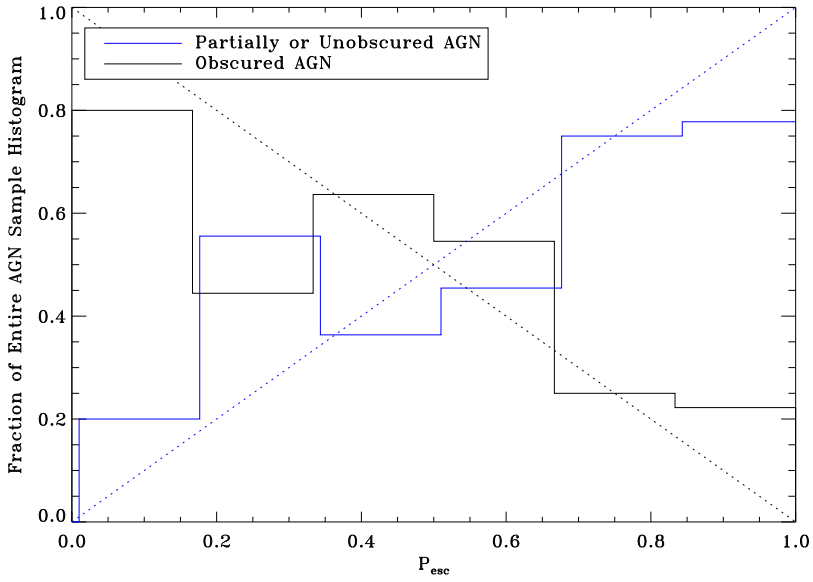

Figure 6.4: The fraction of obscured and unobscured (see text) AGN within the P_{esc} histogram bin are plotted. The dotted intersecting lines represent the ideal distribution.

are classed as either obscured or unobscured . Adopting the standard unified model, we assume LINER, Sy 1.9, and Sy 2 galaxies are obscured AGN and Sy 1, 1.2, 1.5, 1.8, and BL Lac objects are unobscured AGN. We predict accurate torus models will create a distribution of P_{esc} values for obscured and unobserved AGN that match the dotted lines. Our model escape probabilities reflect adherence to the expected behavior.

We test how significantly our histogram differs from the prediction by simulating ten thousand sets of randomly distributed AGN types based on our P_{esc} values. Any given AGN is labeled as either obscured or unobscured if a pseudo-random number drawn from a uniform distribution between 0 and 1 is above or below P_{esc} respectively. We recreate the histogram of Figure 6.4 and measure the displacement of the data from the theoretical prediction. Our data give a mean displacement of 12.4% per bin whereas the mean displacement for our ten thousand simulations of 66 AGN is $11.9 \pm 4.0\%$. We consider this statistic along with Figure 6.4 a clear indicator that our torus models have managed to create an indicative geometric parameter that is verified by optical obscuration data. We predict that the two objects with unknown activity classifications (MRK 18 & NGC 4686) are likely to be unobscured and obscured respectively ($P_{esc} = 0.728$ & 0.037).

An additional ramification of our soft edged clumpy torus distribution is a complicated covering factor. We rely on two separate methods for determining this covering factor (c_{tor}) similar to the M09 analysis. The first method uses the specific ge-

ometry of each modeled torus to integrate the P_{esc} values at all observation angles ($\int P_{esc}(i)\,di$). When subtracted from one, this gives the probability of absorption for any visible photon emitted by the AGN or what M09 call a geometric covering factor (c_{tor}^{geo}). The value utilizes all the relevant torus geometry to predict a robust covering factor. Errors in torus model parameters that may have minimal impact on the torus SED can substantially influence this value. An alternative apparent covering factor (c_{tor}^{app}) can be found by finding the ratio of clumpy torus emission to the bolometric luminosity (M09). Although not mentioned by authors that have used this technique, this apparent covering factor assumes the torus is opaque at all energies; a clear approximation. Given the significant flux that passes through the torus in the form of hard X-rays, we presume c_{tor}^{app} will underestimate the covering factor. Both of these parameters are plotted in Figure 6.5 to demonstrate the slight disparity. The distributions are remarkably similar and the slight shift in mean could be explained by the c_{tor}^{app} approximation, a 16% systematic underestimate of bolometric luminosity, or with small deviations in parameter values with minimal impact on SED shape. Our mean apparent covering factor ($\bar{c}_{tor}^{app} = 38\%$) matches well with that of M09 (34%), but our mean geometric covering factor ($\bar{c}_{tor}^{geo} = 54\%$) is twice the value they find. The significantly more luminous Type 1 sample of M09 may have qualitatively different torus properties (e.g., luminous emission may work to flatten the torus, see Section 4.7). M12 similarly find low apparent covering factors for their sample of luminous Type 1 AGN (median of $c_{tor}^{geo} = 25\%$) but note anti-correlation between bolometric

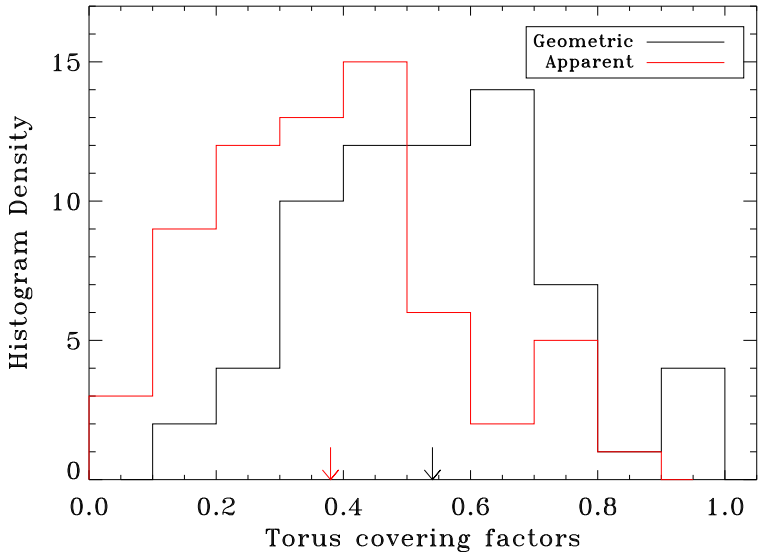

Figure 6.5: Histogram of torus covering factors. Explanation of geometric vs. apparent covering factors in text. Average for each parameter is shown with downward arrow.

luminosity and covering factor. Conversely, the differing methodologies of our analysis 3.4 may favor different covering factors as a result of different amounts of light attributed to the torus.

6.3 NLR Geometric Parameters

Our relatively simple NLR model SED shape is parameterized by a single ionization parameter, but when combined with the normalization and L_{bol} we can derive both the radius and covering factor of the feature (Figure 6.6). We determine the location of the NLR by simply determining where the incident flux (F_{in}) yields the best-fit ionization parameter ($R_{NLR} = \sqrt{\frac{L_{bol}}{4\pi F_{in}}}$). We find the average $R_{NLR} = 9.96\,\mathrm{pc}$

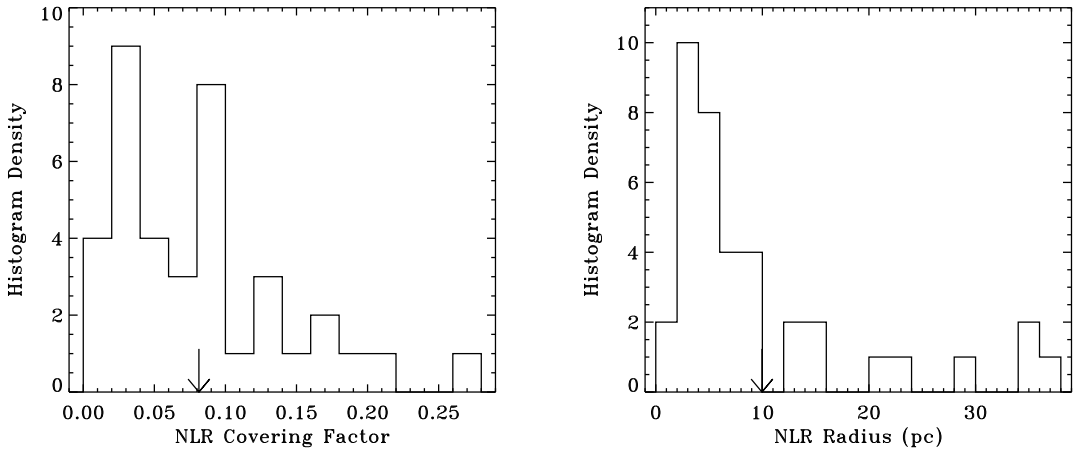

Figure 6.6: Histograms of NLR geometric parameters derived from L_{bol}, $\log(U)$, and NLR model normalization. Large arrows denote parameter averages.

or $138 \times R_i$. Previous attempts to model NLR using the G06 models have given significantly larger radii (S08: $R_{NLR} \sim 170 \times R_i$, M09: $R_{NLR} \sim 700 \times R_i$) for their much more luminous samples of Type 1 AGN. In Figure 6.7, we plot our R_{NLR} against bolometric luminosity and compare it these other samples. Our fainter and closer sample exhibits a larger spread about the best fit power-law, likely a result of the variety of AGN types we are modeling. All the data points roughly agree with a square root L_{bol} – R_{NLR} relationship expected for single-cloud, constant U, photo-ionization models. Because both previous samples utilize different fitting methodologies and models (see Section 3.4), we choose not to delve too deeply into why the best power-law fits of the L_{bol} vs. R_{NLR} differ slightly. Instead we focus on the fact that despite the six decades of luminosity coverage we modeled, the NLR clouds can be consistently well modeled with an incredibly simple single-cloud model.

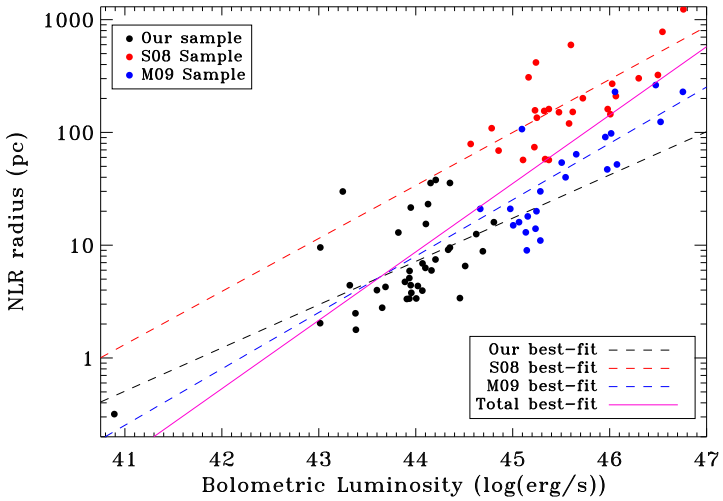

Figure 6.7: NLR radius plotted against bolometric luminosity. Also shown are previous results from the literature along with their best-fit lines. The best-fit to all the data points is shown in magenta.

S08 compute the covering factor of the NLR model by determining the NLR flux compared to the incident flux on the NLR model given the previously found R_{NLR} value ($c_{NLR} = \frac{F_{NLR}}{F_{in}} \frac{D_L^2}{R_{NLR}^2}$). Remembering the origin of R_{NLR}, this simplifies to $c_{NLR} = \frac{L_{NLR}}{L_{bol}}$ and is subject to the same underestimation as c_{tor}^{app} (Section 6.2). Because the NLR is assumed significantly more transparent than the torus, the underestimation should be substantially more acute. Kriss et al. (1992) propose an NLR covering factor upper limit of $\sim 30\%$ based on *HST* imaging. All of our covering factors lie below this cutoff. Our resulting mean covering factor is remarkably close to that of M09 with very similar distributions (our $\bar{c}_{NLR} = 8\%$, their value is 7%). Meléndez et al. (2008) similarly find a mean covering factor of 7% using line diagnostics and photoionization models for the BAT AGN sample. This level of agreement is notable

given the completely different methodologies and measurements used. Figure 6.8 shows the NLR covering factor plotted against the geometric and apparent torus covering factors. We also show the line depicting where the total covering factor of these two features exceeds one. Two of our AGN models exceed this boundary (NGC 4102 and ESO 549 G049) when using the geometric covering factor. The one and five percent covering factor excess demonstrates the inherent error of our torus models especially when considering parameters with only small impact on the IR SED. This is exemplified by the fact that the individual models with a total covering factor (using a geometric torus covering factor) near or exceeding one are the most significantly reduced when compared to the torus apparent covering factor. These data show that the torus geometry can substantially overestimate the covering factor in a few cases. Although the torus shadow serves as a helpful theoretical limit to the NLR size, we note that the majority of the NLR covering factors occupy a small fraction of the available space above and below the accretion disk. NLR occupy on average 15% or 24% of the available space using c_{tor}^{app} and c_{tor}^{geo}, respectively. We expect the NLR covering fraction derived with our methodology to remain small as the majority of emission passes through them in unobscured AGN.

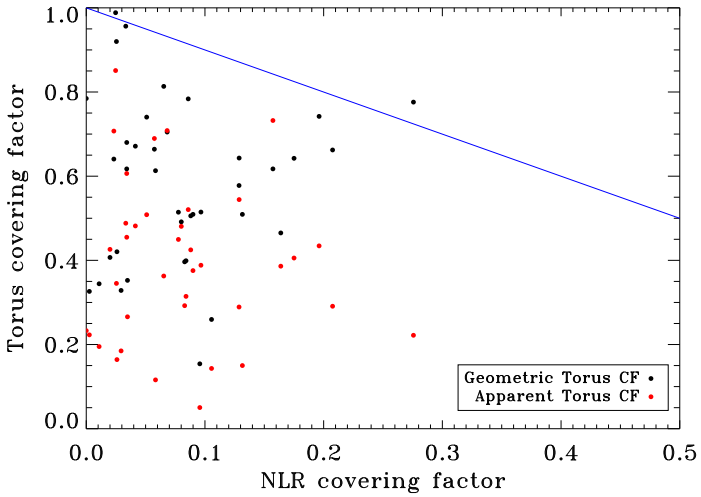

Figure 6.8: The best-fit torus covering factors (both geometric and apparent) are plotted against the NLR covering factor. In blue we give the boundary at which the total covering factor exceeds one.

6.4 Parameter Correlations

We use the statistical correlations between best-fit model parameters to determine there are 18 parameter pairs with strong correlation. Assembling all of our parameters and quantifiable AGN attributes (i.e., covering factor, host galaxy flux fraction, bolometric luminosity) while omitting instances where a model does not include a specific component, we create arrays of Kendall τ rank correlation coefficients ($K\tau$). This robust non-parametric hypothesis test of statistical dependence is sensitive to non-linear monotonic relationships. We visually check the relationships when the null hypothesis probability (P_{null}) is less than 5% yielding 18 parameter correlations which we inspect. Monte Carlo testing reveals that even with random uniform or random normal distributions of parameters we expect around 8 false positives with our visual

inspection criterion.

6.4.1 Torus Radial Density

First we examine the radial density of clouds in the tori. As shown in Section 3.3.3 this is parameterized by the total number of clouds along an equatorial line-of-sight (N_0).

Figure 5.5 reveals that our Sy 1s have smaller density values than our Sy 2s, which are spread evenly across the tested range. We confirm this quantitatively with a strong AGN type – N_0 correlation ($K_\tau = 0.38$). The density parameter controls whether or not the backside of the torus is visible at near edge-on inclinations, an effect that decreases with decreasing inclination. The Sy 1 density distribution could be skewed because our models artificially lower the density instead of the inclination to account for backside emission, but we have determined that this cannot be a significant effect. Failing to reduce the inclination in this scenario would result in a distribution of inclinations characteristically lower than expected for the low density AGN population. A K-S test shows 91% likelihood the low-density inclinations are drawn from a uniform sample, exactly what we expect for models that accurately fit inclination. The K-S test supports the idea that we are fitting the low-density spectra inclinations correctly. The test is supported by the similar inclination and disk thickness distributions for the low- and high-density groups ($\bar{i} = 47.6^\circ$ & 50.8°, $\bar{\sigma} = 39.8^\circ$ & 39.4° respectively).

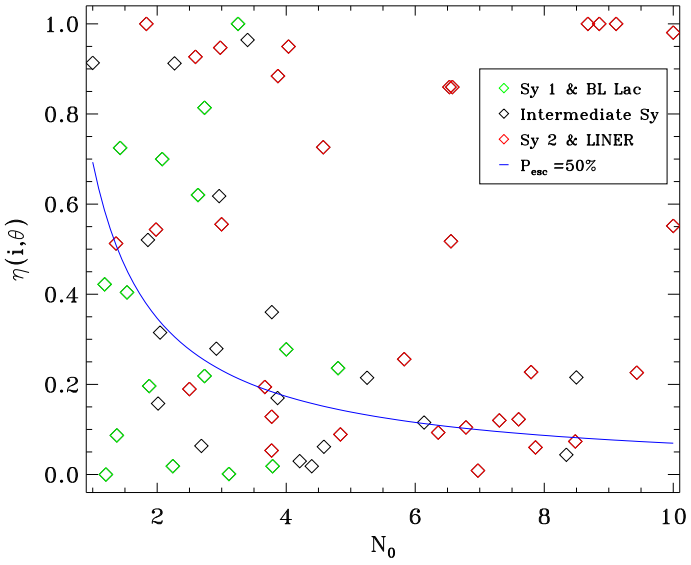

Figure 6.9: The equatorial cloud density is plotted against the angle dependency factor for each best-fit model. The unobscured, partially obscured, and obscured AGN are plotted in green, black, and red respectively. We also plot the line where P_{esc} is equal to 50%.

The data cannot distinguish between low- and high-density models when the line-of-sight of the observer is well out of the plane of the disk of the torus. Figure 6.9 shows the angle dependency factor of our best-fit models $(\eta(i,\sigma)) = \exp(-(90^\circ - i)^2/\sigma^2))$ which is multiplied by our equatorial density factor (N_0) to determine the average number of clouds in our line of sight. Over this we plot a line denoting where $P_{esc} = 50\%$. The plot reveals a sample of Sy 2 near the $P_{esc} = 50\%$ line with small $\eta(i,\sigma)$ and large densities. No accompanying Sy 1s are in this region despite the P_{esc} prediction that half the objects in the region should be unobscured. We conclude that a small fraction of the Sy 1s has an underestimated density when the line of sight is well out of the disk. The similarity between model spectra at these low angles causes this

underestimation and insures that it has little effect on the other torus parameters.

6.4.2 Measuring the Size of the Dusty Torus

We remind the reader of the importance of the Y parameter in the torus model. Y is a dimensionless parameter defined by the ratio of the outer to inner torus radius – and as the size of the torus grows, Y increases.

As the bolometric luminosity increases the Y parameter decreases (Figure 6.10). The Kendall correlation coefficient (K_τ) is -0.19 with a P_{null} of 2.6%. We account for the lack of a sharp cutoff when the radial power-law exponent (q) is larger than zero by plotting $Y_{10\%}$, the radius where the linear cloud density is below 10% the initial density (Figure 6.10). As the bolometric luminosity increases beyond 1.2×10^{44} erg s^{-1}, the mean $Y_{10\%}$ parameter goes from 26.1 to 11.6. Although we could speculate that the torus properties shift above a threshold luminosity, the number of data points above this threshold is small. Modifying $Y_{10\%}$ to represent a more physical concept – the outer radius (R_{outer}) in parsecs – we find that R_{outer} is directly correlated with L_{bol}. In Figure 6.10, we plot the best linear fit for both the outer radius (R_{outer}) and $Y_{10\%}$. The sign change of the correlations implies the dust sublimation determined inner radius dominates the negative $Y_{10\%} - L_{bol}$ correlation. The positive correlation of $R_{outer} - L_{bol}$ demonstrates torus growth with luminosity, which is a significant result of this thesis.

Our torus sizes corroborate previous attempts at luminosity – size relationships

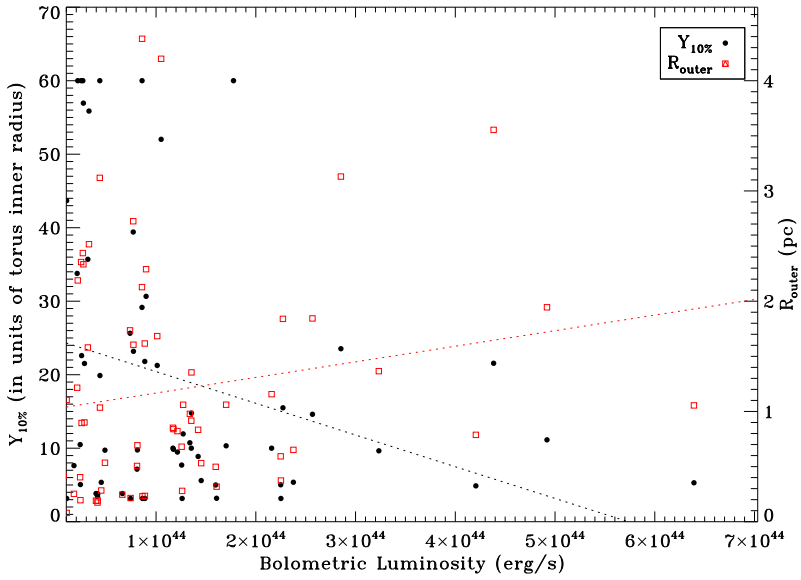

Figure 6.10: We plot both the $Y_{10\%}$ (see text) and R_o of our best fit models. The left axis scale corresponds to $Y_{10\%}$ while the right denotes R_o.

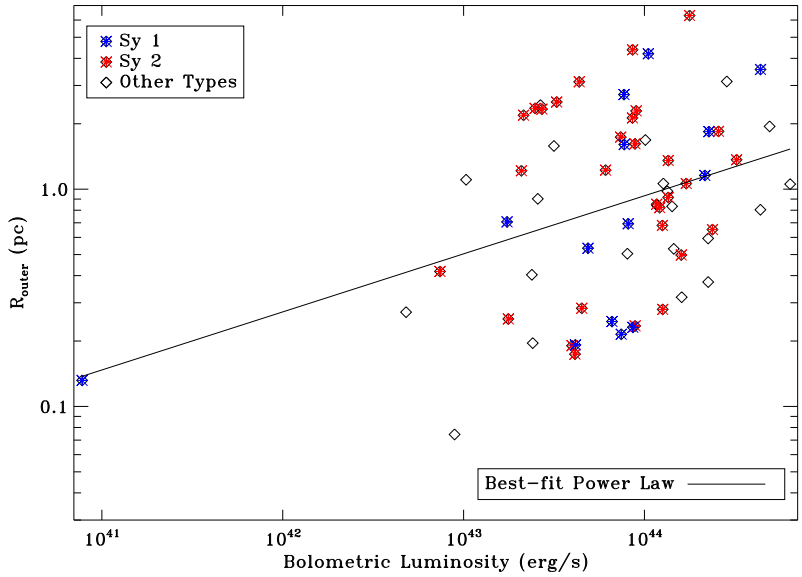

Figure 6.11: The logarithmic depiction of the outer radius and bolometric luminosity depicts the boundaries within which the parameters are allowed to vary as well as the best-fit power law. Sy 1 and Sy 2s are plotted in color to demonstrate their similar distributions.

and thus illustrate the validity of applying the dusty torus model to IR spectra. Tristram & Schartmann (2011) use IR interferometric observations of 10 Seyferts with the assumption of a Gaussian spatial emission profile to determine the torus size when viewed at 12 μm. These authors report sizes that scale roughly with the square root of the 12 μm luminosity. We find that within our tested boundaries, the data are best fit by a power-law with an exponent of 0.285 ± 0.079 (Figure 6.11). Given the shielding that occurs, it is logical that clouds at the periphery are less affected by changes to bolometric luminosity compared to the inner radius, yielding a flatter outer radius-luminosity relationship.

Further tests of the outer radius show no surprising correlations. There is no significant size difference in type 1 and type 2 AGN populations on the bolometric luminosity – outer radius plot (Figure 6.11).

We hypothesize and test whether the degree of hard X-ray variability might impact the overall torus size. Presuming the clouds are impacted by radiation, substantial deviations from our time averaged hard X-ray flux might contribute momentum and inflate the torus size. In Figure 6.12 we test this idea. We use the variability estimator S_{Vc} of Beckmann et al. (2007, references within) in order to quantify the degree of hard X-ray variability found in the 70-month light curves of our AGN. Beckmann et al. (2007) adapted a previously used variability estimator for use with Swift BAT AGN data and discovered a tendency for obscured AGN to exhibit more variability than unobscured AGN. The authors use a variety of temporal bin sizes in order to

probe across different time scales and find the most interesting correlations using 20-day bins. Our data are initially grouped in similar 20-day bins with systematic errors propagated. The variability estimator S_{Vc} is calculated by isolating source variance σ_Q from systematic measurement variance σ_i through maximizing the likelihood function $L(\sigma_Q|x_i, \sigma_i)$ for each light curve (Beckmann et al., 2007). The resulting variance is corrected for background using the variance of empty fields measured by Beckmann et al. (2007) before being converted to a percentage of the source count rate yielding S_{Vc}. In order to determine errors for this estimator, we use Monte-Carlo simulations creating 500 synthetic light curves for each source assuming a Gaussian distribution for each flux measurement. These simulated data are binned and fit identically to create a distribution of σ_Q and corresponding S_{Vc} values. Our errors are the standard deviation of these S_{Vc} values.

The X-ray variability correlates weakly with the torus outer radius size ($K_\tau = 0.14, P_{null} = 7.9\%$). This weak correlation shows that hard X-ray variation above the 20-day timescale does not impact torus growth. Increasing bin size to 40 days decreases the correlation significantly ($K_\tau = 0.08, P_{null} = 34.4\%$). Decreasing bin size to 7 days incorporates smaller scale variations yielding a larger correlation ($K_\tau = 0.18$) with a null hypothesis likelihood of 3.0%. The correlation is plotted in Figure 6.12 with its best-fit linear relationship. A negative variability estimator implies the systematic error has been overestimated for the rate measurements. We include negative values because we assume that the systematic error is uniformly overestimated and we

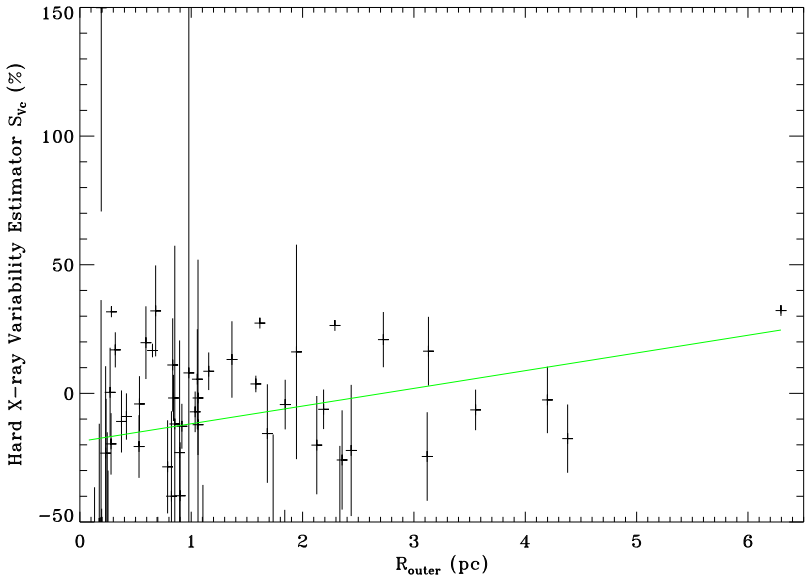

Figure 6.12: The hard X-ray variability estimator found using 7-day bins is plotted against the clumpy torus outer radius. Parameter definitions can be found in the text

are more interested in relative variability than absolute variability. The binning required to exclude the null hypothesis at our 5% threshold implies that short timescale variability most significantly impacts torus size. Only variability intrinsic to the AGN can vary on this timescale implying accretion disk luminosity changes are the torus cloud driving force.

6.4.3 The Contribution of the Host Galaxy Light to the IR

The host galaxy fraction of the IR flux (f_{host}) decreases with increasing AGN IR luminosity ($K_\tau = -0.25, P_{null} = 4.1\%$).This confirms that the spectra are dominated

by the AGN in the IR. As AGN IR strength increases, it becomes brighter compared to the host galaxy, requiring a smaller f_{host} value. This correlation reaffirms the lack of a link between AGN and host galaxy luminosity.

The f_{host} parameter also scales strongly with $\log(U)$, the NLR ionization parameter ($K_\tau = -0.55, P_{null} = 0.07\%$). It appears that when the ionization parameter decreases, the host galaxy fraction linearly increases. This is predictable as NLR flux is included in the total IR luminosity of the AGN and the ionization parameter significantly impacts the strength of the NLR flux (Figure 3.7). Finally, we note f_{host} correlates with q_{PAH} as the PAH contribution scales the total IR host galaxy contribution below 20 μm (see Figure 3.4).

6.4.4 Silicate Absorption Correlations

The silicate model is incorporated into the model to account for absorption not intrinsic to the AGN. But is the intervening material totally independent of the AGN? We find substantial correlations between $\tau_{9.7\mu m}$ and AGN type ($K_\tau = 0.29, P_{null} = 0.2\%$) and N_0 ($K_\tau = 0.23, P_{null} = 1.1\%$). The former can be explained with the idea that some obscured AGN are not just blocked by a classic torus. Previous work has suggested that host galaxy dust could impact AGN classification (e.g., Maiolino & Rieke, 1995; Rigby et al., 2006). We use the host galaxy major and minor axis sizes in NED to divide our sample into highly inclined ($a/b > 1.67$) and face-on groups. The correlation between optical AGN type and $\tau_{9.7\mu m}$ vanishes for

the face-on sample ($K_\tau = 0.19, P_{null} = 16\%$) and remains for the inclined group ($K_\tau = 0.42, P_{null} = 0.2\%$). A complication is that $\tau_{9.7\mu m}$ should be independent of N_0 if our models perfectly encapsulated the physics of the disparate obscuration regions. The degree of obscuration from host galaxy dust occurs on scales tens of thousands time larger than the torus obscuration, defined in this case by the torus density (N_0). Some fraction of the galaxy dust is inflating the AGN torus density in our model. We isolate this effect by determining the correlation parameters for the inclined and face-on host galaxy samples separately. Once again, the correlation disappears when only face-on host galaxies are considered ($K_\tau = -0.03, P_{null} = 84\%$). Our data demonstrate that highly inclined host galaxies add substantial silicate absorption thus impacting the assigned AGN classification. We discuss this result in Chapter 7.

6.4.5 Other Correlations of Note

Several correlations arise that we cannot easily explain. The disk thickness (σ) and inclination (i) show slight correlation with a $K_\tau = 0.27$ and $P_{null} = 0.16\%$. This relationship has no physical explanation; the orientation of the AGN should be independent of every other parameter. Analysis of the $i - \sigma$ plot shows that below inclinations of $\sim 40°$, the σ values are less broadly distributed about a slightly higher mean. We believe that because the disk thickness does not significantly affect the spectrum in face-on models, adjustment of the σ parameter remains small. This is supported by the fact that below $i = 40°$, the average σ value ($45.16°$) is very close

to the initial guess of 45°.

We find that the ionization parameter ($\log(U)$) of our NLR model scales strongly with the outer radius size (R_o) of the torus model ($K_\tau = 0.36, P_{null} = 0.1\%$). This correlation remains even when the scaled torus outer radius ($Y_{10\%}$) is used so that the result is independent of bolometric luminosity ($K_\tau = 0.29, P_{null} = 1.0\%$). Both of these relationships imply the torus size is anti-correlated with the NLR radius. Any radiative pressure driven clouds would be expected to act similarly in the torus and the NLR. The unaccountable correlation may be caused by the simplicity of our NLR models that approximate the NLR with a thin shell exposed to a single ionization parameter (the actual NLR is extended radially and stratified). The lack of any significant correlation between the ionization parameter and the luminosity (IR or hard X-ray), hard X-ray variability, or any other of our torus model parameters leaves us with no clear explanation for the correlation. We expect several spurious correlations given the number of parameter pairs tested; this may simply be one of them.

Chapter 7

Conclusions

In this chapter we examine the results of this thesis in the context of the open questions posed in Chapter 1. We examine the nature of the angle dependent toroidal obscuration region in the context of a minimally biased catalog of AGN. Additionally, we address AGN torus dynamics using both our static torus models and variability information. Our NLR models are used to discuss the isotropic nature of the NLR region. Finally, we attempt to link our data and models to the impact of AGN interactions with their host galaxies.

7.1 A Better Understanding of the the Obscuring Torus

We set out to understand the angle dependence of the obscuration region for our sample of AGN. We have demonstrated that a collection of clumpy torus models is capable of reproducing the wide variety of spectral shapes present in a minimally biased sample of AGN. The models inform us of plausible specific geometries for each AGN in our sample, regardless of AGN type.

One of the primary goals of AGN torus modeling is to reproduce the distribution of AGN type observed. Our subsample of BAT AGN contains thirty Sy 2's and thirty Sy 1-1.9's which we label as obscured and unobscured respectively. Added to the Seyferts, we have two LINERS, two BL Lac objects, and two AGN with unknown or significantly disagreed upon type. Our individual models yield geometric covering factors (c_{tor}^{geo}, Section 6.2) that describe the fraction of optical light that is blocked for each AGN. The average c_{tor}^{geo} for our sample is 54%, remarkably close to the fraction of unobscured AGN in our sample determined from optical emission. Through blind model fitting we have produced an ensemble of torus models with an average shape that matches the distribution of AGN type in our sample. This result is complemented by the ability of each individual model to predict the likelihood (P_{esc}) of observing the accretion disk optically without obscuration. The individual P_{esc} values for both the obscured and unobscured AGN reproduces the exact behavior we predict (Section

6.2). The probabilistic assignment of type lacks the precision of the Seyfert class system, but we are capable of making strong predictions regarding AGN obscuration based entirely on IR continuum emission. This finding is remarkable given the total lack of orientation or AGN type information originally fed into the model fitting process.

We have shown using our models a strong correlation between torus outer radius size and the AGN bolometric luminosity. The relationship is parameterized by a power-law with an exponent of 0.285 ± 0.079 (Figure 6.11). Although our static models cannot explain this correlation, it is interesting to see deviation from the square root relationship of illuminated single cloud models (i.e., the NLR or torus inner radius luminosity–distance relationships). Given the shielding by the torus of the AGN emission, it is logical that the clouds at the outer extent of the torus a less impacted by AGN luminosity.

The current state of IR AGN continuum models is not advanced enough to put statistically robust constraints on individual model parameters (Section 5.2 and M09). We can however examine bulk properties of our entire sample to estimate the appearance of a typical AGN torus (Figure 7.1). The torus consists of very optically thick clouds ($\bar{\tau}_v = 47$). The density of clouds decreases gradually as distance from the accretion disk increases at a rate of $r^{-0.63}$, until, at 27 times the inner radius, the density falls to zero. The number of clouds along an equatorial line of sight is typically around 4.5. The torus extends 40° above the surface of the disk with density

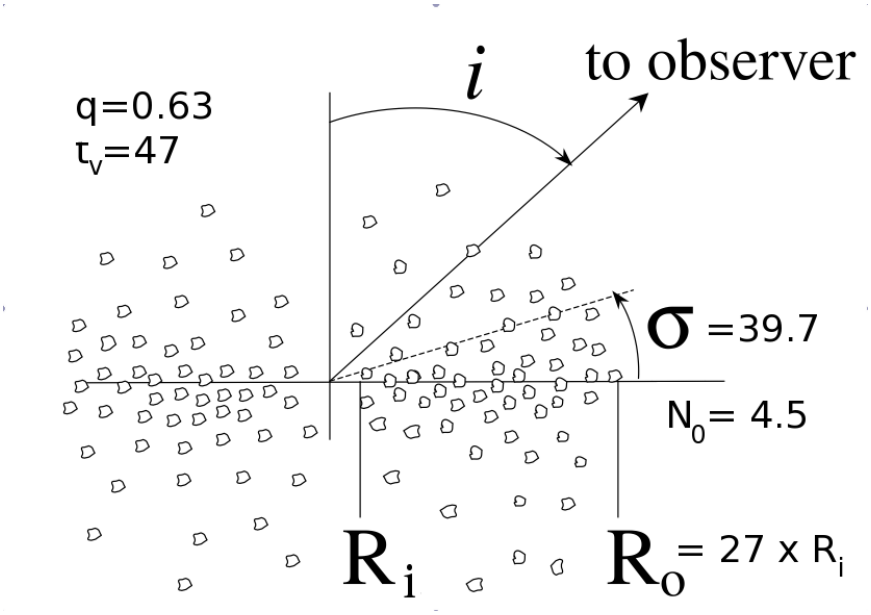

Figure 7.1: We show the Nenkova clumpy torus (N08) model with the average values for our sample.

decreasing as the poloidal angle increases. We cannot easily describe the torus height – radius ratio, but we can say that 54% of the optical light emitted by the AGN will be obscured. In terms of the putative solid torus, this corresponds to $H/R \sim 1$.

7.2 Torus Dynamics and Variability

Although none of our torus models contain information regarding torus dynamics, we are capable of arguing for cloud outflows by comparing our models to hard X-ray variability data. First we demonstrate the NGC 4395 IR data is best fit with models where the torus flattens when exposed to increased accretion disk radiation (Section 4.8). Looking at our entire data set, we have shown that hard X-ray variability

correlates with our model torus size (Figure 6.12). The timescale of the variation for this correlation is indicative that the torus clouds are shaped by changes in the accretion disk luminosity (Section 6.4.2).

We observe no significant correlation between hard X-ray variability and hard X-ray luminosity extending the 9-month Beckmann et al. (2007) result to our 70-month observations. We do see a significant IR luminosity – hard X-ray variability correlation ($K_\tau = 0.16, P_{null} = 0.5\%$). The fact that only IR flux has this correlation is notable because it signifies the short timescale variability directly affects the dust luminosity. The correlation between IR luminosity and hard X-ray variability decreases as the bin size increases. We further test the hard X-ray variability by comparing it to the angular separation of the line-of-sight and the soft edge of the torus ($\phi \equiv |(90^\circ - i) - \sigma|$). Presumably, obscuration based hard X-ray variability will be stronger when looking through the edge of the torus. The slight inverse correlation between ϕ and S_{Vc} increases with bin size and is strongest ($K_\tau = -0.15, P_{null} = 8.2\%$) when looking at the 40-day binned variability estimator. This insinuates that if edge-of-torus observations do increase variability (something we have not definitively shown), the hard X-ray variations likely take place with monthly timescales or greater. Our data support that hard X-ray variability inherent to the accretion disk impacts the IR luminosity as well as the torus outer radius size for our models. We suspect but cannot quantitatively demonstrate that longer timescale variations may be caused by torus dynamics near the edge of the obscuration region.

7.3 The Isotropic Nature of the NLR

Our NLR models are remarkably consistent with previous findings.We compare our NLR covering factors ($\bar{c}_{NLR} = 8\%$) to those derived by Meléndez et al. (2008) through photoionization modeling of BAT AGN line strengths ($\bar{c}_{NLR} = 7\%$) and find incredibly similar averages and distributions. The location of the NLR has been shown to scale with bolometric luminosity in our sample (see Figure 6.7 and Section 6.3). The correlation can be observed to scale through 6 decades in bolometric luminosity when added to the S08 and M09 results indicating both a strong correlation and model adept at fitting very different objects.

Although a full spectral line analysis of this data set is outside the scope of this thesis, we can gain insight comparing previous emission line studies for this sample (Meléndez et al., 2008; Weaver et al., 2010; Meléndez et al., 2011) to our model parameters and fluxes. We can easily reproduce the strong [OIV] 25.89 μm hard X-ray (14-195 keV) correlation of (Meléndez et al., 2008) with our sample ($K\tau = 0.39, P_{null} = 0.4\%$). This correlation is strengthened significantly when we use our IR and hard X-ray derived (Section 3.3.6) bolometric luminosity ($K\tau = 0.52, P_{null} = 7.7 \times 10^{-5}$). As we would expect, the correlation coefficient is further increased when we instead compare the NLR model luminosity to the [OIV] 25.89 μm luminosity ($K\tau = 0.54$), but the null hypothesis probability also increases because not all of our AGN have detectable NLR continuum components ($P_{null} = 0.47\%$). The [OIV] luminosity correlations strongly support our derived bolometric luminosities and highlight our ability

to accurately reproduce NLR continuum flux.

The incredibly strong link between our bolometric luminosity and the [OIV] 25.89 μm luminosity indicates [OIV] 25.89 μm emission is isotropic. We examine the correlations of our IR model components with the hard X-ray luminosity as it's value is completely independent of the IR spectrum. Of our model components, the NLR continuum correlates most strongly with hard X-ray emission ($K\tau = 0.45, P_{null} = 6.9 \times 10^{-5}$).

Weaver et al. (2010) find that six of the newly discovered BAT AGN are underluminous in [OIV] which they attribute to strong host galaxy dust extinction based on line ratios and edge-on host galaxy inclination. Our models show five of these AGN exhibit host galaxy obscuration and three have significantly larger IR optical depths ($\tau_{9.7\mu m} = 0.79, 1.26, 1.39$) than the average for our sample ($\bar{\tau}_{9.7\mu m} = 0.56$). The new AGN all show strong host galaxy emission (for new AGN: $\bar{f}_{host} = 37\%$) compared to the average of our entire sample ($\bar{f}_{host} = 16\%$) indicative of possible IR obscuration from the host galaxy. Although our silicate absorption and host galaxy models only weakly support the Weaver et al. (2010) galaxy extinction explanation for this small sample; our entire sample demonstrates the ability of the host galaxy to affect AGN type (Sections 5.3.2 and 6.4.4). This host galaxy obscuration causes NLR flux anisotropy for some galaxy types.

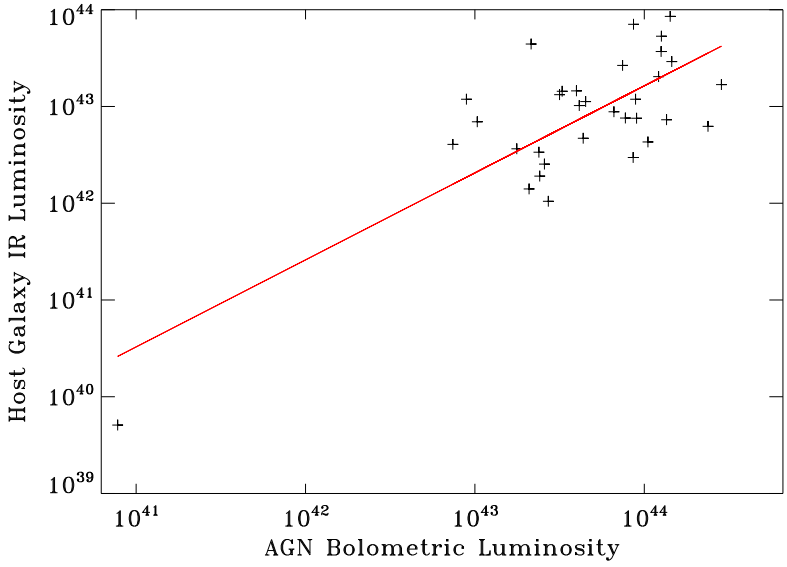

Figure 7.2: We plot the host galaxy IR luminosity against the AGN bolometric luminosity and see a clear correlation. The best-fit power-law to the data is shown in red.

7.4 Host Galaxy – AGN Interactions

Through our modeling of the AGN, we have modeled and studied the host galaxies as a method of isolating the AGN emission. In this section we will compare our models to the host galaxy orientation, flux, and parameter values in an effort to observe correlations between host galaxy and AGN features. Using the optically derived NED galaxy axis ratios, we compare the host galaxy inclinations to our model inclinations. No correlation exists ($K\tau = -0.06, P_{null} = 42\%$) corroborating the similar null result found with radio jet derived AGN inclinations (e.g., Schmitt et al., 1997; Clarke et al., 1998; Nagar & Wilson, 1999).

Figure 7.2 plots the host galaxy model luminosity against the AGN bolomet-

ric luminosity (L_{bol}) and shows a significant correlation ($K\tau = 0.33, P_{null} = 0.6\%$). The correlation persists when we compare the host galaxy to only IR or hard X-ray AGN luminosities ($K\tau = 0.31$ and 0.29 respectively). Together, these imply feedback between the BAT AGN and their host galaxies. Our host galaxy model flux is likely tracing star formation accelerated by AGN feedback. Diamond-Stanic & Rieke (2012) use both 24 μm continuum and 11.3 μm PAH feature strength to quantify star formation and find a similar correlation with [OIV] 25.89 μm luminosity, their stand in for AGN bolometric luminosity. We find no correlation between the host galaxy parameters and the AGN luminosity.

7.5 Future Avenues of Exploration

Our methodologies could be applied to both larger data sets or more detailed models with minimal adjustments. Because *Spitzer* IRS is no longer functional, archival AGN spectra represent the best option for further testing of our models. The advantages of our minimally biased BAT AGN derived sample would be lost, but hundreds of AGN spectra are available to model.

We could also compare our AGN spectra to a collection of non-active galaxies to determine whether IR spectra could be used to exclude the possibility of AGN presence in normal galaxies. We consider this a weak search methodology, but the ramifications of this study could be used to improve and justify the search for AGN

using IR photometric observations and color selection. As our ideas regarding AGN torus geometries are refined, our methodology and XSPEC adaptations could easily accommodate more complex theoretical models. These might include more sophisticated and better tested host galaxy models, torus models featuring a variety of cloud optical depths or different grain properties, torus models that incorporate additional carbonaceous dust components within the silicate dust photo-disassociation boundary, or even dynamically justified torus simulations.

Bibliography

Abel, N. P., & Satyapal, S. 2008, ApJ, 678, 686

Abramowicz, M. A., Chen, X., Kato, S., Lasota, J.-P., & Regev, O. 1995, ApJ, 438, L37

Adams, T. F. 1977, ApJS, 33, 19

Ahn, C. P., et al. 2012, ApJS, 203, 21

Alloin, D., Pantin, E., Lagage, P. O., & Granato, G. L. 2000, A&A, 363, 926

Alonso-Herrero, A., et al. 2006, ApJ, 640, 167

Antonucci, R. 1993, ARA&A, 31, 473

Arnaud, K. A. 1996, in Astronomical Society of the Pacific Conference Series, Vol. 101, Astronomical Data Analysis Software and Systems V, ed. G. H. Jacoby & J. Barnes, 17

Balbus, S. A., & Hawley, J. F. 1991, ApJ, 376, 214

BIBLIOGRAPHY

Barger, A. J., ed. 2004, Astrophysics and Space Science Library, Vol. 308, Supermassive Black Holes in the Distant Universe

Barthelmy, S. D., et al. 2005, Space Sci. Rev., 120, 143

Barvainis, R. 1987, ApJ, 320, 537

Baumgartner, W. H., Tueller, J., Markwardt, C. B., Skinner, G. K., Barthelmy, S., Mushotzky, R. F., Evans, P., & Gehrels, N. 2012, ArXiv e-prints

Beckmann, V., Barthelmy, S. D., Courvoisier, T. J.-L., Gehrels, N., Soldi, S., Tueller, J., & Wendt, G. 2007, A&A, 475, 827

Begelman, M. C., McKee, C. F., & Shields, G. A. 1983, ApJ, 271, 70

Begelman, M. C., & Nath, B. B. 2005, MNRAS, 361, 1387

Bennert, N., Jungwiert, B., Komossa, S., Haas, M., & Chini, R. 2006, A&A, 459, 55

Bock, J. J., et al. 2000, AJ, 120, 2904

Brandl, B. R., et al. 2006, ApJ, 653, 1129

Bregman, J. N. 1990, A&A Rev., 2, 125

Burenin, R. A., Mescheryakov, A. V., Revnivtsev, M. G., Sazonov, S. Y., Bikmaev, I. F., Pavlinsky, M. N., & Sunyaev, R. A. 2008, Astronomy Letters, 34, 367

Chiar, J. E., & Tielens, A. G. G. M. 2006, ApJ, 637, 774

BIBLIOGRAPHY

Clarke, C. J., Kinney, A. L., & Pringle, J. E. 1998, ApJ, 495, 189

Claussen, M. J., & Lo, K.-Y. 1986, ApJ, 308, 592

Contini, T., Considere, S., & Davoust, E. 1998, A&AS, 130, 285

Crenshaw, D. M., & Kraemer, S. B. 2000, ApJ, 532, L101

Cutri, R. M., Nelson, B. O., Francis, P. J., & Smith, P. S. 2002, in Astronomical Society of the Pacific Conference Series, Vol. 284, IAU Colloq. 184: AGN Surveys, ed. R. F. Green, E. Y. Khachikian, & D. B. Sanders, 127

Dahari, O., & De Robertis, M. M. 1988, ApJS, 67, 249

Davis, S. W., & Laor, A. 2011, ApJ, 728, 98

de Grijp, M. H. K., Keel, W. C., Miley, G. K., Goudfrooij, P., & Lub, J. 1992, A&AS, 96, 389

de Grijp, M. H. K., Lub, J., & Miley, G. K. 1987, A&AS, 70, 95

Desroches, L., et al. 2006, ApJ, 650, 88

Di Matteo, T., Springel, V., & Hernquist, L. 2005, Nature, 433, 604

Diamond-Stanic, A. M., & Rieke, G. H. 2012, ApJ, 746, 168

Diamond-Stanic, A. M., Rieke, G. H., & Rigby, J. R. 2009, ApJ, 698, 623

Dopita, M. A., et al. 2005, ApJ, 619, 755

BIBLIOGRAPHY

Draine, B. T., & Li, A. 2007, ApJ, 657, 810

Efstathiou, A., & Rowan-Robinson, M. 1995, MNRAS, 273, 649

Elitzur, M., & Ho, L. C. 2009, ApJ, 701, L91

Elvis, M. 2000, ApJ, 545, 63

Elvis, M., et al. 1994, ApJS, 95, 1

Emmering, R. T., Blandford, R. D., & Shlosman, I. 1992, ApJ, 385, 460

Evans, I. N., Ford, H. C., Kinney, A. L., Antonucci, R. R. J., Armus, L., & Caganoff, S. 1991, ApJ, 369, L27

Fanaroff, B. L., & Riley, J. M. 1974, MNRAS, 167, 31P

Ferrarese, L., & Merritt, D. 2000, ApJ, 539, L9

Filippenko, A. V., Ho, L. C., & Sargent, W. L. W. 1993, ApJ, 410, L75

Filippenko, A. V., & Sargent, W. L. W. 1989, ApJ, 342, L11

Fritz, J., Franceschini, A., & Hatziminaoglou, E. 2006, MNRAS, 366, 767

Galliano, E., Alloin, D., Granato, G. L., & Villar-Martín, M. 2003, A&A, 412, 615

Gandhi, P. 2005, Asian Journal of Physics, 13, 90

Gardner, J. P., et al. 2006, Space Sci. Rev., 123, 485

BIBLIOGRAPHY

Gebhardt, K., et al. 2000, ApJ, 539, L13

Goncalves, A. C., Veron, P., & Veron-Cetty, M.-P. 1998, A&A, 333, 877

Goodrich, R. W., Veilleux, S., & Hill, G. J. 1994, ApJ, 422, 521

Granato, G. L., & Danese, L. 1994, MNRAS, 268, 235

Greenhill, L. J., et al. 2003, ApJ, 590, 162

Groves, B., Dopita, M., & Sutherland, R. 2006a, A&A, 458, 405

Groves, B. A., Heckman, T. M., & Kauffmann, G. 2006b, MNRAS, 371, 1559

Guyon, O., Sanders, D. B., & Stockton, A. 2006, ApJS, 166, 89

Haardt, F., & Maraschi, L. 1991, ApJ, 380, L51

Hao, L., et al. 2005, AJ, 129, 1783

Hartwick, F. D. A., & Schade, D. 1990, ARA&A, 28, 437

Hasinger, G., Miyaji, T., & Schmidt, M. 2005, A&A, 441, 417

Herrnstein, J. R., an, J. M., Greenhill, L. J., & Trotter, A. S. 2005, ApJ, 629, 719

Ho, L. C., Li, Z.-Y., Barth, A. J., Seigar, M. S., & Peng, C. Y. 2011, ApJS, 197, 21

Houck, J. R., et al. 2004, ApJS, 154, 18

Hubeny, I., Agol, E., Blaes, O., & Krolik, J. H. 2000, ApJ, 533, 710

BIBLIOGRAPHY

Ivezic, Z., & Elitzur, M. 1997, MNRAS, 287, 799

Jaffe, W., et al. 2004, Nature, 429, 47

Johansson, L. 1988, A&A, 191, 29

Jones, D. H., et al. 2004, MNRAS, 355, 747

—. 2009, MNRAS, 399, 683

Kaiser, M. E., et al. 2000, ApJ, 528, 260

Kaspi, S., Maoz, D., Netzer, H., Peterson, B. M., Vestergaard, M., & Jannuzi, B. T. 2005, ApJ, 629, 61

Kaspi, S., Smith, P. S., Netzer, H., Maoz, D., Jannuzi, B. T., & Giveon, U. 2000, ApJ, 533, 631

Kauffmann, G., et al. 2003, MNRAS, 346, 1055

Kay, L. E., & Moran, E. C. 1998, PASP, 110, 1003

Kembhavi, A. K., & Narlikar, J. V. 1999, Quasars and active galactic nuclei : an introduction

Kemper, F., Vriend, W. J., & Tielens, A. G. G. M. 2004, ApJ, 609, 826

Kennicutt, Jr., R. C. 1998, ARA&A, 36, 189

Kewley, L. J., Groves, B., Kauffmann, G., & Heckman, T. 2006, MNRAS, 372, 961

BIBLIOGRAPHY

Kewley, L. J., Heisler, C. A., Dopita, M. A., & Lumsden, S. 2001, ApJS, 132, 37

Khachikian, E. Y., & Weedman, D. W. 1974, ApJ, 192, 581

Kraemer, S. B., Ho, L. C., Crenshaw, D. M., Shields, J. C., & Filippenko, A. V. 1999, ApJ, 520, 564

Kriss, G. A., et al. 1992, in Bulletin of the American Astronomical Society, Vol. 24, American Astronomical Society Meeting Abstracts #180, 751

Krolik, J. H. 1999, Active galactic nuclei : from the central black hole to the galactic environment

Krolik, J. H., & Begelman, M. C. 1988, ApJ, 329, 702

LaMassa, S. M., Heckman, T. M., Ptak, A., Martins, L., Wild, V., Sonnentrucker, P., & Hornschemeier, A. 2011, ApJ, 729, 52

Landt, H., Elvis, M., Ward, M. J., Bentz, M. C., Korista, K. T., & Karovska, M. 2011, MNRAS, 414, 218

Lewis, K. T., Eracleous, M., & Sambruna, R. M. 2003, ApJ, 593, 115

Li, A. 2007, in Astronomical Society of the Pacific Conference Series, Vol. 373, The Central Engine of Active Galactic Nuclei, ed. L. C. Ho & J.-W. Wang, 561

Lira, P., Lawrence, A., O'Brien, P., Johnson, R. A., Terlevich, R., & Bannister, N. 1999, MNRAS, 305, 109

BIBLIOGRAPHY

Maiolino, R., & Rieke, G. H. 1995, ApJ, 454, 95

Malkan, M. A. 1983, ApJ, 268, 582

Malkan, M. A., Gorjian, V., & Tam, R. 1998, ApJS, 117, 25

Manske, V., Henning, T., & Men'shchikov, A. B. 1998, A&A, 331, 52

Marco, O., & Alloin, D. 2000, A&A, 353, 465

Markarian, B. E., Lipovetsky, V. A., Stepanian, J. A., Erastova, L. K., & Shapovalova, A. I. 1989, Soobshcheniya Spetsial'noj Astrofizicheskoj Observatorii, 62, 5

Masetti, N., et al. 2006, A&A, 455, 11

Matt, G., Perola, G. C., & Piro, L. 1991, A&A, 247, 25

Matthews, L. D., et al. 1999, AJ, 118, 208

Meléndez, M., Kraemer, S. B., Weaver, K. A., & Mushotzky, R. F. 2011, ApJ, 738, 6

Meléndez, M., et al. 2008, ApJ, 682, 94

Minezaki, T., et al. 2006, ApJ, 643, L5

Miyoshi, M., Moran, J., Herrnstein, J., Greenhill, L., Nakai, N., Diamond, P., & Inoue, M. 1995, Nature, 373, 127

Mor, R., & Netzer, H. 2012, MNRAS, 420, 526

Mor, R., Netzer, H., & Elitzur, M. 2009, ApJ, 705, 298

BIBLIOGRAPHY

Moran, E. C., Eracleous, M., Leighly, K. M., Chartas, G., Filippenko, A. V., Ho, L. C., & Blanco, P. R. 2005, AJ, 129, 2108

Moran, E. C., Filippenko, A. V., Ho, L. C., Shields, J. C., Belloni, T., Comastri, A., Snowden, S. L., & Sramek, R. A. 1999, PASP, 111, 801

Moran, E. C., Halpern, J. P., & Helfand, D. J. 1996, ApJS, 106, 341

Mushotzky, R. F., Fabian, A. C., Iwasawa, K., Kunieda, H., Matsuoka, M., Nandra, K., & Tanaka, Y. 1995, MNRAS, 272, L9

Nagar, N. M., & Wilson, A. S. 1999, ApJ, 516, 97

Narayan, R., Yi, I., & Mahadevan, R. 1995, Nature, 374, 623

Nardini, E., & Risaliti, G. 2011, MNRAS, 1318

Nenkova, M., Ivezić, Ž., & Elitzur, M. 2002, ApJ, 570, L9

Nenkova, M., Sirocky, M. M., Ivezić, Ž., & Elitzur, M. 2008a, ApJ, 685, 147

Nenkova, M., Sirocky, M. M., Nikutta, R., Ivezić, Ž., & Elitzur, M. 2008b, ApJ, 685, 160

—. 2010, ApJ, 723, 1827

O'Neill, P. M., et al. 2006, ApJ, 645, 160

Osterbrock, D. E. 1977, ApJ, 215, 733

Osterbrock, D. E., & De Robertis, M. M. 1985, PASP, 97, 1129

Osterbrock, D. E., & Martel, A. 1993, ApJ, 414, 552

Padovani, P. 1998, in IAU Symposium, Vol. 179, New Horizons from Multi-Wavelength Sky Surveys, ed. B. J. McLean, D. A. Golombek, J. J. E. Hayes, & H. E. Payne, 257

Parisi, P., et al. 2009, A&A, 507, 1345

—. 2012, A&A, 545, A101

Pecontal, E., Adam, G., Bacon, R., Courtes, G., Georgelin, Y., & Monnet, G. 1990, A&A, 232, 331

Pelletier, G., & Pudritz, R. E. 1992, ApJ, 394, 117

Peterson, B. M., et al. 2005, ApJ, 632, 799

Pier, E. A., & Krolik, J. H. 1992, ApJ, 401, 99

—. 1993, ApJ, 418, 673

Porquet, D., Kaastra, J. S., Page, K. L., O'Brien, P. T., Ward, M. J., & Dubau, J. 2004, A&A, 413, 913

Rees, M. J. 1998, Proceedings of the National Academy of Science, 95, 47

Reunanen, J., Kotilainen, J. K., & Prieto, M. A. 2003, MNRAS, 343, 192

Richards, G. T., et al. 2002, AJ, 123, 2945

Rigby, J. R., Diamond-Stanic, A. M., & Aniano, G. 2009, ApJ, 700, 1878

Rigby, J. R., Rieke, G. H., Donley, J. L., Alonso-Herrero, A., & Pérez-González, P. G. 2006, ApJ, 645, 115

Rouan, D., Rigaut, F., Alloin, D., Doyon, R., Lai, O., Crampton, D., Gendron, E., & Arsenault, R. 1998, A&A, 339, 687

Rowan-Robinson, M. 1995, MNRAS, 272, 737

Sandage, A. R. 1971, in Study Week on Nuclei of Galaxies, ed. D. J. K. O'Connell, 271

Sani, E., Lutz, D., Risaliti, G., Netzer, H., Gallo, L. C., Trakhtenbrot, B., Sturm, E., & Boller, T. 2010, MNRAS, 403, 1246

Sargent, W. L. W. 1970, ApJ, 160, 405

Sazonov, S. Y., Ostriker, J. P., Ciotti, L., & Sunyaev, R. A. 2005, MNRAS, 358, 168

Sazonov, S. Y., Ostriker, J. P., & Sunyaev, R. A. 2004, MNRAS, 347, 144

Schmidt, M., & Green, R. F. 1983, ApJ, 269, 352

Schmitt, H. R., Donley, J. L., Antonucci, R. R. J., Hutchings, J. B., & Kinney, A. L. 2003, ApJS, 148, 327

Schmitt, H. R., Kinney, A. L., Storchi-Bergmann, T., & Antonucci, R. 1997, ApJ, 477, 623

Schneider, D. P., et al. 2010, AJ, 139, 2360

Schweitzer, M., et al. 2008, ApJ, 679, 101

Seyfert, C. K. 1943, ApJ, 97, 28

Shakura, N. I., & Sunyaev, R. A. 1973, A&A, 24, 337

Shields, G. A. 1978, Nature, 272, 706

Smith, J. D. T., et al. 2007, ApJ, 656, 770

Stern, D., et al. 2005, ApJ, 631, 163

Terlevich, R., Melnick, J., Masegosa, J., Moles, M., & Copetti, M. V. F. 1991, A&AS, 91, 285

Thim, F., Hoessel, J. G., Saha, A., Claver, J., Dolphin, A., & Tammann, G. A. 2004, AJ, 127, 2322

Tran, H. D. 2001, ApJ, 554, L19

Tristram, K. R. W., & Schartmann, M. 2011, A&A, 531, A99

Tristram, K. R. W., et al. 2007, A&A, 474, 837

Tueller, J., Mushotzky, R. F., Barthelmy, S., Cannizzo, J. K., Gehrels, N., Markwardt, C. B., Skinner, G. K., & Winter, L. M. 2008, ApJ, 681, 113

Tueller, J., et al. 2010, ApJS, 186, 378

Turner, T. J., George, I. M., Nandra, K., & Mushotzky, R. F. 1997, ApJS, 113, 23

Turner, T. J., Netzer, H., & George, I. M. 1996, ApJ, 463, 134

Ulrich, M.-H., Maraschi, L., & Urry, C. M. 1997, ARA&A, 35, 445

van Bemmel, I. M., & Dullemond, C. P. 2003, A&A, 404, 1

Vasudevan, R. V., Fabian, A. C., Gandhi, P., Winter, L. M., & Mushotzky, R. F. 2010, MNRAS, 402, 1081

Vaughan, S., Iwasawa, K., Fabian, A. C., & Hayashida, K. 2005, MNRAS, 356, 524

Véron-Cetty, M.-P., & Véron, P. 2006, A&A, 455, 773

Veron-Cetty, M. P., & Veron, P. 2010, VizieR Online Data Catalog, 7258, 0

Ward, M., Elvis, M., Fabbiano, G., Carleton, N. P., Willner, S. P., & Lawrence, A. 1987, ApJ, 315, 74

Weaver, K. A., Nousek, J., Yaqoob, T., Mushotzky, R. F., Makino, F., & Otani, C. 1996, ApJ, 458, 160

Weaver, K. A., et al. 2010, ApJ, 716, 1151

BIBLIOGRAPHY

Weedman, D. W., et al. 2005, ApJ, 633, 706

Weingartner, J. C., & Draine, B. T. 2001, ApJ, 548, 296

White, R. L., et al. 2000, ApJS, 126, 133

Winkler, H. 1992, MNRAS, 257, 677

Winter, L. M., Lewis, K. T., Koss, M., Veilleux, S., Keeney, B., & Mushotzky, R. F. 2010, ApJ, 710, 503

Winter, L. M., Mushotzky, R. F., Reynolds, C. S., & Tueller, J. 2009, ApJ, 690, 1322

Winter, L. M., Mushotzky, R. F., Tueller, J., & Markwardt, C. 2008, ApJ, 674, 686

Wrobel, J. M., & Ho, L. C. 2006, ApJ, 646, L95

Vita

Seamus Riley received a B. A. degree in Physics with a minor in Astrophysics from Tufts University in 2006. He enrolled in the Physics and Astronomy Ph. D. program at Johns Hopkins University the following fall. While a first year teaching assistant, he was awarded the Roland Prize for Innovation and Excellence in Teaching. He began his research identifying dwarf galaxies in nearby galaxy clusters using Bayesian redshift identifications and Hubble ACS data with Professor Holland Ford. For his presentation of this work at the American Astronomical Society 2007 summer meeting he was awarded the Chambliss Astronomy Student Achievement Student Award. Following this, he became interested in Active Galactic Nuclei and started his dissertation work with Kim Weaver. This research focuses on the infrared spectra of accreting supermassive black hole systems in an effort to disambiguate the equatorial obscuration region.

Starting in September of 2013, Seamus will leave academics and transition to an internal consulting position with Ab Initio, a software company in Lexington, MA.

VITA